Cleaning Effect of Microbubbles and Development of Microbubble Generator

李, 月桂

(Degree)
博士（工学）

(Date of Degree)
2024-03-25

(Date of Publication)
2025-03-01

(Resource Type)
doctoral thesis

(Report Number)
甲第8935号

(URL)
https://hdl.handle.net/20.500.14094/0100490160

Doctoral Dissertation

Cleaning Effect of Microbubbles and Development of Microbubble Generator

（マイクロバブルによる汚れの除去および気泡生成法に関する研究）

January 2024

Department of Mechanical Engineering,
Graduate School of Engineering,
Kobe University

LI YUEGUI

李 月桂

Table of Contents

Table of Contents ····· i
List of Figures ····· v
List of Tables ····· ix
Nomenclature ····· x

1. Introduction 1
1.1 Background ····· 1
1.2 Characteristics of microbubbles ····· 3
1.2.1 Rise velocity ····· 3
1.2.2 Shape regimes ····· 4
1.2.3 Internal pressure ····· 5
1.2.4 Mass transfer ····· 6
1.3 Applications of microbubbles ····· 7
1.4 Removal effects of microbubble ····· 10
1.5 Microbubble generation methods ····· 10
1.6 Objectives ····· 13
1.7 Structure of dissertation ····· 14
References for Chapter 1 ····· 16

2. Effects of microbubbles on removal of viscous oil from duct wall 21
2.1 Introduction ····· 21
2.2 Experimental apparatus and methods ····· 23
2.2.1 Experimental setup and experimental conditions ····· 23

2.2.2 Observation system and image analyses for oil thickness measurement ····· 26
2.2.3 Evaluation methods of bubble diameter and number density ····· 31
2.2.3.1 Image processing ····· 31
2.2.3.2 Evaluation of average bubble diameter and number density ····· 32
2.3 Results and discussion ····· 35
2.3.1 Influence of water flow on oil removal ····· 35
2.3.2 Influence of microbubbles on oil removal ····· 37
2.3.3 Adhesion of microbubbles on oil interface under turbulent flow condition ·· 41
2.4 Conclusions ····· 49
References for Chapter 2 ····· 50

3. Numerical prediction of microbubbles in water with mass transfer 53
3.1 Introduction ····· 53
3.2 Numerical method ····· 55
3.2.1 Single bubbles ····· 55
3.2.2 Bubble groups in liquid flows ····· 57
3.2.3 Influence of each numerical parameter on prediction of d_B ····· 59
3.3 Results of single bubble simulations ····· 64
3.3.1 Validation for growing bubble ····· 64
3.3.2 Validation for shrinking bubble ····· 66
3.3.3 Effects of dissolved oxygen concentration on d_{Beq} ····· 67
3.4 Results of Validation for microbubble flows ····· 70
3.4.1 Experimental ····· 70
3.4.1.1 Experimental apparatus and methods ····· 70
3.4.1.2 Results of microbubble flow ····· 73
3.4.2 Comparison between numerical predictions and measured data ····· 76
3.5 Conclusions ····· 81
References for Chapter 3 ····· 82

4. Generation of microbubbles by subcooled boiling 84
4.1 Introduction ····· 84

4.2 Experimental apparatus and methods ····· 86
4.2.1 Experimental setup and experimental conditions ····· 86
4.2.1.1 Experimental setup and measurement area ····· 86
4.2.1.2 Experimental conditions ····· 89
4.2.2 Measurement methods ····· 91
4.2.2.1 Evaluation method by image analyses ····· 91
4.2.2.2 Measurement time ····· 91
4.2.2.3 Evaluation method of heat transfer from wire surface ····· 93
4.3 Results and discussion ····· 96
4.3.1 Influence of *DO* and microbubble generation mechanism ····· 96
4.3.1.1 Influence of dissolved oxygen concentration ····· 96
4.3.1.2 Microbubble generation mechanism ····· 100
4.3.2 Influence of heat flux with DC and AC ····· 101
4.3.2.1 Boiling curve of DC and AC ····· 101
4.3.2.2 Effects of DC and AC on microbubble generation ····· 103
4.3.3 Influence of AC frequency ····· 108
4.3.4 Microbubble generation using a nichrome wire ····· 109
4.4 Application of bubble generation method based on subcooled boiling to oil removal effects ····· 111
4.5 Conclusions ····· 114
References for Chapter 4 ····· 115

5. Conclusions **117**

Appendix A. Evaluation of the amount of bubble generation **121**
A.1 Experimental setup and evaluation method ····· 121
A.1.1 Experimental setup ····· 121
A.1.2 Evaluation method ····· 123
A.2 Bubble characteristics and heat transfer surface temperature ····· 127
A.3 Evaluation of bubble generation ····· 128

A.3.1 Flow state ····· 128
A.3.2 n_B ····· 130
A.3.3 Rise velocity ····· 131
A.3.4 Amount of generated bubbles ····· 132
References for Appendix A ····· 133

Appendix B. Attachment state of microbubbles to dirt surface in laminar flow 134

List of Figures

Fig. 1.1 Microbubble ····· 2
Fig. 1.2 Difference in behavior between microbubble and non-fine bubbles ····· 2
Fig. 1.3 Relation between V_T and d_B by Stokes law ····· 4
Fig. 1.4 Applications of microbubbles in various fields ····· 7
Fig. 1.5 Diameter and number density of bubbles generated by various methods ····· 11
Fig. 1.6 Pressurized dissolution method ····· 11
Fig. 1.7 Microbubble generator using a Venturi tube ····· 12
Fig. 1.8 Microbubble generator using a swirling flow ····· 12
Fig. 1.9 Microbubble generator using microporous ····· 13

Fig. 2.1 Factors of microbubbles effective for cleaning ····· 22
Fig. 2.2 Experimental apparatus. (a) Schematic of experimental setup. (b) Channel cross-section of test section. (c) Side view of test section ····· 25
Fig. 2.3 Optical setup for micrography ····· 27
Fig. 2.4 An example of fluorescence image ····· 27
Fig. 2.5 Test cell and measurement points ····· 28
Fig. 2.6 Relation between oil thickness δ and fluorescence intensity $\bar{I}$ ····· 29
Fig. 2.7 Relationship between removal effect and photobleaching ····· 30
Fig. 2.8 Image processing with average image ····· 31
Fig. 2.9 Image processing with contour and center detection ····· 32
Fig. 2.10 Measurement of DOF ····· 33
Fig. 2.11 Images of bubble detection ····· 34
Fig. 2.12 Changes in oil thickness δ by water flow ····· 35

Fig. 2.13 Relation between $-d\delta/dt$ and τ_w of water flow ····· 36
Fig. 2.14 Probability density function of bubble diameter ····· 38
Fig. 2.15 Relation between Re, $\overline{d}_B$ and $\overline{n}_B$ of microbubbles ····· 38
Fig. 2.16 Changes in oil thickness δ by water flow with microbubbles ····· 39
Fig. 2.17 Relation between $-d\delta/dt-c_s[\tau_W/\rho]^{1/2}$ and $\overline{n}_B$ of water flow ····· 40
Fig. 2.18 Processes of oil removal with bubble detachment (Re = 6750) ····· 42
Fig. 2.19 Microbubble attachment and bubble coalescence ····· 43
Fig. 2.20 Relation between d_B and t' in stagnant water and microbubbles flow ····· 44
Fig. 2.21 Microbubbles (MB) grow to a certain degree and coalesce with other bubbles 45
Fig. 2.22 Microbubble adhesion and peel-off ····· 46
Fig. 2.23 Relation between peel-off rate and t (Re = 6750) ····· 47
Fig. 2.24 Process of removing oil by water flow with microbubble (turbulent flow condition) ····· 48

Fig. 3.1 Schematic of simulated system ····· 58
Fig. 3.2 Effects of Δt on bubble diameter change ····· 60
Fig. 3.3 Effects of Δr on bubble diameter change ····· 61
Fig. 3.4 Relation between Δr and $\varepsilon_{\Delta r}$ ····· 61
Fig. 3.5 Effects of $\widetilde{A}$ on bubble diameter change ····· 63
Fig. 3.6 Relation between $\widetilde{A}$ and $\varepsilon_{\widetilde{A}}$ ····· 63
Fig. 3.7 Microbubble growth (single bubble) ····· 65
Fig. 3.8 Comparison between experiment data of a single shrinking bubble (Ward et al., 1982) and numerical prediction ····· 67
Fig. 3.9 Change in d_B at low DO (8.8×10^{-3} kg/m^3) ····· 68
Fig. 3.10 Change in d_B at high DO (1.47×10^{-2} kg/m^3) ····· 68
Fig. 3.11 Relation between d_{Beq} and DO ····· 69
Fig. 3.12 Apparatus for microbubble flow experiment ····· 71
Fig. 3.13 Test section (a), decompression nozzle (b) and flow pattern in the decompression nozzle (c) ····· 72
Fig. 3.14 Bubble size distribution ····· 74
Fig. 3.15 Gas volume fraction ····· 75

Fig. 3.16 Measured and predicted bubble size distribution of J_L = 9.0 m/s (NC)····· 76
Fig. 3.17 Measured and predicted bubble size distribution of J_L = 10.5 m/s (BC) ····· 76
Fig. 3.18 Measured and predicted bubble size distribution of J_L = 12.5 m/s (SC)····· 77
Fig. 3.19 Measured and predicted volume fractions of J_L = 9.0 m/s (NC)····· 77
Fig. 3.20 Measured and predicted volume fractions of J_L = 10.5 m/s (BC) ····· 77
Fig. 3.21 Measured and predicted volume fractions of J_L = 12.5 m/s (SC)····· 78
Fig. 3.22 Time evolution of volume fraction of bubbles ····· 79
Fig. 3.23 Time evolution of ΔDO ····· 80

Fig. 4.1 Experimental apparatus ····· 87
Fig. 4.2 Imaging area and measurement area ····· 88
Fig. 4.3 Bubble Observation System ····· 89
Fig. 4.4 Imaging area ····· 89
Fig. 4.5 Relation between $\overline{d}_B$, $\overline{n}_B$ and t ····· 92
Fig. 4.6 Changes in T and DO ····· 93
Fig. 4.7 Circuit diagram ····· 93
Fig. 4.8 Relation between T_W and R_p ····· 95
Fig. 4.9 Images of generated microbubbles (t = 5.0 s)····· 97
Fig. 4.10 Process of microbubble generation ····· 98
Fig. 4.11 Bubble size distribution ($\overline{q}$ = 4.5 MW/m^2, f = 60 Hz) ····· 99
Fig. 4.12 Effect of DO on $\overline{d}_B$ and $\overline{n}_B$ ($\overline{q}$ = 4.5 MW/m^2, f = 60 Hz) ····· 100
Fig. 4.13 Microbubble generation process····· 101
Fig. 4.14 Boiling curve for DC [16] ····· 102
Fig. 4.15 Boiling curve for AC ····· 103
Fig. 4.16 Images of generated microbubbles (Top: DC, Bottom: AC) ····· 104
Fig. 4.17 Heat transfer surface temperature during one cycle ($\overline{q}$ = 4.5 MW/m^2) ····· 105
Fig. 4.18 Generation state with different heat transfer surface temperature ····· 105
Fig. 4.19 Effects of $\overline{q}$ on $\overline{n}_B$ ····· 106
Fig. 4.20 Bubble size distribution····· 106
Fig. 4.21 Effects of $\overline{q}$ on $\overline{d}_B$ ····· 107
Fig. 4.22 Effects of $\overline{q}$ on $\overline{\alpha}$ ····· 107

Fig. 4.23 Microbubbles generated with different AC frequencies (AC, $\bar{q}$ = 4.5 MW/m^2)108
Fig. 4.24 Relations between f, $\bar{d}_B$ and $\bar{n}_B$ ····· 109
Fig. 4.25 Comparison in bubble generation state between nichrome and platinum wires 110
Fig. 4.26 Experimental setup for cleaning ····· 112
Fig. 4.27 Effects of L and $\bar{q}$ on oil removal. (t = 10 min in cases (b), (c) and (d)) ····· 113

Fig. A.1 Experimental apparatus ····· 123
Fig. A.2 Test section of calculation ····· 124
Fig. A.3 Measurement area ····· 126
Fig. A.4 Relation between t and T_W ····· 128
Fig. A.5 Schematic diagram of the measurement area ····· 129
Fig. A.6 Images of generated microbubbles (DC, $\bar{q}$ = 4.5 MW/m^2) ····· 129
Fig. A.7 Images of generated microbubbles (AC (f = 60 Hz), $\bar{q}$ = 4.5 MW/m^2) ····· 130
Fig. A.8 Distribution of $\bar{n}_B$ ····· 131
Fig. A.9 $\bar{u}_{Bz}$ distribution ····· 132

Fig. B.1 Experimental apparatus ····· 135
Fig. B.2 State of microbubbles attached on oil ····· 136

List of Tables

Table 1.1 Relation between d_B and Eo at $M = 3.1 \times 10^{-11}$ (air-water system) ····· 5
Table 1.2 Relation between d_B and p_B ····· 5

Table 2.1 Entrance length L_e ····· 24
Table 2.2 Oil thickness at 120 s. The unit is [μm] ····· 39

Table 3.1 Numerical conditions ····· 59
Table 3.2 Effects of Δr and $\varepsilon_{\Delta r}$ ····· 62
Table 3.3 Numerical conditions for single bubble simulation ····· 65

Table 4.1 Platinum property [12] ····· 87
Table 4.2 Experimental conditions ····· 90
Table 4.3 Experimental condition for measurement time evaluation ····· 91
Table 4.4 $\overline{d}_B$ and $\overline{n}_B$ at each $\overline{q}$ ····· 110
Table 4.5 Relation of $\overline{q}$, L and V_{res} ····· 112

Table A.1 Relation between $\overline{u}$, d_B and n_B ····· 127
Table A.2 Relation between $\overline{u}$ and T_{Wave} ····· 128

Nomenclature

A	computational domain size [m]
Bi	Biot number [–]
c_s	dimensionless constant for shear-induced oil removal [–]
c_B	constant for oil removal by microbubble [m^3/s]
C	concentration of fluorescent dye [mol/m^3]
C_S	interfacial concentration of gaseous species [mol/m^3]
C_L	concentration of liquid [mol/m^3]
C_{H2O}	concentration of water [mol/m^3]
d_B	sphere-volume-equivalent bubble diameter [μm]
d_H	hydraulic equivalent diameter [m]
d_{Beq}	equilibrium diameter [m]
D	diffusion coefficient [–]
DO	dissolved oxygen concentration [kg/m^3]
E_o	Eötvös number [–]
F_b	buoyant force [N]
F_σ	surface tension force [N]
f	AC frequency [Hz]
h	phase change heat transfer [$W/m^2 \cdot K$]
H	Henry's constant [–]
H_{DOF}	depth of field [m]
I	fluorescence intensity [–]
I_{LL}	intensity of laser light [–]
I_P	intensity for photobleaching without flow [–]
I_C	intensity under cleaning [–]
I_E	electric current [A]
J_L	liquid volumetric flux [m/s]
k_p	Heat conductivity of platinum wire [W/m·K]

K	number of sample image [–]
l_H	hydraulic equivalent length
L	distance [m]
L_e	entrance length [m]
m	molar mass [kg/mol]
$\dot{m}$	mass transfer rate [–]
M	Morton number [–]
n_B	number density [m^{-3}]
N	number of moles [–]
N_B	number of bubble [m^{-3}]
p	pressure [Pa]
p_{vaper}	saturation water vapor pressure [Pa]
P	probability density function [–]
P_e	perimeter of the channel [m]
q	heat flux [MW/m^2]
Q	liquid volume flow rate [m^3/s]
R	bubble radius [m]
R_R	electrical resistance of fixed resistor [Ω]
R_G	gas constant [J/mol·K]
R_p	electrical resistance of platinum wire [Ω]
Re	Reynolds number [–]
S	measurement area [m^2]
S_p	surface area [m^2]
S_c	channel cross-sectional area [m^2]
t	time [s]
t'	time for bubble growth [s]
T	temperature [K]
T_m	Melting point [K]
T_W	heat transfer surface temperature [K]
T_E	Elapsed time after passing through decompression nozzle [s]
ΔT_{sat}	saturation temperature [K]
u	velocity of liquid [m/s]
u^*	frictional velocity [m/s]
u_r	velocity normal to the interface [m/s]
V_{res}	residual volume [m^3]

V voltage [V]
V_T rise velocity of bubble [m/s]
y mole fraction [–]
Δt time increments [s]
Δr grid spacing [m]

Greek letters

α gas volume fraction [–]
σ surface tension
δ oil thickness [μm]
ρ density [kg/m^3]
ρ_E Electrical resistivity [Ω·m]
μ viscosity [Pa·s]
μ_L viscosity of liquid [Pa·s]
τ_w shear stress [Pa]
ε errors [–]

Subscripts

0 initial condition
B bubble
c channel
C cleaning
G gas
L liquid
LL laser light
p platinum wire
P photobleaching
w water
W wall

Chapter 1

Introduction

1.1 Background

Around the end of the 1990s, several major media outlets covered the rapid growth of young oysters in Hiroshima due to the effects of microbubbles (Fig. 1.1), and the existence and success of microbubbles spread throughout Japan [1]. It was Professor Hirofumi Ohnari who provided microbubble technology for oyster farming in Hiroshima. Microbubbles of 1–100 μm in diameter [2] and nano-sized bubbles (ultrafine bubble) have been named fine bubbles by ISO20480-1 in recent years. Microbubbles are characterized by high internal pressure; the gas pressure inside a bubble is higher than the liquid pressure due to the action of surface tension, and long residence time [3] as shown in Fig. 1.2. The most common air-embedded non-fine bubbles cannot maintain a spherical shape in water, but instead deform into an elliptical shape and rise with a zigzaging or spiral motion [4]. Microbubbles, on the other hand, do not deform and rise slowly enough [5]. Therefore, in clean water where the concentration of dissolved gases is not high, microbubbles are in contact with water for a long time, and the dissolution of the air in water progresses. However, the situation is different under conditions of supersaturation at shallow water depths as will be described in the following sections.

Microbubbles have been reported to have cleaning effects [6] and to reduce frictional resistance [7]. Compared to millimeter bubbles, microbubbles have a large interfacial area

concentration and a high mass transfer rate due to the large internal pressure, as well as having high penetration ability into narrow areas [8]. In addition to these characteristics, microbubble flows can be composed of only gases and water, making them economical and low environmental impact, and have been utilized in a wide range of fields as will be described in Section 1.3.

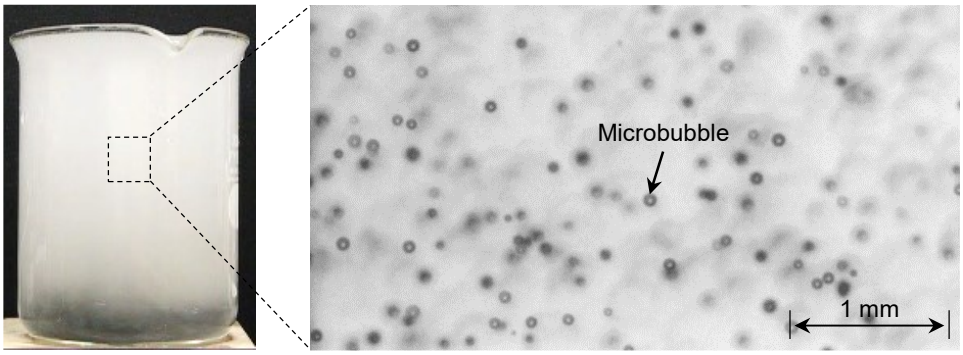

Fig. 1.1 Microbubble.

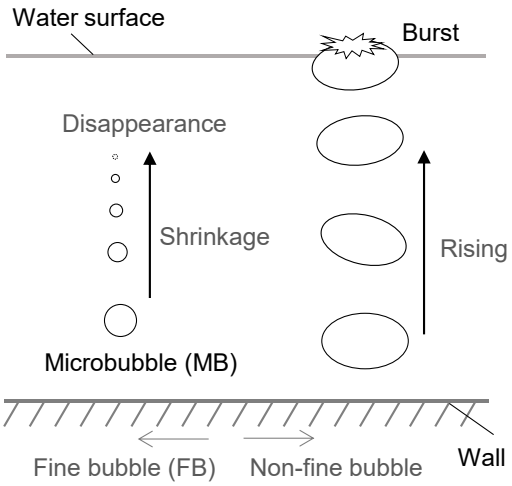

Fig. 1.2 Difference in behavior between microbubble and non-fine bubbles.

1.2 Characteristics of microbubbles

1.2.1 Rise velocity

Although the rise velocity, V_T, of microbubbles depends on the liquid properties, microbubbles become small spherical shapes in water, and the behavior of microbubbles is similar to the settling motion of solid spheres in water with surface-active agents. Therefore, the rise velocity [9] of microbubbles in water as the no-slip condition can be explained by the following Stokes equation:

$$V_T = \frac{(\rho_L - \rho_G) g d_B^2}{18 \mu_L} \tag{1.1}$$

$$Re = \frac{\rho_L V_T d_B}{\mu_L} \tag{1.2}$$

where d_B is the bubble diameter, ρ_L the density of liquid, ρ_G the density of gas, and μ_L the viscosity of liquid. The bubble Reynolds number, Re, of microbubbles in water is less than 1 at $d_B = 100$ μm in water as calculated by Eq. (1.1) and Eq. (1.2). Since $Re < 1$, the rise velocity of microbubbles can be expressed by Eq. (1.1) [10, 11]. The relationship between V_T and d_B of microbubbles at the temperature $T = 293$ K in water is shown in Fig. 1.3. Microbubbles of 10 μm rise only about 19.5 cm per hour.

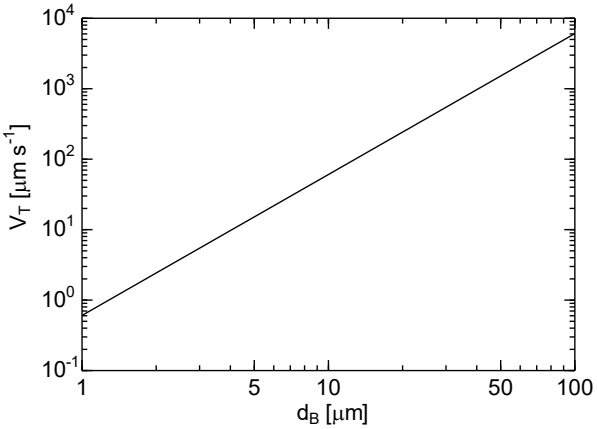

Fig. 1.3 Relation between V_T and d_B by Stokes law.

1.2.2 Shape regimes

Grace et al. [12] pointed out that Eötvös, Morton and Reynolds numbers, *Eo*, *M* and *Re*, are dominant factors governing the shape of fluid particles rising or falling freely through stagnant liquids. They showed that deformation of fluid particles depends on *Eo* and *M*, and fluid particles of small *Eo* less deform than those of high *Eo* even at the same *M*.
Here, *Eo* and *M* are defined by

$$Eo = \frac{F_b}{F_\sigma} = \frac{(\rho_L - \rho_G) g d_B^2}{\sigma} \tag{1.3}$$

$$M = \frac{\mu_L^4 (\rho_L - \rho_G) g}{\rho_L^2 \sigma^3} \tag{1.4}$$

where F_b is the buoyant force, F_σ the surface tension force, and σ the surface tension (σ = 72.8 mN/m at T = 293 K). Table 1.1 shows the relation of d_B and *Eo* at the same *M* for microbubbles and millimeter bubbles in air-water system. See Clift et al. [13] for more details of *Eo* and *M* of bubbles and drops. The *Eo* of d_B =100 μm was sufficiently small to indicate that the surface tension is mostly responsible for the shape of the bubble. This is understood why non-fine bubbles cannot maintain a spherical shape in water and deform into an elliptical

shape, etc. In contrast, microbubbles can maintain a spherical shape as shown in Fig. 1.2.

1.2.3 Internal pressure

Microbubbles have a spherical interface and are surrounded by water and liquid molecules with large intermolecular forces on the outside, and gas molecules exist only at a sparse density compared to the inside of the bubble. The pressure inside the bubble is therefore higher than the pressure around the bubble by Δp according to the following Young–Laplace equation due to the effect of surface tension.

$$\Delta p = \frac{4\sigma}{d_B} \tag{1.5}$$

The relationship between d_B of an air bubble in water and the internal pressure, p_B, of bubble is shown in Table 1.2 (assuming the surface tension of water σ is 72.8 mN/m at T = 293 K and the surrounding pressure is 1 atm).

Table 1.1 Relation between d_B and Eo at $M = 3.1 \times 10^{-11}$ (air-water system).

d_B	Eo
6 mm [13]	5
1 mm	0.14
100 μm	1.35×10^{-3}
10 μm	1.35×10^{-5}
1 μm	1.35×10^{-7}

Table 1.2 Relation between d_B and p_B.

d_B	p_B [atm]
1 mm	1.003
100 μm	1.03
10 μm	1.29
1 μm	3.87

It can be seen that when bubbles are reduced to microbubbles, the internal pressure of the bubbles becomes non-negligible compared to atmospheric pressure (= 1 atm). On the liquid phase side, the pressure is about the same as the system pressure (atmospheric pressure) added to the liquid head (water pressure), but the internal pressure of the bubble is high, and the gas component dissolves at a high mass transfer rate into the liquid phase in contact with the bubble surface.

1.2.4 Mass transfer

Some studies have been reported that a microbubble can grow in the liquid [14, 15]. The bubble diameter, d_B, and the number density, n_B, of microbubbles are, therefore, important factors in the development and improvement of the applications, and the control of these factors is required for microbubble generators and applications [16]. However, both d_B and n_B would change in time after generation due to the mass transfer between the bubbles and the surrounding liquid.

The cause of the trends in microbubbles diameter can be understood as follows. The interfacial concentration, C_S, of the gaseous species forming a bubble is given by

$$C_S = C_L \frac{p_B}{H} \tag{1.6}$$

where H is Henry's constant, C_L the concentration of liquid, and p_B the gas pressure. Assuming that the bubble shape is spherical yields

$$C_S = \frac{C_L}{H}\left[p_L + \frac{4\sigma}{d_B} \right] \tag{1.7}$$

where σ is the surface tension, and p_L the liquid pressure. A difference between C_S and the concentration, C_0, of the dissolved gas in the liquid phase drives the interfacial mass transfer. Therefore, the equilibrium diameter, d_{Beq}, for C_0 is given by

$$d_{Beq} = \frac{4\sigma}{C_0 H / C_L - p_L} \tag{1.8}$$

A bubble of d_B smaller (larger) than d_{Beq} will shrink (grow). Microbubbles in liquid flows are usually poly-dispersed and may grow or shrink depending on their size and d_{Beq}, resulting in a change in the bubble size distribution.

1.3 Applications of microbubbles

Microbubbles have been utilized in a variety of fields such as agriculture [17], environmental [18], washing process [19], medicine [20, 21], water treatment [22–24] and so on because of their characteristics suitable for applications in those fields, e.g. small size, high internal pressure, long residence time [3] and large interfacial area concentration [8]. A brief summary of research in each field is given below. Fig. 1.4 (a)–(e) shows the applications of microbubbles in various fields as will be described in the following.

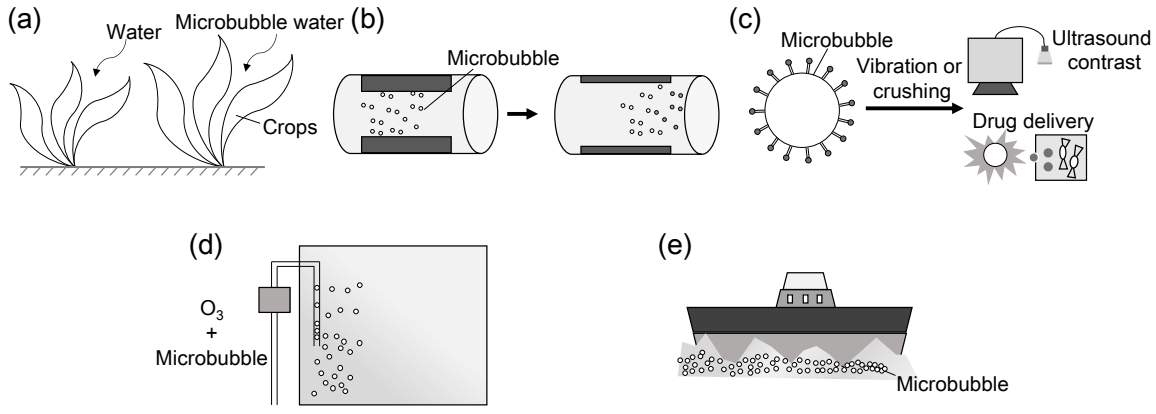

Fig. 1.4 Applications of microbubbles in various fields.

(a) Agriculture and fisheries fields

Microbubbles are used to improve crop yields and quality. Some agricultural water is unsuitable for agriculture, such as water with low dissolved oxygen or residual chlorine. Problems with agricultural water can lead to crop growth problems and soil contamination. Therefore, by adding microbubbles to agricultural water, the amount of dissolved oxygen can be increased by the long residence time and large interfacial area concentration, and the water quality can be improved by the contaminant removal effect, thereby increasing the activity of agricultural crops [25–28].

In aquaculture, microbubbles are being used in the cultivation of fish and shellfish. In oyster farming [1], it has been reported that injecting microbubbles into the oyster farm increases blood flow to the oysters and promotes their growth. In addition, when farmed fish are present in high-density tanks, they may die due to anoxic conditions. Microbubbles injected into the tank can improve the anoxic condition by dissolving oxygen from microbubbles into seawater [29, 30].

(b) Environmental fields

Cleaning processes are important in the manufacturing and production processes of industrial products, and in the food industry, including beverage products, the removal of oil and grease adhering to pipe walls is also necessary [31]. However, conventional industrial cleaning processes use chlorofluorocarbon gas, volatile organic compounds, acid-alkali cleaning agents, etc., and the environmental burden caused by these chemicals and the cost of waste liquid treatment have become issues. In response, there is a need to develop a cleaning technology with less environmental impact [32]. Therefore, development of a cleaning technology that can remove or reduce these chemical substances using microbubbles is underway.

(c) Medicine fields

Microbubbles of 10 μm in size are used as contrast agents in ultrasound diagnosis [33, 34] and have a shell structure in which the surface is covered with a thin shell of surfactant, lipid, or protein. The natural frequency of microbubbles has a large acoustic impedance difference from that of body tissues, resulting in a strong ultrasonic echo signal [20]. Researches have

also been underway to utilize microbubbles for cancer and stone treatment. Recently, a technique for removing dental plaque using microbubbles has also been reported to reduce periodontal disease [35].

(d) Water treatment fields

Microbubble technologies are being used in water treatment. Ozone is often used as an oxidant in drinking water disinfection and wastewater treatment [36, 37]. Ozone treatment is reported to be very effective in reducing color in dye wastewater because it attacks conjugated double bonds, which are often associated with color [21]. However, the low solubility of ozone has been attributed to its low mass transfer rate between gas and liquid. The effectiveness of ozone treatment can be enhanced by increasing the surface area of ozone through the formation of smaller bubbles.

(e) Drag reduction

In recent years, microbubbles have been applied to drag reduction in ship engineering, and this method has been effective in reducing drag over a wide range of speeds. It has been reported that microbubbles have a very large effect of reducing drag [38, 39]. There is no established theory on the mechanism of frictional drag reduction by microbubbles, but one of the possible mechanisms is the density effect. The size of bubbles is one of the important influencing factors and is mainly related to the flow characteristics. Smaller bubbles are more beneficial for drag reduction [40].

1.4 Removal effects of microbubble

Up to the present, many studies have been conducted on cleaning using microbubbles. For instance, Tamura et al. [41] reported the effects of microbubbles using a Venturi tube to promote the removal of chemical solvent. Fujimoto et al. [12] reported the detergency effects of adding surfactants to microbubbles generated by a Venturi-tube-type microbubble generation method, and the effects of removing surfactants adsorbed on skin surface by microbubbles [43]. Takahashi et al. [44] used ozone microbubbles generated by a pressurized dissolution method in photoresist removal. The existence of microbubbles in ozonized water increased dissolved ozone concentration and improved the photoresist removal rate. Their cleaning efficiency was however inferior to that of hot concentrated sulfuric acid, and it has not yet been widely used in practical applications. Furthermore, Minagawa et al. [45] reported that in immersion cleaning of lubricant oil in water containing microbubbles, numerous bubbles are generated within the oil, which coalesce and grow, adsorb the oil, and then float to the surface, thereby removing the oil. However, the mechanism by which microbubbles are generated in oil has not been fully elucidated.

As described above, studies on cleaning with microbubbles have been reported, and the factors that make water containing microbubbles effective for cleaning, e.g., the adsorption of dirt at the gas-liquid interface, the effects of surface charge, the possibility that bubbles act as an abrasive, the lifting effect of bubbles on dirt, and the soaking of dirt into the microstructure by lowering surface tension. However, none of these factors has been clearly demonstrated, and the detailed mechanism regarding the removal effect has not been fully elucidated.

1.5 Microbubble generation methods

Several methods for generating microbubbles have been proposed. The d_B and n_B of the generated bubbles are different for each method as shown in Fig. 1.5. The main methods are described below.

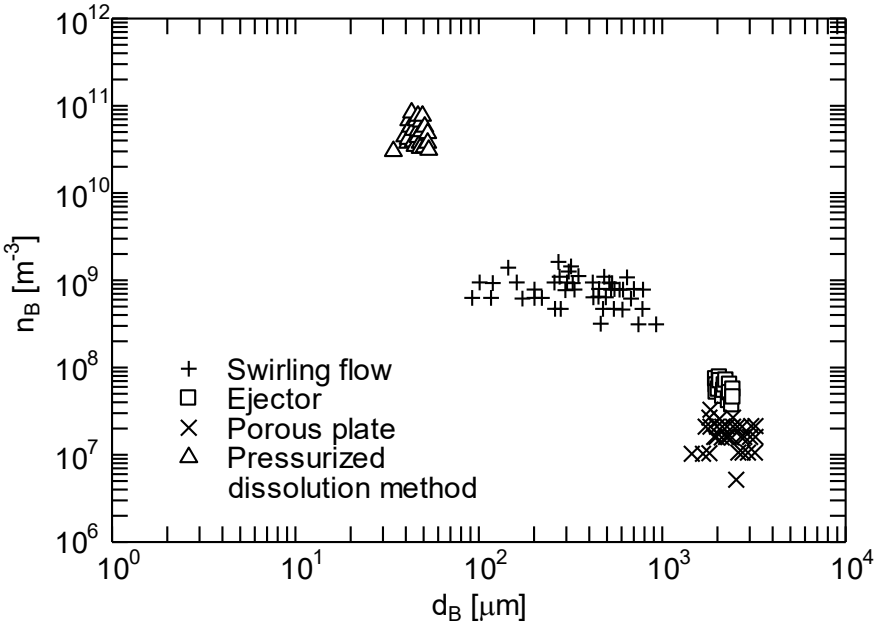

Fig. 1.5 Diameter and number density of bubbles generated by various methods [46–49].

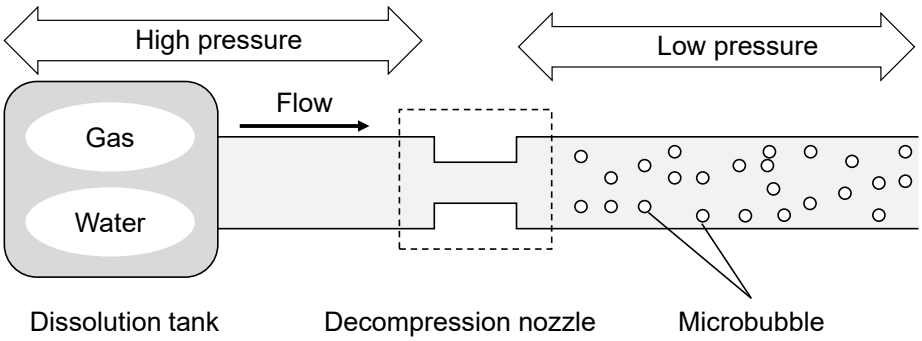

Fig. 1.6 Pressurized dissolution method.

(a) Pressurized dissolution method

In the pressurized dissolution method [49], the liquid and gas phases are mixed under high pressure to dissolve the gas phase in the liquid phase, and then the pressure is rapidly reduced at the nozzle to form microbubbles from the dissolved gas phase as shown in Fig. 1.6. Although this method requires a container for dissolving the gas phase under high pressure, it can generate microbubbles with diameters of several tens of micrometers or less at high number density.

(b) Gas-liquid shear method

This method makes use of breakup of gas-phase clumps by shearing the flow to generate microbubbles. A Venturi tube [50] has a condensed flow section as shown in Fig. 1.7. After the mixture of the gas and liquid phases reaches the speed of sound in the converged flow section, a sudden increase in pressure generated under the condensed flow section causes bubbles to expand rapidly and collapse to form microbubbles. Although it is difficult to generate microbubbles of several tens of micrometers or less at high density with this method, the simple structure makes it easy to downsize the equipment.

A microbubble generation method by swirling flow [51] is shown in Fig. 1.8. In a swirling flow, a gas-liquid two-phase flow is formed by mixing the gas phase with the liquid phase that is swirling at high speed in the circumferential direction in the flow path, and the gas phase is broken up by shearing and crushing due to the difference in swirling speed to generate microbubbles. This method is characterized by the ability to control bubble refinement by the swirling velocity.

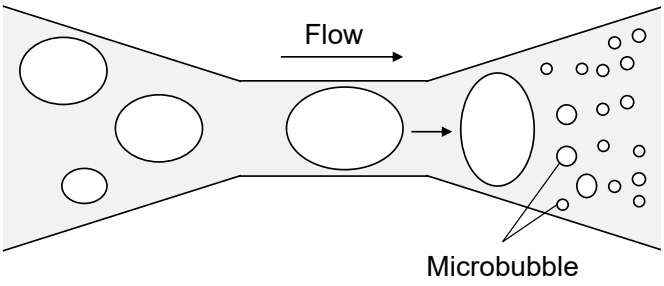

Fig. 1.7 Microbubble generator using a Venturi tube.

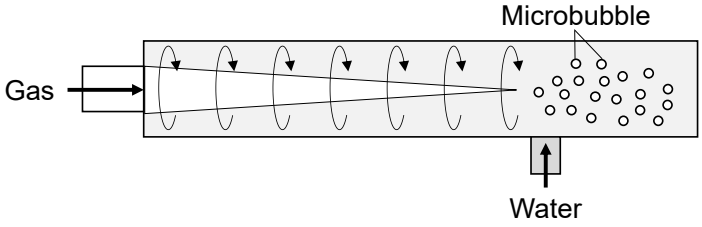

Fig. 1.8 Microbubble generator using a swirling flow.

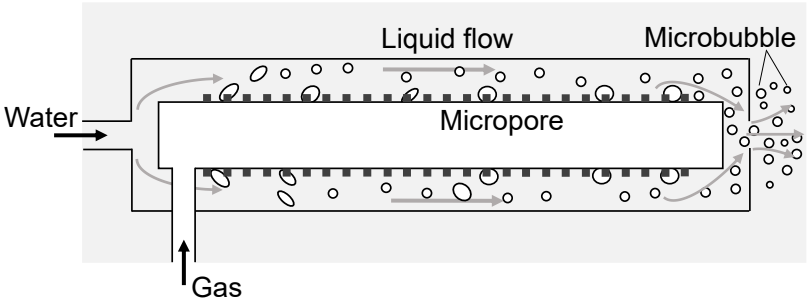

Fig. 1.9 Microbubble generator using microporous.

(c) Microporous pores method

This method is a microbubble generation method for gas miniaturization [52, 53]. The gas is supplied to a cylindrical section composed of a porous membrane with microporous pores as shown in Fig. 1.9. Bubbles exuding from the micropores on the sides of the cylinder and are cut off from the pores and flow downstream due to shear force exerted by the liquid flow perpendicular to the direction of bubble expansion in the annular flow of the double cylinder that surrounds the cylinder. The size and number density of microbubbles vary to some extent depending on the balance between the gas flow rate and liquid flow velocity.

Although there are other methods for generating microbubbles, an equipment for the generation of microbubbles can realize further cost reduction and miniaturization and can nicely change the relationship between the cleaning object and the cleaner/generator with respect to dirt is desired when considering their use in various fields.

1.6 Objectives

In order to investigate the removal mechanism of microbubbles, it is important to develop a measurement method to quantitatively evaluate the removal effects of microbubbles. In addition, the relationship between the bubble diameter, the bubble number density, and the bubble behavior in the vicinity of the object to be cleaned and the removal effect is important. Therefore, it is necessary to clarify not only the removal effects but also the relationship

between the bubble diameter and number density near the object to be cleaned and the removal effects. Furthermore, in order to fully demonstrate the performance of equipment using microbubbles, it is necessary to understand the change in diameter of microbubbles. Moreover, because conventional microbubble generators require the supply of liquid, there is a need for a compact and low-cost generation method that can generate microbubbles at any local location.

The objective of this study is to clarify the relationship between the behavior of microbubbles in the vicinity of oil and the removal process, and to investigate the diameter change of microbubbles and the generation mechanism of microbubbles, and to obtain design guidelines for the removal mechanism and new generators of microbubbles.

1.7 Structure of dissertation

This dissertation consists of five chapters. An overview of each chapter is given below.

In Chapter 1, as background of this study, the overview of previous research on the properties of microbubbles, fields of application, cleaning fields, and methods of generation was presented, and the issues related to the effects and properties of microbubbles that are the subject of this study were discussed. The purpose and methods of this study were described.

In Chapter 2, the purpose is to investigate the mechanism of the improvement of removal effect by microbubbles by continuously measuring the diameter and the number density of microbubbles and the change in the thickness of dirt in the vicinity, and quantitatively examining the influence of microbubbles on the removal of oil dirt. Experiments on the removal effects of water flows in a horizontal channel with and without microbubbles are therefore conducted to investigate the removal process by microbubbles. Silicone oil adhering to the bottom wall of the channel is used as dirt. The local thickness of the oil is measured during cleaning from micrographs of fluorescence intensity by laser-induced

fluorescence method.

In Chapter 3, a calculation method based on mass transfer is proposed to predict the diameter change of a single bubble and the bubble diameter distribution of a group of microbubbles with time. Numerical simulations based on the Rayleigh-Plesset equation are developed to investigate the time evolution of bubble diameter and the mass transfer of dissolved gas between bubbles and water in microbubble flow in a duct. Experiments on microbubbles in a water stream generated by a pressurized dissolution method are also conducted to investigate changes in the bubble size distribution of bubble groups and to obtain data for validation of the numerical method.

In Chapter 4, a method requires neither a pump nor a complex piping system, with which it is possible to generate bubbles in a stagnant liquid pool and at any local location, is developed. Since the bubble generation mechanism of the pressurized dissolution method is not based on effervescence but on shrink of the cavitation bubbles, subcooled boiling might be one of the candidates for the new microbubble generation method. Therefore, a microbubble generation method based on subcooled boiling on a thin metal wire is proposed. The generation process of microbubbles is observed using a high-speed camera to evaluate the bubble diameter and the number density. The experiments are conducted using resistance heating by direct current (DC) and alternating current (AC) in several electric power conditions.

In Chapter 5, the results and findings obtained in the previous chapters are summarized and the conclusions of this dissertation are given.

References for Chapter 1

[1] H. Onari, K. Maeda, K. Matsuo, Y. Yamahara, K. Watanabe, N. Ishikawa, Effect of micro-bubble technique on oyster cultivation, *Proceedings of hydraulic engineering*, vol. 46, 1163–1168, 2002.

[2] ISO 20480-1:2017(en) Fine bubble technology — General principles for usage and measurement of fine bubbles — Part 1: *Terminology*, 2017.

[3] M. Takahashi, K. Chiba, P. Li, Free-radical generation from collapsing microbubbles in the absence of a dynamic stimulus, *J. Phys. Chem. B*, vol. 111, 1343–1347, 2007.

[4] J. Zhang, K. C. Sahu, M. J. Ni, Transition of bubble motion from spiralling to zigzagging: A wake-controlled mechanism with a transverse magnetic field, *Int. J. Multiph. Flow*, vol. 136, 103551, 2021.

[5] C. H. Lee, S. Wongwises, D. W. Jerng, H. S. Ahn, Experimental study on breakup mechanism of microbubble in 2D channel, *Case Stud. Therm. Eng*., vol. 28, 101523, 2021.

[6] K. Tan, Y. Mohan, K. Liew, S. Chong, P. Poh, Development of an effective cleaning method for metallic parts using microbubbles, *J. Clean. Prod*., vol. 261, 121076, 2020.

[7] Y. Feng, H. Hu, G. Peng, Y. Zhou, Microbubble effect on friction drag reduction in a turbulent boundary layer, *Ocean Eng*., vol. 211, 107583, 2020.

[8] S. Tanaka, S. Kastens, S. Fujioka, M. Schlüter, K. Terasaka, Mass transfer from freely rising microbubbles in aqueous solutions of surfactant or salt, *Chem. Eng. J*., vol. 387, 121246, 2020.

[9] L. Parkinson, R. Sedev, D. Fornasiero, J. Ralston, The terminal rise velocity of 10–100 μm diameter bubbles in water, *J. Colloid Interface Sci*., vol. 322, 168–172, 2008.

[10] B. Swart, Y. Zhao, M. Khaku, E. Che, R. Maltby, Y.M. J. Chew, J. Wenk, In situ characterisation of size distribution and rise velocity of microbubbles by high-speed photography, *Chem. Eng. Sci*., vol. 225, 115836, 2020.

[11] R. Parmar, S. K. Majumder, Terminal rise velocity, size distribution and stability of microbubble suspension, *Asia-Pac. J. Chem. Eng.,* vol. 10, 450–465, 2015.

[12] J. R. Grace, T. Wairegi, T. H. Nguyen, Shapes and velocities of single drops and bubbles moving freely through immiscible liquids, *Trans. Inst. Chem. Eng*., vol. 54, 167–173, 1976.

[13] R. Clift, J. R. Grace, M. E. Weber, Bubbles, drops, and particles, *Courier Corporation*, 2005.

[14] W. E. Juwana, A. Widyatama, O. Dinaryanto, W. Budhijanto, Indarto, Deendarlianto, Hydrodynamic characteristics of the microbubble dissolution in liquid using orifice type microbubble generator, *Chem. Eng. Res. Des*., vol. 141, 436–448, 2019.

[15] K. Li, S. T. Matkarimov, W. Xiao, C. Liu, S. Yang, Fundamental study on the growth process of interfacial microbubbles in an air-supersaturated solution, *Colloids Surf. A Physicochem. Eng. Asp*., vol. 673, 131879, 2023.

[16] R. Parmar, S. K. Majumder, Microbubble generation and microbubble-aided transport process intensification—A state-of-the-art report, *Chem. Eng. Process*, vol. 64, 79–97, 2013.

[17] Y. Liu, Y. Zhou, T. Wang, J. Pan, B. Zhou, T. Muhammad, C. Zhou, Y. Li, Micro-nano bubble water oxygation: Synergistically improving irrigation water use efficiency, crop yield and quality, *J. Cle. Prod*., vol. 222, 835–843, 2019.

[18] S. T. M. Maung, R. Kokoo, M. Khangkhamano, Innovation in natural rubber latex coagulation using CO_2 microbubbles, *Chem. Eng. Process*., vol. 193, 109556, 2023.

[19] C. Oliveira, R.T. Rodrigues, J. Rubi, A new technique for characterizing aerated flocs in a flocculation-microbubble flotation system, *Int. J. Miner. Process*., vol. 96, 36–44, 2009.

[20] Y. Kaneko, T. Maruyama, K. Takegami, T. Watanabe, H. Mitsui, K. Hanajiri, H. Nagawa, Y. Matsumoto, Use of a microbubble agent to increase the effects of high intensity focused ultrasound on liver tissue, *Eur. Radiol*., vol. 15, 1415–1420, 2005.

[21] P. B. Vaidya, B. E. Oeffinger, R. Patel, Q. Lacerda, J. Powell, J. R. Eisenbrey, M. A. Wheatley, Shaping the synthesis of surfactant-stabilized oxygen microbubbles to accommodate encapsulated drug, *Colloids Surf. B*, vol. 208, 112049, 2021

[22] L. B. Chu, X. H. Xing, A. F. Yu, X. L. Sun, B. Jurcik, Enhanced treatment of practical textile wastewater by microbubble ozonation, *Process Saf. Environ. Prot.,* vol. 86, 389–393, 2008.

[23] P. P. F. Brasileiro, R. d. C. F. S. d. Silva, V. A. d. Santos, L. A. Sarubbo, M. Benachour, Efficiency of microbubble production using surfactants for the treatment of oily water by flotation, *Chem. Eng. Res. Des*., vol. 168, 254–263, 2021.

[24] W. Zhang, F. Jiang, Membrane fouling in aerobic granular sludge (AGS)-membrane bioreactor (MBR): Effect of AGS size, *Water Res*., vol. 157, 445–453, 2019.

[25] H. Minagawa, K. Fujiwara, R. Kurimoto, T. Yasuda, E. Harada, N. Hata, Effects of microbubbles on germination and growth of spinach, *Journal of JSEM*, vol. 16, 77–83, 2016.

[26] J.S Park, K. Kurata, Application of Microbubbles to hydroponics solution promotes lettuce growth, *HortTechnology*, vol. 19, 212–215, 2009.

[27] F. Kobayashi, H. Ikeura, S. Ohsato, T. Goto, M. Tamaki, Disinfection using ozone microbubbles to inactivate Fusarium oxysporum f. sp. melonis and Pectobacterium carotovorum subsp. carotovorum, *Crop Prot*., vol. 30, 1514–1518, 2011.

[28] H.L. Chen, R. D. Arcega, P.Y. Liao, C.Y. Hou, W.C. Liu, Y.R. Chen, J.S. Wu, W.R. Wang, C.M. Lin, Reduction of pesticides and bacteria on Napa cabbage by ozone microbubble water, *Postharvest Biol. Technol*., vol. 204, 112444, 2023.

[29] A. Endo, S. Srithongouthai, H. Nashiki, I. Teshiba, T. Iwasaki, D. Hama, H. Tsutsumi, DO-increasing effects of a microscopic bubble generating system in a fish farm, *Mar. Pollut. Bull*., vol. 57, 78–85, 2008.

[30] H. Tsutsumi, Application of microbubble injector to marine fish farming and its future perspective, *Bull. Soc. Sea Water Sci., Jpn*., vol. 64, 31–38, 2010.

[31] S. Liu, Q. Wang, H. Ma, P. Huang, J. Li, T. Kikuchi, Effect of micro-bubbles on coagulation flotation process of dyeing wastewater, *Sep. Purif. Technol*., vol. 71, 337–346, 2010.

[32] N. Jin, F. Zhang, Y. Cui, L. Sun, H. Gao, Z. Pu, W. Yang, Environment-friendly surface cleaning using micro-nano bubbles, *Particuology*, vol. 66, 1–9, 2022.

[33] A. A. Exner, M. C. Kolios, Bursting microbubbles: How nanobubble contrast agents can enable the future of medical ultrasound molecular imaging and image-guided therapy, *Curr. Opin. Colloid Interface Sci*., vol. 54, 101463, 2021.

[34] H. Yusefi, B. Helfield, The influence of inter-bubble spacing on the resonance response of ultrasound contrast agent microbubbles, *Ultrason. Sonochem.*, vol. 90, 106191, 2022.

[35] P.J Lin, M.C. Chuang, S.C. Chang, Research on the cleaning efficacy of micro-bubbles on dental plaque, *Procedia Manuf*., vol 3, 13–20, 2015.

[36] W. Lee, J. Shin, M. Lee, Y. Choi, H. Son, Y. Lee, Elimination efficiency of synthetic musks during the treatment of drinking water with ozonation and UV-based advanced oxidation processes, *Sci. Total Environ*., vol. 844, 156915, 2022.

[37] P. Tripathi, S. Tiwari, H. Tiwari, R. K. Sonwani, R. S. Singh, Techno-economic assessment of coupling ozonation and biodegradation process for the dye wastewater treatment, *J. Water Process. Eng*., vol. 56, 104286, 2023.

[38] P. B. Vaidya, B. E. Oeffinger, R. Patel, Q. Lacerda, J. Powell, J. R. Eisenbrey, M. A. Wheatley, Shaping the synthesis of surfactant-stabilized oxygen microbubbles to accommodate encapsulated drug, *Colloids Surf. B*, vol. 208, 112049, 2021.

[39] H. Yang, Z. Guo, Y. Li, H. Wang, Y. Dou, Experimental study on microbubble drag reduction on soil-steel interface, *Appl. Ocean Res*., vol. 116, 102891. 2021.

[40] L. J. Velasco, D. N. Venturi, D. H. Fontes, F. J. de Souza, Numerical simulation of drag reduction by microbubbles in a vertical channel, *Eur. J. Mech. B Fluids*., vol. 92, 215–225. 2022.

[41] N. Tamura, A. Kaneko, S. Uesawa, Y. Abe, M. Ike, Development of non-chemical micro-bubble washing technology using a Venturi tube, *Japanese J. Multiphase Flow*, vol. 27, 577–584, 2014.

[42] A. Fujimoto, K. Hattori, M. Oya, Effect of addition of surfactant on microbubble cleaning, *J. Jpn. Res. Assoc. Text. End-Uses*, vol. 57, 44–49, 2016.

[43] A. Fujimoto, K. Hattori, M. Oya, Removal of the surfactants adhered to the skin surface by the shower containing microbubble, *J. Home Econ.Jpn.*, vol. 67, 491–496, 2016.

[44] M. Takahashi, H. Ishikawa, T. Asano, H. Horibe, Effect of microbubbles on ozonized water for photoresist removal, *J. Photopolym. Sci. Technol*., vol. 28, 293–298, 2015.

[45] H. Minagawa, K. Sugimoto, R. Kurimoto, T. Yasuda, Basis study on immersion cleaning using microbubble water, *J. JSEM*, vol. 17, 298–303, 2017.

[46] K. Tabei, S. Haruyama, S. Yamaguchi, H. Shirai, F. Takakusagi, Study of micro bubble generation by a swirl Jet, *J. Environ. Eng.*, vol. 2, 172–182, 2007.

[47] K. Koide, S. Kato, Y. Tanaka, H. Kubota, Bubbles generated from porous plate, *J. Chem. Eng. Jpn*., vol. 1, 51–56, 1968.

[48] A. M. Aliyu, H. Seo, M. Kim, K. C. Kim, An experimental study on the characteristics of ejector-generated bubble swarms, *J. Vis*., vol. 21, 711–728, 2018.

[49] Y. Maeda, S. Hosokawa, A. Tomiyama, Y. Baba, Y. Ito, Generation mechanism of micro-bubbles in a pressurized dissolution method, *Exp. Therm. Fluid Sci*., vol. 60, 201–207, 2015.

[50] M. Sadatomi, A. Kawahara, K. Kano, A. Ohtomo, Performance of a new micro-bubble generator with a spherical body in a flowing water tube, *Exp. Therm. Fluid Sci.*, vol. 29, 615–623, 2005.

[51] Y. Wu, H. Chen, X. Song, Experimental and numerical study on the bubble dynamics and flow field of a swirl flow microbubble generator with baffle internals, *Chem. Eng. Sci*., vol. 263, 118066, 2022.

[52] M. Kukizaki, M. Goto, Size control of nanobubbles generated from Shirasu-porous-glass (SPG) membranes, *J. Membr. Sci*., vol. 281, 386–396, 2006.

[53] A. M. Trushin, E. A. Dmitriev, V. V. Akimov, Mechanics of the formation of microbubbles in gas dispersion through the pores of microfiltration membranes, *Theor. Found. Chem. Eng*., vol. 45, 26–32, 2011.

Chapter 2

Effects of microbubbles on removal of viscous oil from duct wall

2.1 Introduction

The cleaning process is important in the manufacturing and production processes of industrial products [1, 2], and in the food industry the removal of oil and grease from pipes is also necessary [3, 4]. However, conventional industrial cleaning uses chlorofluorocarbon gas [5, 6], volatile organic compounds [7], acid-alkali cleaning agents [8], and other chemicals [9], which pose environmental burdens, chronic health problems and waste liquid treatment costs [10, 11]. There is therefore a need to develop cleaning technologies with less environmental impact [12].

There have been many studies on cleaning using microbubbles. Lin et al. [13] used microbubbles to remove dental plaque in order to reduce a risk of periodontal disease. Takahashi et al. [14] reported that the use of ozone microbubbles generated by a pressurized dissolution method increased the concentration of ozonized water and improved the cleaning speed, but the cleaning efficiency was inferior to that of hot concentrated sulfuric acid, and the method has not yet been widely put to practical use. Matsuura et al. [15] carried out cleaning of polymer ink from a glass substrate using microbubbles. They suggested that the cleaning method should take into account microbubble adsorption onto ink surfaces to

improve the cleaning effects on hydrophobic materials. Factors that make water containing microbubbles effective for cleaning have been speculated as adsorption of dirt at the gas-liquid interface, an effect of surface charge, an abrasive effect of bubbles, a lifting effect of dirt by bubbles and so on [16–20] as shown in Fig. 2.1. However, none of the factors has been clearly demonstrated, and the detailed mechanisms related to the removal effect have not been fully elucidated. It is important to develop a measurement method to quantitatively evaluate the cleaning effect to clarify the cleaning process with microbubbles. Akuzawa et al. [21] proposed a method for continuously measuring the amount of removed lard oil based on temporal changes in the intensity of fluorescence generated by irradiation of a laser beam to the lard oil mixed with fluorescent dye (laser-induced fluorescence method). Although this method enables them to quantitatively evaluate the amount of removed oil, the effects of microbubbles on the oil-removal process could not be discussed in detail due to a lack of the information on the microbubble characteristics such as the number density and the diameter.

Experiments on the removal effects of water flows in a horizontal channel with and without microbubbles were conducted to investigate the oil removal process with microbubbles. Silicone oil adhering to the bottom wall of the channel was used as dirt. The local thickness of the oil was measured during cleaning from micrographs of fluorescence intensity from fluorescent dye mixed into the oil. The bubble diameter and the number density in the vicinity of the oil were also measured by using an image processing method. The behavior of microbubbles in the vicinity of the oil and its relation with the removal process are also discussed.

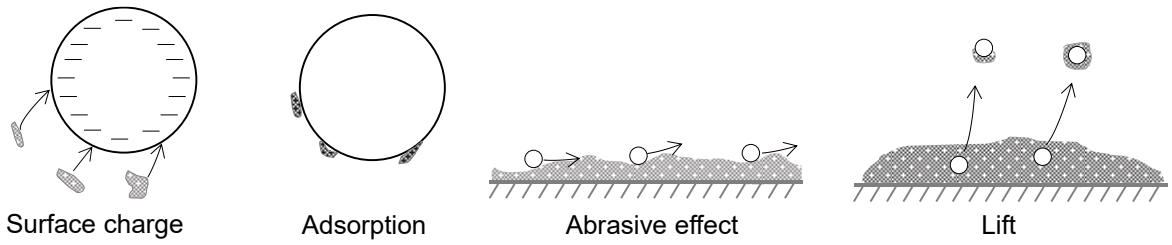

Fig. 2.1 Factors of microbubbles effective for cleaning.

2.2 Experimental apparatus and methods

2.2.1 Experimental setup and experimental conditions

Fig. 2.2 (a) shows a schematic of the experimental apparatus which consisted of a microbubble generator (Science, SMBO-PS480), an acrylic water tank, a pump (IWAKI, MD-6ZK), a flow meter (Nippon Flow Cell, NSP-5-B006), a test section, and an inverted microscope (Nikon, ECLIPSE Ti-U). The dimensions of the tank were 300 × 300 × 500 mm in width, depth and height, respectively. The tank was filled with water purified using a water purification system (Merck, Elix UV5). The water temperature T [K] and the dissolved oxygen concentration DO [kg/m^3] in the water tank were measured using a waterproof digital thermometer (Nekken, Safety Thermo, SN3000) and a luminescent dissolved oxygen meter (HACH, HQ30d LDO101-01), respectively. The temperature was $T = 298 \pm 0.5$ K and DO of purified water was $(8.45 \pm 0.2) \times 10^{-3}$ kg/m^3. During the experiment with flows containing microbubbles, the microbubble generator was operated for a sufficient time in advance to reach a quasi-equilibrium state in the tank, DO at which was $(9.65 \pm 0.2) \times 10^{-3}$ kg/m^3. Water was then started to flow into the channel by the pump. After passing through the test section, water flowed into a drain tank. The liquid volume flow rate was adjusted using valves installed in the flow path. The length of the experimental test was 350 mm and the oil was placed 200 mm downstream from the channel entrance.

The cross-section of the oil removal section is shown in Fig. 2.2 (b). The measurement section was a part of the bottom surface of the rectangular channel with the cross-sectional area of 5 and 10 mm in height and width, respectively. The area of the oil part was 4 mm × 4 mm and the depth was 200 μm. The bottom plate was removable, and the oil containing fluorescent dye was applied to a recess on the top surface of the protruding part of the bottom plate, which was then fixed in such a way that the oil interface was exposed to the water flow on the same plane as the bottom wall of the channel, i.e., flush mounted as shown in Fig. 2.2 (c). The initial thickness of oil was 200 μm and the change in the thickness could be measured without removing the test section, thereby enabling non-contact and continuous measurement of the oil thickness.

The experiments were carried out at Re = 250, 750, 5000 and 6750 with the uncertainty less than 1% so as to observe cleaning effects in laminar and turbulent flows, where Re is the Reynolds number defined by

$$Re = \frac{\rho \bar{u} d_H}{\mu} \tag{2.1}$$

Here ρ is the density of water (998 kg/m^3), μ the viscosity of water (0.89 mPa·s), $\bar{u}$ (= Q/S_c) the cross-sectional mean velocity, d_H (= $4S_c/P_e$) ~ 6.7 mm the hydraulic equivalent diameter, Q the liquid volume flow rate, S_c the channel cross-sectional area (50 mm^2), and P_e the perimeter of the channel (30 mm). The length, L_e, of the entrance section is usually recommended to be longer than $L_e = 0.058 d_H Re$ and $L_e = 30 d_H$ for laminar and turbulent flows, respectively, to achieve fully-developed states. As shown in Table 2.1 the present experimental setup satisfies the condition except for Re = 750. It will be shown in Section 2.3.1 the wall shear stress calculated using correlations for fully-developed state gives a reasonable explanation of cleaning rate, so that L_e was considered to be acceptable.

Table 2.1 Entrance length L_e.

Re	L_e [mm]
250	96
750	290
5000	200
6750	200

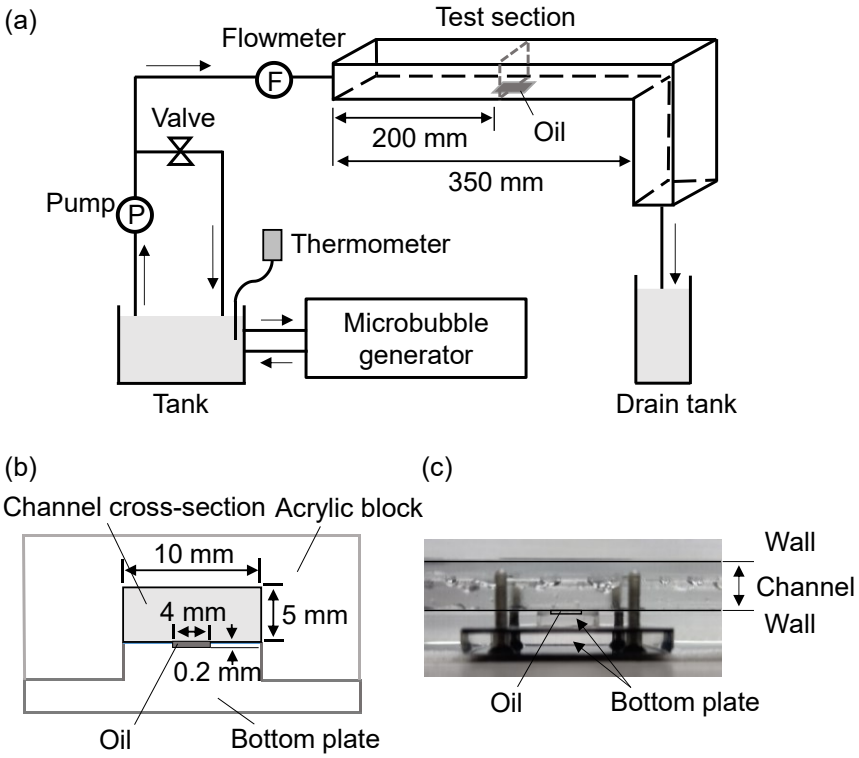

Fig. 2.2 Experimental apparatus. (a) Schematic of experimental setup. (b) Channel cross-section of test section. (c) Side view of test section.

2.2.2 Observation system and image analyses for oil thickness measurement

Fig. 2.3 shows a schematic of the optical system for observation using an inverted microscope. The test section was set on the stage, a high-speed camera (Photron, FASTCAM NOVA S12) was mounted on the camera port, and the microscope backlight or laser beam was illuminated according to the imaging conditions. The magnification of the objective lens (Nikon, S Plan Fluor 10×) was 10, and the resolution of the captured images was 2 μm/pixel. In the measurements of bubble diameter and bubble number density, the backlight was irradiated from above the test section and the transmitted light was recorded by the high-speed camera.

A laser beam was used to irradiate fluorescent dye in the oil for measuring the oil thickness, δ. *Coumarin* 6 (TCI) was used as fluorescent dye. The laser beam passed through a lens (SIGMAKOKI, DLB-26-120PM) placed between the inverted microscope and the laser source (Optic Electronic Co., Ltd.), which expanded the beam diameter at the focal point of the microscope and widened the region of fluorescence intensity measurement. The laser beam then entered the microscope horizontally through an access port located on the back of the microscope and was reflected by a dichroic mirror (Edmund Optics, DICHROIC LONG-PASS 500NM 25.2 × 35.6) installed at a 45-degree angle in the microscope. The laser beam was then irradiated onto the oil region. A rotary shutter was connected to a motor (ORIENTAL MOTOR Co, Ltd, SCM26JA-360) to control the irradiation time of the laser beam, and the speed was adjusted by a speed controller (US2D6-JA-CC). As shown in Fig. 2.3, the fluorescence emitted from the fluorescent dye in the oil by the laser beam passed through a dichroic mirror and a long-pass filter (Edmund Optics, PREC-ISION LONG-PASS 550NM 25MM). The high-speed camera connected to the camera port was used to take the fluorescence images every 30 s for 120 s, and the oil thickness was measured from the fluorescence intensity at each instant as will be described in Fig. 2.4. The shutter speed was 1/6000 s and the frame rate was 10 fps when measuring the oil thickness.

After 120 s, the microscope was used with a 4× objective lens (image resolution was 5 μm/pixel) and backlight to observe the removal process for a wider region and the behavior of microbubbles in the vicinity of the oil interface. The shutter speed was 1/16000 s and the frame rate was 10 fps.

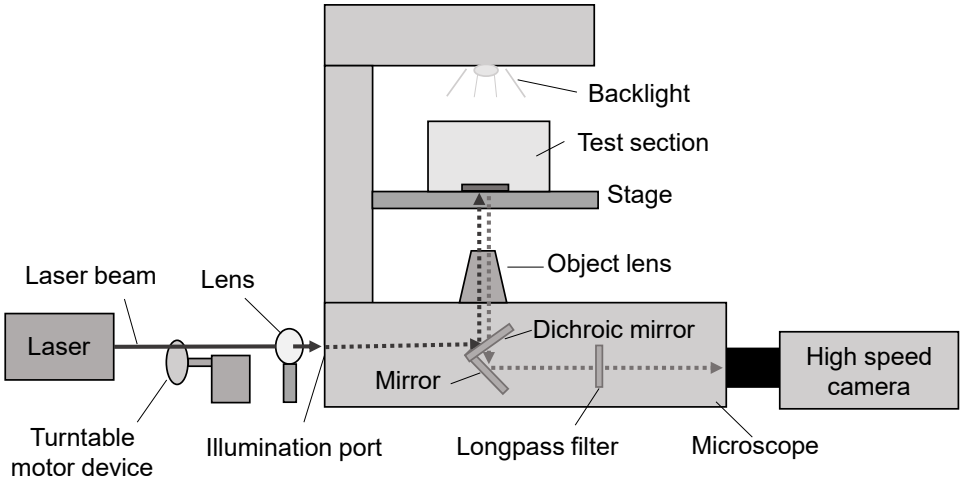

Fig. 2.3 Optical setup for micrography.

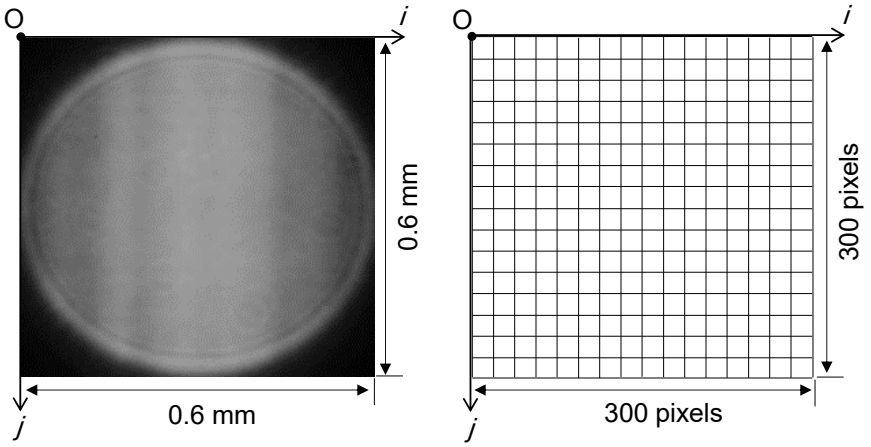

Fig. 2.4 An example of fluorescence image.

Fig. 2.4 shows a grayscale image (300 × 300 pixel) recorded for the oil thickness measurement. The spatial resolution of the image was 2 μm/pixel. The mean fluorescence intensity, $\bar{I}$, was obtained by averaging the local intensity (grey scale value), I_{ij}, of each pixel ij, that is

$$\bar{I} = \frac{\sum_{j=0}^{j=299}\sum_{i=0}^{i=299} M_{ij} I_{ij}}{\sum_{j=0}^{j=299}\sum_{i=0}^{i=299} M_{ij}} \tag{2.2}$$

where M_{ij} is a mask function which takes 1 for fluorescence region and 0 for background region.

When the fluorescence is irradiated with a laser beam, electrons of the fluorescent dye molecules are excited. Photons are emitted when returning from the excited state to the ground state. The number of emitted photons is proportional to the concentration, C, of the fluorescent dye in the sample, δ and the intensity, I_{LL}, of the laser light. The fluorescence intensity, I, can therefore be expressed as

$$I \propto CI_{LL}\delta \tag{2.3}$$

Two slide glasses (Artec, 8534) were set up as shown in Fig. 2.5 for validation of this relation. The gap between the slide glasses was filled with an oil, and the fluorescence intensity was measured by irradiating a laser beam from below. Moving from δ = 0.05 mm to 0.40 mm in 0.05 mm increments, images were taken at each position and the average fluorescence intensities were obtained. The relationship between δ and $\bar{I}$ is shown in Fig. 2.6. The linear increase in $\bar{I}$ with increasing δ shows that Eq. (2.3) is valid.

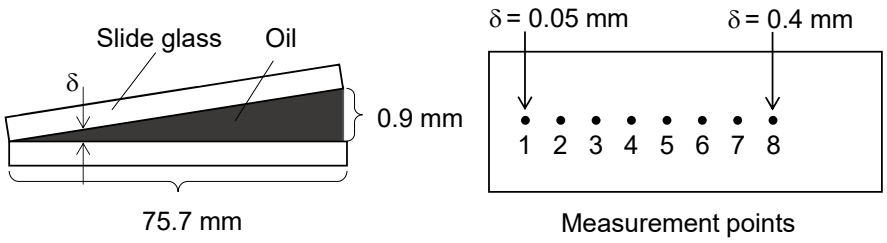

Fig. 2.5 Test cell and measurement points.

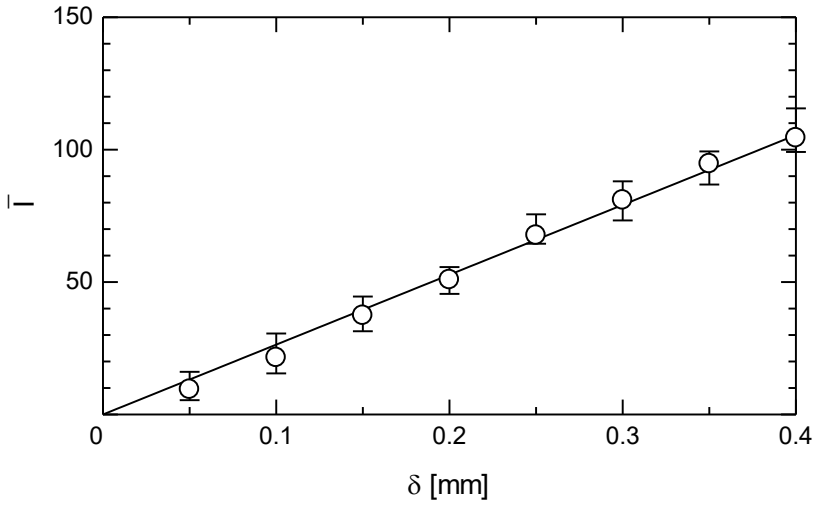

Fig. 2.6 Relation between oil thickness δ and fluorescence intensity $\bar{I}$.

It is known that fluorescent dyes exhibit a decrease in fluorescence intensity after prolonged exposure to laser light, i.e., photobleaching [22, 23]. Thus, it is necessary to understand the amount of fluorescence intensity reduction due to photobleaching to evaluate the oil thickness from $\bar{I}$. Fluorescence intensities for photobleaching without flow and for cleaning condition are denoted by $I_P(t)$ and $I_C(t)$, respectively. Since the initial thickness, δ(0), of the sample oil is constant, from Eq. (2.3), the fluorescence intensity and initial thickness are related as $I_P(0) = I_C(0) = CI_{LL}\delta(0)$. When confirming the photobleaching effect, the thickness $\delta(t)$ of the oil does not change because of no flow, i.e., $\delta(t) = \delta(0)$. The proportionality equation between $I_P(t)$ and δ(0) can therefore be expressed as

$$I_P(t) \propto CI_{LL}\delta(0)f(t) \tag{2.4}$$

where $f(t)$ is the decay rate of $\bar{I}$ due to photobleaching. In the oil removal experiment, the relationship between $I_C(t)$ and $\delta(t)$ can be expressed as (Fig. 2.7)

$$I_C(t) \propto CI_{LL}\delta(t)f(t) \tag{2.5}$$

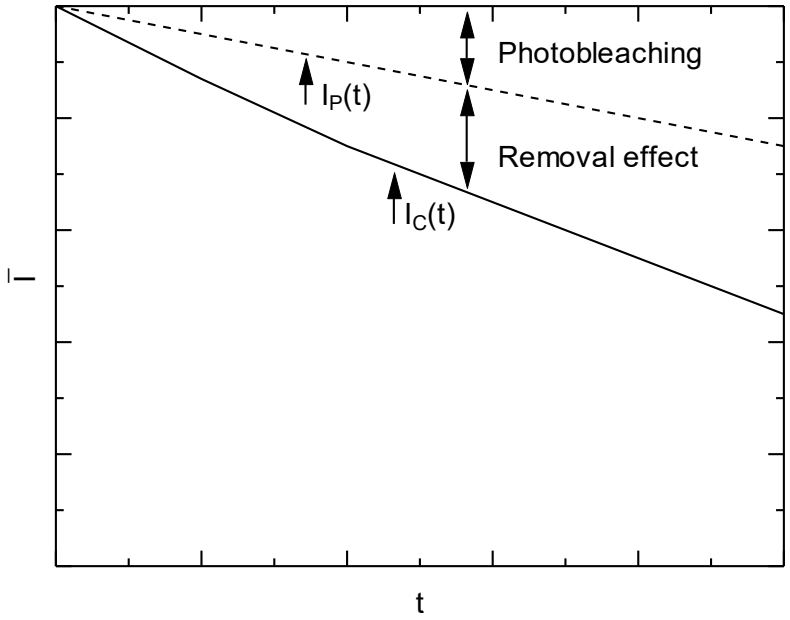

Fig. 2.7 Relationship between removal effect and photobleaching.

Substituting Eq. (2.4) into Eq. (2.5) yields

$$\delta(t) = \frac{I_C(t)}{I_P(t)}\delta(0) \tag{2.6}$$

The oil thickness can therefore be evaluated from I_P and I_C.

To reduce the influence by the variation in C and/or I_L in each experimental run, the normalized intensities were used:

$$\delta(t) = \frac{I'_C(t)}{I'_P(t)}\delta(0) \tag{2.7}$$

where $I'_C(t) = I_C(t)/I_C(0)$ and $I'_P(t) = I_P(t)/I_P(0)$. By obtaining $I_C(t)/I_C(0)$ and $I_P(t)/I_P(0)$, the thickness, $\delta(t)$, at each time can be obtained.

2.2.3 Evaluation methods of bubble diameter and number density

2.2.3.1 Image processing

(a) Image processing with average image

In the image processing, bubbles generated by using the microbubble generator were observed with a high-speed video camera (Photron, FASTCAM NOVA S12) as shown in Fig. 2.8 (a). The bubble diameter, d_B, and the number density, n_B, of microbubbles flowing through the measurement section were obtained by applying image processing to the captured images. When the captured image (Fig. 2.8 (a)) was processed as obtained, shades of gray that were not bubbles or bubbles that were stationary are also detected. Therefore, background removal was performed using the average intensity projection method. At first, an average image of all the images taken was created (Fig. 2.8 (b)), and then the average image was subtracted from each image taken as a background image to create an image showing only microbubbles passing through the measurement section of the cleaning effect (Fig. 2.8 (c)). This image was inverted and d_B and n_B were measured (Fig. 2.8 (d)). ImageJ (Ver. 1.49, Windows version) was used to calculate and subtract the average image.

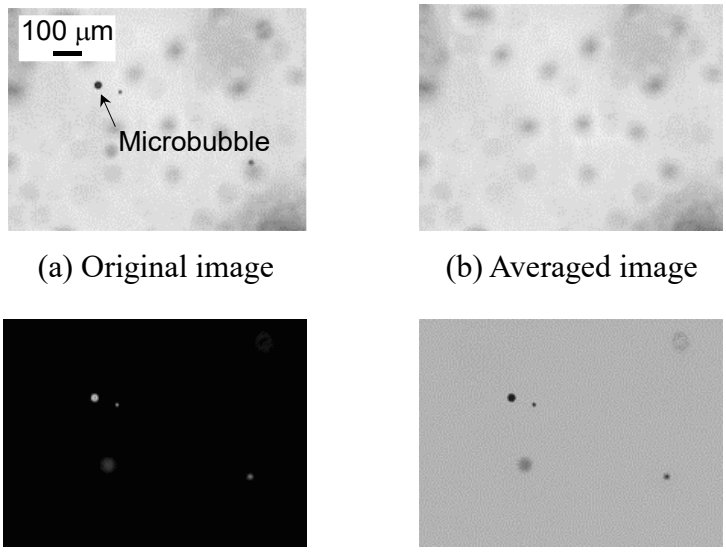

(a) Original image (b) Averaged image

(c) Subtracted image (d) Inverted image

Fig. 2.8 Image processing with average image.

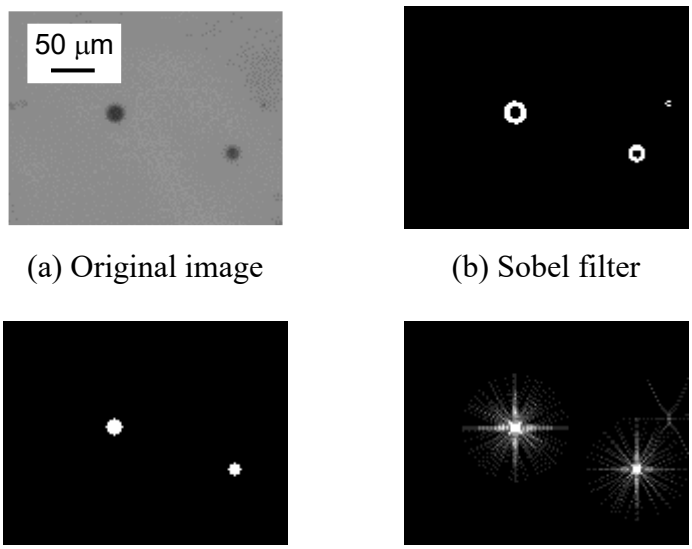

(a) Original image (b) Sobel filter

(c) Binary image (d) Normal Hough transform

Fig. 2.9 Image processing with contour and center detection.

(b) Detection of bubble and diameter calculation

The original image (Fig. 2.9 (a)) was Sobel filtered and binarized to detect bubble contours. The Sobel filter was a 3 × 3 pixel differential filter that produced a gradient of luminance. The luminance gradient was large for the contours of the in-focus image, and small for the out-of-focus bubbles and background. Therefore, by binarizing the Sobel-filtered image with a threshold value, only the bubble contours could be detected (Fig. 2.9 (b)). After detecting the contour of bubbles by the Sobel filter and binarization, bubbles in the focal plane were extracted (Fig. 2.9 (c)), and the geometric centers of bubbles were detected using the normal Hough transform (Fig. 2.9 (d)). The diameters of the detected bubbles were evaluated as the mean distances between the centers and the contours.

2.2.3.2 Evaluation of average bubble diameter and number density

The sphere-volume-equivalent diameter, d_{Bi}, of each bubble flowing in the vicinity of the oil interface was obtained using the above measurement method, where the subscript i is the index of bubbles detected in the images. The diameters of the detected bubbles were evaluated as the mean distances between the centers and the contours. The mean bubble diameter, $\overline{d}_B$, was then calculated as

$$\bar{d}_B = \frac{1}{N}\sum_{i=1}^{N} d_{Bi} \tag{2.8}$$

where N is the total number of bubbles detected.

The average number density, $\bar{n}_B$, of micro-bubbles was calculated as

$$\bar{n}_B = \frac{1}{H_{DOF}S}\left[\frac{1}{K}\sum_{j=1}^{K} N_{Bj}\right] \tag{2.9}$$

where K is the number of sample images (20,000), H_{DOF} is the depth of field (DOF, 310 μm), S is the measurement area, and N_{Bj} is the number of bubbles in the jth image. The resolution of the captured images was 2 μm/pixel, and therefore, the uncertainty of d_B is ±2 μm. The $\bar{d}_B$ was calculated from d_B of over 10,000 bubbles, the uncertainty in $\bar{d}_B$ was 2.4×10^{-2} μm, which is about 0.2% of the typical $\bar{d}_B$. The uncertainty in $\bar{n}_B$ was 5.4×10^{6} m^{-3}, which is about 0.8% of the typical value of $\bar{n}_B$.

The following shows a DOF measurement method. As shown in Fig. 2.10, DOF was determined as the distance at which a bubble was recognized by moving the stage of the inverted microscope in the depth direction, using the position at which the bubble was in focus as a reference. The image of the detected bubble is shown in Fig. 2.11. The diameter of the bubble shown in Fig. 2.11 is approximately 30 μm.

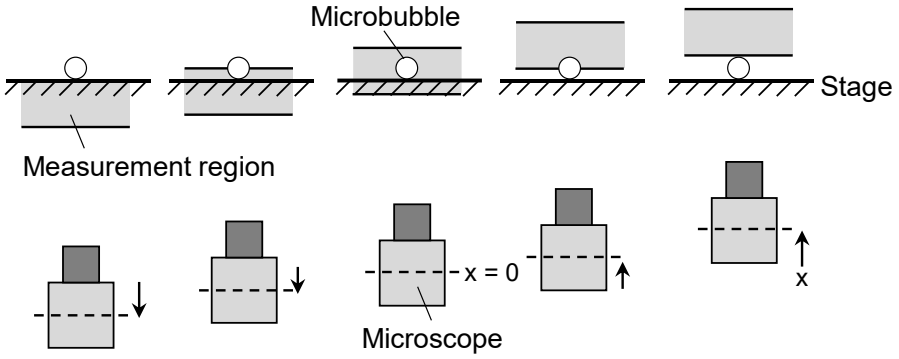

Fig. 2.10 Measurement of DOF.

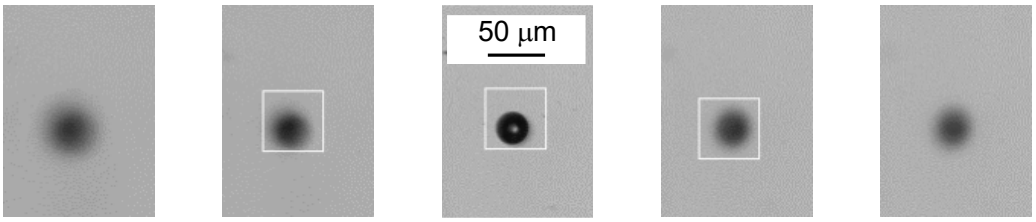

$x = -0.15$ mm $x = -0.14$ mm $x = 0$ mm $x = 0.17$ mm $x = 0.18$ mm

Fig. 2.11 Images of bubble detection.

2.3 Results and discussion

2.3.1 Influence of water flow on oil removal

Before discussing the removal effects by a water flow with microbubbles, the influence of water flow is investigated in this section. Two laminar flow conditions (*Re* = 250 and 750) and two turbulent flow conditions (*Re* = 5000 and 6750) were considered. Fig. 2.12 shows changes in δ until 120 s. The δ decreases with increasing time, and the amount of removed oil increases with increasing *Re*. Therefore, even without microbubbles, the water flow has a removal effect.

The relationship between the thickness decreasing rate, $-d\delta/dt$, and the shear stress, τ_W, is shown in Fig. 2.13, where $d\delta/dt$ is calculated by fitting a linear function to the $\delta(t)$ data and τ_W is estimated as

$$\tau_W = \frac{\lambda}{8}\rho\overline{u}^2 \tag{2.10}$$

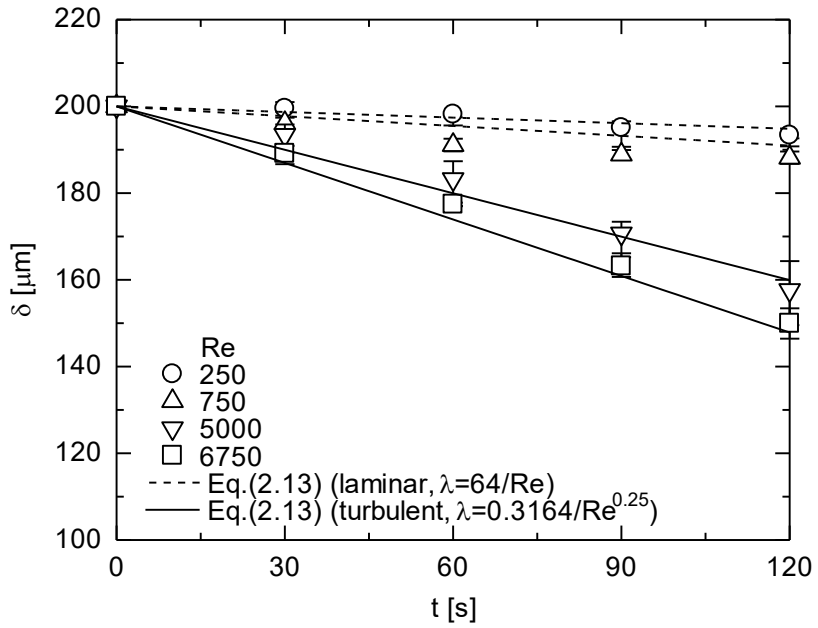

Fig. 2.12 Changes in oil thickness δ by water flow.

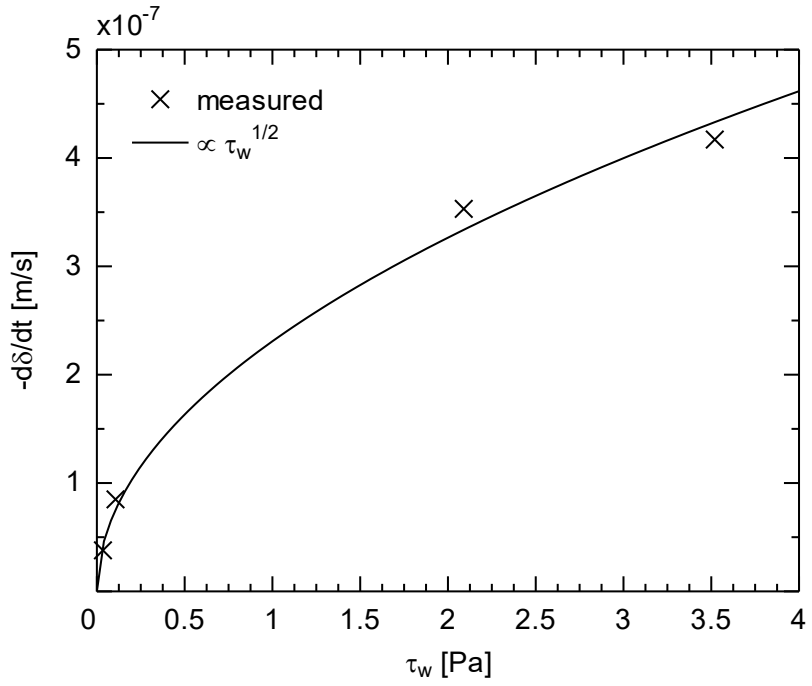

Fig. 2.13 Relation between $-d\delta/dt$ and τ_w of water flow.

$$\lambda = \begin{cases} \dfrac{64}{Re} & \text{for } Re < 2300 \\ \dfrac{0.3164}{Re^{0.25}} & \text{otherwise} \end{cases} \tag{2.11}$$

The removal rate increases as the shear stress increases and is proportional to $\tau_w^{1/2}$. Hence, it is assumed that the removal rate is proportional to the frictional velocity, $u^* = (\tau_w/\rho)^{1/2}$, i.e.

$$\frac{d\delta}{dt} = -c_s\sqrt{\frac{\tau_w}{\rho}} \tag{2.12}$$

where c_s is a dimensionless constant and its value was obtained as 7.3×10^{-6} by fitting Eq. (2.12) to the data. Integrating Eq. (2.12) yields

$$\delta(t) = \delta(0) - c_s\sqrt{\frac{\lambda}{8}}\bar{u}t \tag{2.13}$$

Eq. (2.13) is compared with the experimental data as shown in Fig. 2.12; the dashed lines are for the laminar flows, and the solid lines are for the turbulent flows. The correlation is consistent with the experiment. Hence, the oil removal by water flow is mainly due to the shear stress acting on the oil interface. Although the entrance length is somewhat shorter than the calculated value at Re = 750 shown in Table 2.1, the reasonable trend in Fig. 2.13 indicates that the flow was developed.

2.3.2 Influence of microbubbles on oil removal

Fig. 2.14 shows the probability density functions, $P(d_B)$, of d_B of bubbles within the region from the channel wall to 170 μm apart from the wall. The bin width was set to 5 μm. In all the conditions, the peak diameter around 20 μm slightly decreases as Re increases, implying that small microbubbles were brought to the near wall region against buoyancy due to turbulent fluctuations. The effects of Re on $\overline{d}_B$ and $\overline{n}_B$ are shown in Fig. 2.15. Increasing Re has no significant effect on $\overline{d}_B$ and $\overline{d}_B$ ~ 30 μm. On the other hand, $\overline{n}_B$ increases as Re increases.

Fig. 2.16 shows $\delta(t)$ in water flows with microbubbles. The δ decreases with time, and the amount of removed oil increases with increasing Re as well as in the water flow cases. Table 2.2 shows δ at 120 s in each case. The removal effects were confirmed to be enhanced by microbubbles whatever the Reynolds number is.

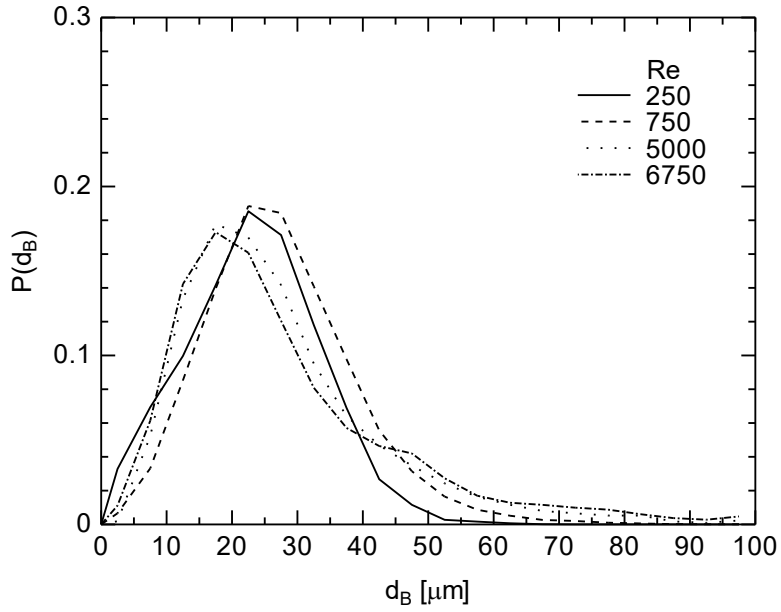

Fig. 2.14 Probability density function of bubble diameter.

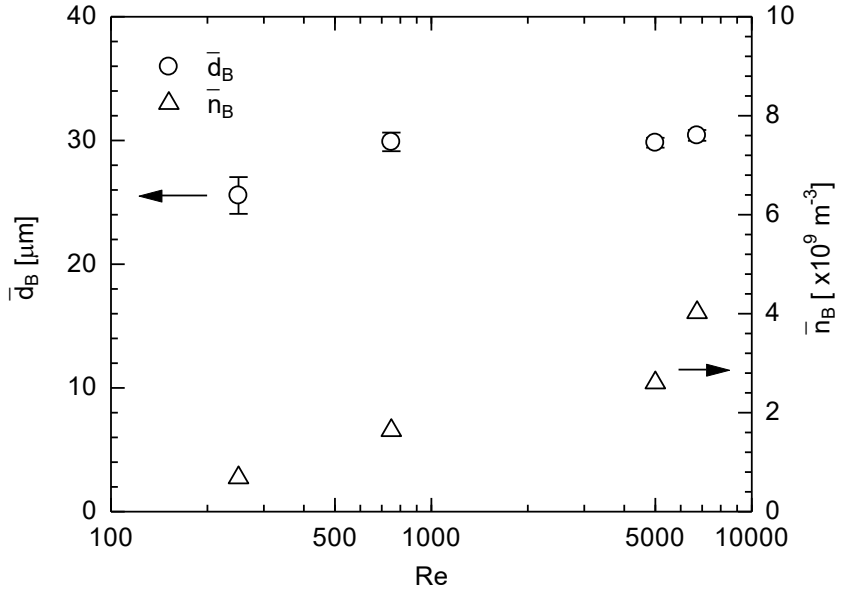

Fig. 2.15 Relation between *Re*, $\overline{d}_B$ and $\overline{n}_B$ of microbubbles.

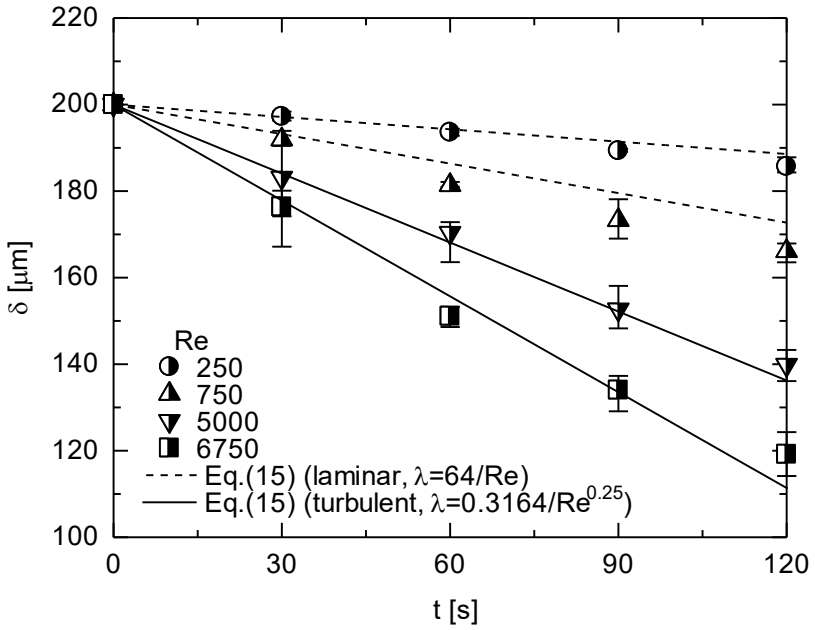

Fig. 2.16 Changes in oil thickness δ by water flow with microbubbles.

Table 2.2 Oil thickness at 120 s. The unit is [μm].

Re	250	750	5000	6750
Water flow	194	188	158	149
Microbubbles flow	186	168	136	114

Fig. 2.17 shows a relation between $\bar{n}_B$ and the removal rate excluding the effects of water flow, i.e., Eq. (2.12). It is shown that the effects of microbubbles increase almost linearly as $\bar{n}_B$ increases. Therefore,

$$\frac{d\delta}{dt} = -c_s\sqrt{\frac{\tau_w}{\rho}} - c_B L\bar{n}_B \tag{2.14}$$

where L is the distance from the oil interface, bubbles within which contribute to oil removal enhancement, and c_B [m^3/s] is a constant representing the amount of oil volume removed by a bubble. The L is approximated as $L \sim \bar{d}_B$, so that

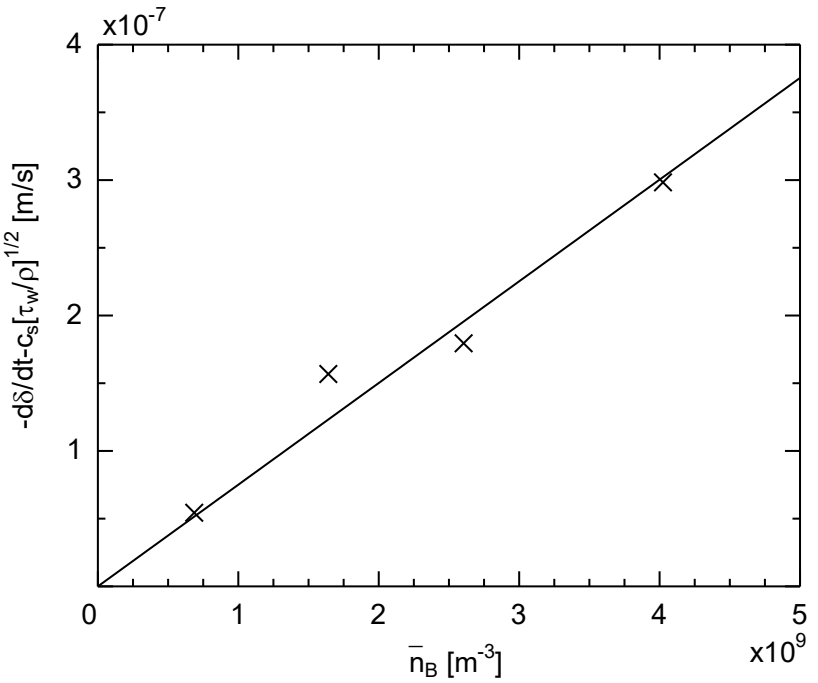

Fig. 2.17 Relation between $-d\delta/dt - c_s[\tau_w/\rho]^{1/2}$ and $\bar{n}_B$ of water flow.

$$\delta(t) = \delta(0) - \left(c_s \sqrt{\frac{\lambda}{8}} \bar{u} + c_B \bar{d}_B \bar{n}_B \right) t \tag{2.15}$$

By fitting this functional form to the data, we obtained $c_B = 3.8 \times 10^{-12}$ m^3/s. Eq. (2.14) is compared with the data in Fig. 2.16, in which the dashed lines are for the laminar flow cases and the solid lines are for the turbulent flow cases. The data and the correlation are in reasonable agreement, which demonstrates the validity of the model. The reason why the liquid velocity (*Re*) does not appear in the microbubble effect can be understood as follows: the increase in $\bar{u}$ increases the number of bubbles passing through the oil section per unit time. However, the residence time of bubbles in that section decreases. The former and the latter exhibit the proportionalities $\propto \bar{u}$ and $\propto \bar{u}^{-1}$, respectively, so that the flow rate effects are cancelled out and only $\bar{n}_B$ plays the role.

2.3.3 Adhesion of microbubbles on oil interface under turbulent flow condition

In the above sections, the removal effect was locally evaluated using the laser-induced fluorescence. In the microbubble experiment, the fluorescence intensity $\bar{I} = 0$ occurred after t = 240 s in the turbulent flow of Re = 6750. Fig. 2.18 shows the process of oil removal. Microbubbles attach to the water-oil interface and the number of adhering bubbles increases as t increases. The bubble size obviously becomes large. The large bubble indicated with the white circle at t = 330 s is swept away by the water flow in the direction of the black arrow. After that, a peeling-off indicated with the black dashed circle occurs from the original location of the large bubble. The peeling also expands with t in the direction of the white arrow shown in the image of t = 480 s.

Fig. 2.19 shows the process of large bubble generation, where t' is the time at which the bubbles attach to the oil interface and get larger. The state of microbubble adhesion and growth is shown in Fig. 2.19 (a). Large bubbles coming from the upstream could not attach to the oil, and only microbubbles did due to turbulent fluctuations. In addition, the attached microbubbles became larger and coalesced with other bubbles around them as shown in Fig. 2.19 (b). The coalescence of such bubbles resulted in bubbles reaching a certain degree of size, and they were pushed and swept away by the water flow, followed by peel-off.

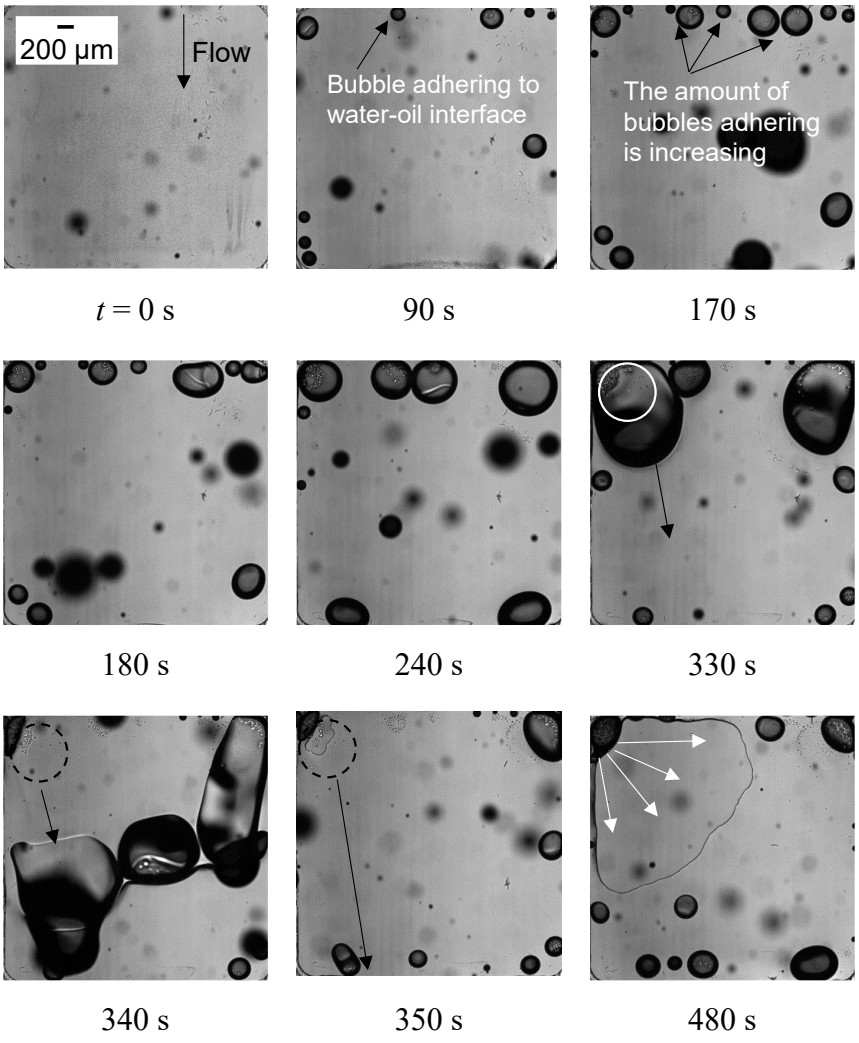

Fig. 2.18 Processes of oil removal with bubble detachment (*Re* = 6750).

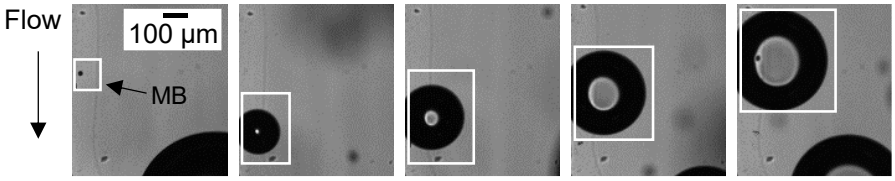

(a) Attachment and growth of microbubble.

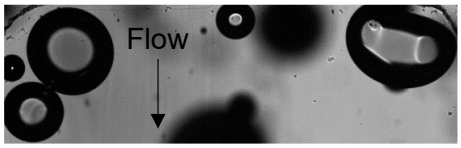

t' = 198 s

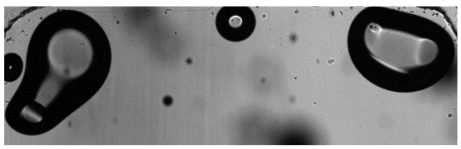

200 s

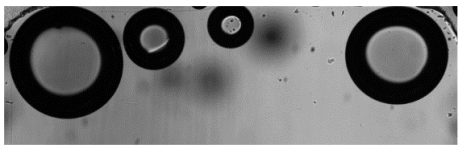

252 s

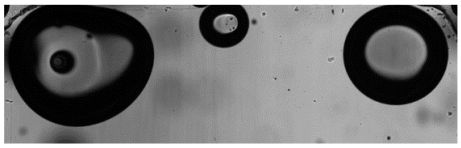

267 s

(b) Bubble coalescence.

Fig. 2.19 Microbubble attachment and bubble coalescence.

Let us check whether the growth of microbubbles is caused by coalescence or mass transfer of gaseous species from water to the bubbles. Water with microbubbles was made to flow into the channel, and then the flow was stopped immediately after some microbubbles attached to the oil. This condition is referred to as the stagnant water condition in the following. The relationship between d_B and t' in the stagnant water condition is shown in Fig.

2.20; microbubbles can grow by mass transfer of oxygen from water without coalescing with each other. A relation between d_B and t' in the water flow is also shown in Fig. 2.20. In the microbubble flow, DO in the tank was kept at 9.65×10^{-3} kg/m^3 due to the continuous generation of microbubbles. That is, it provided the same DO in the vicinity of the oil, regardless of time. The growth rate in the bubbly flow was the same as in the stagnant water at the initial growth stage and, thus, microbubbles can grow by mass transfer without coalescing in microbubble flow. After 90 s, the microbubbles in the bubbly flow grew faster after a certain time if no coalescence occurred in the bubbly flow. The data of the microbubble flow in Fig. 2.20 depart from those of the stagnant flow case after 120 s. This is due to bubble coalescence with surrounding bubbles. The bubble size became larger than 300 μm and coalesced with another large bubble, which causes the jump in the data plots at 240 s as shown in Fig. 2.21.

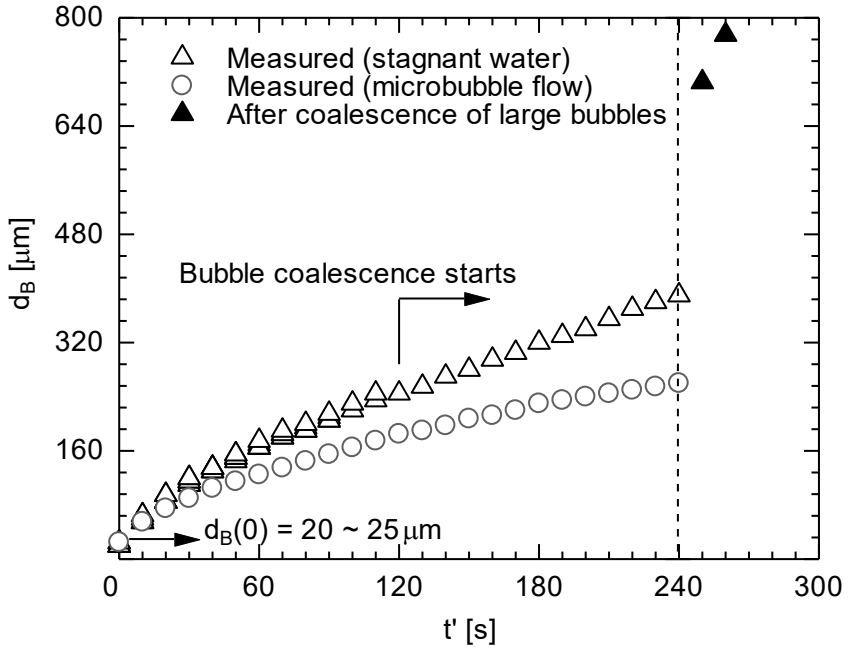

Fig. 2.20 Relation between d_B and t' in stagnant water and microbubbles flow.

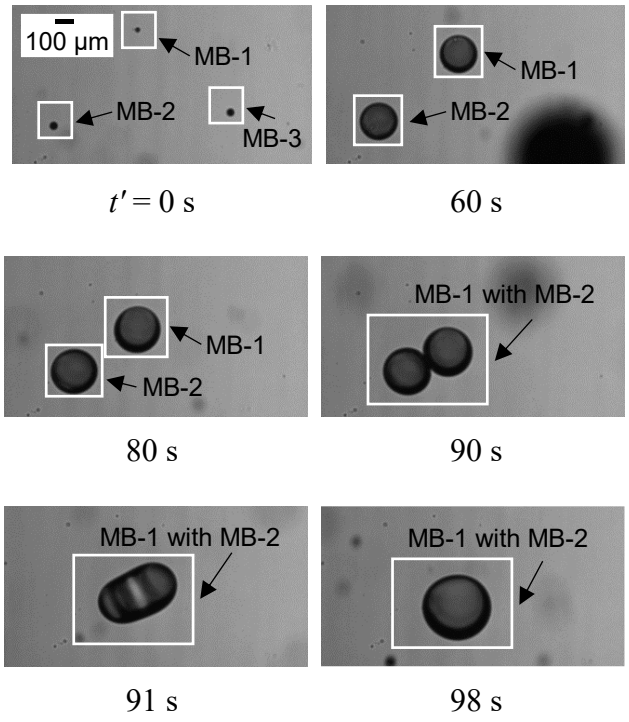

Fig. 2.21 Microbubbles (MB) grow to a certain degree and coalesce with other bubbles.

It is important to observe the condition under which the peeling occurs and to evaluate the extent of the peeling. Fig. 2.22 (a) shows the state of oil at t = 600 s in the water flow of Re = 750 with microbubbles. The fluorescence intensity measurement showed the decrease in thickness under this condition, but no peeling off was observed. The black shading regions in the image indicate bubbles in water and on the upper wall of the channel outside the focal plane. In this experiment, the microbubbles did not adhere to the interface, resulting in no peeling in the laminar flow even with microbubbles. Fig. 2.22 (b) shows oil images in the turbulent flow of Re = 6750 without microbubbles at t = 600 s and 720 s. No peeling was observed in these flows. Fig. 2.22 (c) shows the state of the oil in the turbulent flow with microbubbles. At t = 600 s, peeling of oil occurred and the area of peeling expanded with time. Fig. 2.23 shows the ratio of the area, in which peel-off takes place, to the area of oil region (4 mm × 4 mm). Peeling began around t = 380, and the peel-off rate increased with time.

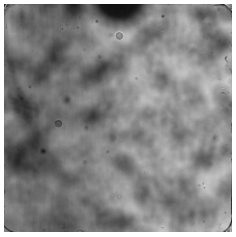

t = 600 s

(a) Microbubbles flow in laminar flow (Re = 750).

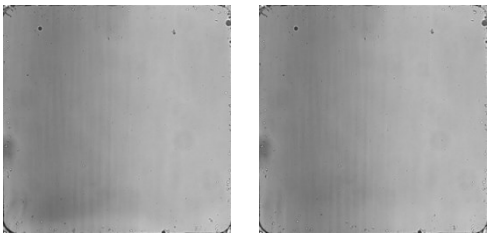

t = 600 s 720 s

(b) Water flow in turbulent flow (Re = 6750).

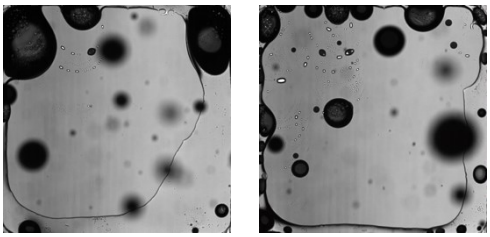

t = 600 s 720 s

(c) Peel-off of microbubbles flow in turbulent flow (Re = 6750).

Fig. 2.22 Microbubble adhesion and peel-off.

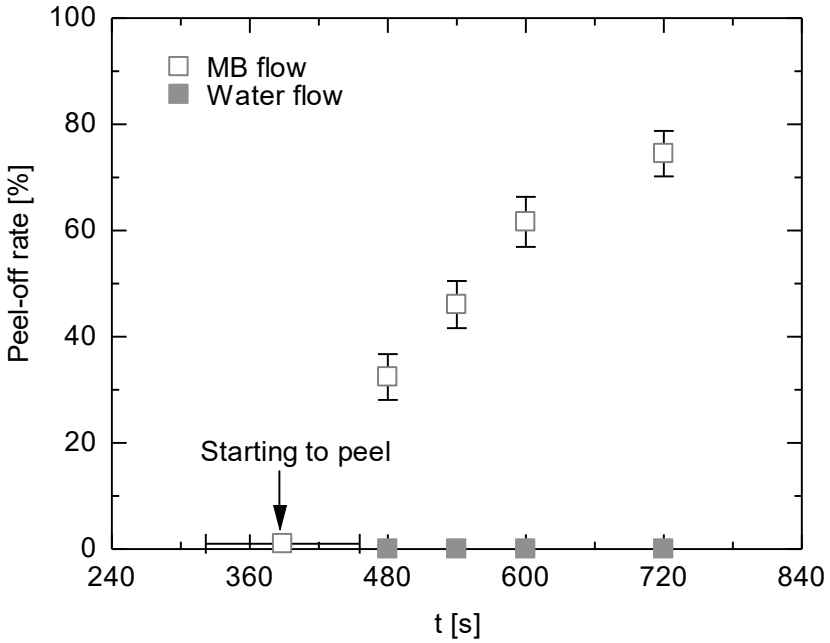

Fig. 2.23 Relation between peel-off rate and t (Re = 6750).

Fig. 2.24 shows a schematic of the whole process of oil removal. In the early stage (the left part of the figure), oil removal is mainly due to the shear stress acting on the oil interface, and when microbubbles are mixed, the microbubble effect is superposed. In a turbulent bubbly flow at high Re, microbubbles attach to the water-oil interface, and those bubbles grow by mass transfer of gas species from water and the bubble growth initiates bubble coalescence from $t \sim 120$ s. Bubbles that have grown by bubble coalescence are swept away by the water flow, which results in peel off around $t = 380$ s (the right part of the figure). The overall residual adhering rate decreases with time.

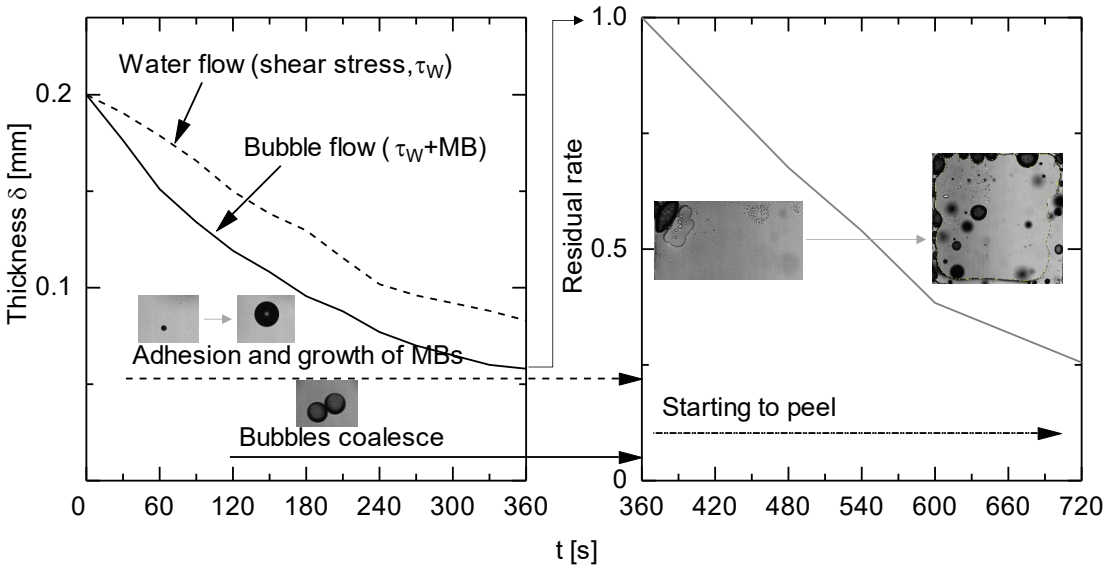

Fig. 2.24 Process of removing oil by water flow with microbubble (turbulent flow condition).

2.4 Conclusions

Oil removal experiments were conducted using viscous silicone oil adhering to the bottom wall of a horizontal rectangular channel to investigate the effects of microbubbles on the removal of oil on the wall surface. The fluorescence intensity of the fluorescent dye mixed in the silicone oil was photographed by a microscope to measure the change in oil thickness, and the bubble diameter and number density in the vicinity of the wall surface were also measured to investigate the removal rate enhanced by microbubbles. As a result, the following results were obtained:

(1) The amount of oil removed by the water flow increases with increasing *Re*, showing that the water flow has cleaning effects even without microbubbles. This is attributed to the shear stress acting on the oil interface.

(2) Adding microbubbles to the water flow increases the amount of oil removal. In other words, microbubbles have a removal enhancement effect. The higher the bubble number density, the larger the removal effect is. The removal effect of microbubbles can be evaluated by a model that assumes that the amount of oil removal is proportional to the number of microbubbles in the vicinity of oil interface.

(3) The removal rate can be modeled as a superposition of the effects of shear stress and the presence of microbubbles.

(4) Microbubbles adhering to oil under turbulent conditions can be grown by mass transfer. The cleaning effect is largely promoted by peeling of the oil by the detachment of large bubbles grown on the oil interface.

References for Chapter 2

[1] A. T Bull, A. W Bunch, G. K Robinson, Biocatalysts for clean industrial products and processes, *Curr. Opin. Microbiol*., vol. 2, 246–251, 1999.

[2] K. Kishimotto, J. Nakajima, T. Moriyasu, S. Shigeoka, H. Kamimura, The cases of cleaning validation in pharmaceutical factories, *Ann. Rep. Tokyo Metr. Res. Lab. P.H*., vol. 52, 33–37, 2001.

[3] S. Liu, Q. Wang, H. Ma, P. Huang, J. Li, T. Kikuchi, Effect of micro-bubbles on coagulation flotation process of dyeing wastewater, *Sep. Purif. Technol*., vol.71, 337–346, 2010.

[4] J.B. Williams, C. Clarkson, C. Mant, A. Drinkwater, E. May, Fat, oil and grease deposits in sewers: Characterisation of deposits and formation mechanisms, *Water Res*., vol. 19, 6319–6328, 2012.

[5] E. Kikuchi, Y. Kikuchi, M. Hirao, Analysis of risk trade-off relationships between organic solvents and aqueous agents: case study of metal cleaning processes, *J. Cleaner Prod*., vol. 19, 414–423, 2011.

[6] M.A. Ilgin, S.M. Gupta, Remanufacturing Modeling and Analysis, *CRC Press*, *New York*, 2012.

[7] B. C. Singer, B. K. Coleman, H. Destaillats, A. T. Hodgson, M. M. Lundin, C. J. Weschler, W. W. Nazaroff, Indoor secondary pollutants from cleaning product and air freshener use in the presence of ozone, *Atmospheric Environ*., vol. 40, 6696–6710, 2006.

[8] Y.Y. Liu, R. J. Haynes, Influence of different acid and alkaline cleaning agents on the effects of irrigation of synthetic dairy factory effluent on soil quality, ryegrass growth and nutrient uptake, *Environ. Sci. Pollut. Res*., vol. 20, 498–507, 2012.

[9] B. Moniz, J. W. Horvath, Chemical cleaning and cleaning-related corrosion of process equipment, *ASM International*, 2006.

[10] O. Dumas, N. Le Moual, Damaging effects of household cleaning products on the lungs, *Expet Rev. Respir. Med*., vol. 14, 1–4, 2020.

[11] Y. Zhao, L. Gao, F. Zha, X. Chen, X. Zhou, X. Wang, Y. Chen, X. Pan, Research on heavy metal level and co-occurrence network in typical ecological fragile area, *J. Environ. Health Sci. Eng*., vol. 19, 531–540, 2021.

[12] E. Sisco, M. Najarro, A. Burns, Quantifying the effectiveness of cleaning agents at removing drugs from laboratory benches and floor tiles, *Forensic Chem*., vol. 12, 1–7, 2019.

[13] P.J. Lin, M.C. Chuang, S.C. Chang, Research on the cleaning efficacy of micro-bubbles on dental plaque, *Procedia Manuf*., vol. 3, 13–20, 2015.

[14] M. Takahashi, H. Ishikawa, T. Asano, H. Horibe, Effect of microbubbles on ozonized water for photoresist removal, *J. Phys. Chem. C*., vol. 116, 12578–12583, 2012.

[15] K. Matsuura, S. Ogawa, S. Kasaki, K. Koyama, M. Kodama, S. Yanase, Cleaning polymer ink from a glass substrate using microbubbles generated by a hydrogen bubble method, *Sep. Purif. Technol*., vol. 142, 242–250, 2015.

[16] I.D. Sta Maria, M.W. Lim, E.V. Lau, Multiple roles of gra- phene nanoparticles (GNP) in microbubble flotation for crude oil recovery from sand, *Results Eng*., vol. 11, 100271, 2021.

[17] L. Cao, Q. Liu, Y. Peng, The surface energy and surface charge of microbubbles generated by frother surfactants, *J. Mol. Liq*., vol. 372, 121201, 2023.

[18] M. Miyamoto, S. Ueyama, N. Hinomoto, T. Saitoh, S. Maekawa, J. Hirotsuji, Degreasing of solid surfaces by microbubble cleaning, *Jpn. J. Appl. Phys*., vol. 46, 1236–1243, 2007.

[19] L. Cao, X. M. Chen, Y. J. Peng, The adsorption and orientation of frother surfactants on heterogeneous wetting surfaces, *Appl. Surf. Sci*., vol. 548, 149225, 2021.

[20] H. Zhang, Z. Lu, P. Zhang, J. Gu, C. Luo, Y. Tong, X. Ren, Experimental and numerical investigation of bubble oscillation and jet impact near a solid boundary, *Optics & Laser Technology*, vol. 138, 106606, 2021.

[21] H. Akuzawa, K. Amagai, M. Funatsu, F. Takakusagi, K. Tabei, Y. Noda, Study on cleaning of pipe inner wall by micro-bubble flow, *Jpn. J. Multiph. Flow*., vol. 24, 454–461, 2010.

[22] N. Klonis, M. Rug, I. Harper, M. Wickham, A. Cowman, L. Tilley, Fluorescence photobleaching analysis for the study of cellular dynamic, *Eur. Biophys. J*., vol. 31, 36–51, 2002.

[23] S. Khandai, R.A. Siegel, S.S. Jena, Probing the micro- environment of polyacrylamide hydrogel matrix using tur- bidity and fluorescence recovery after photobleaching: One versus Two phases. Colloids Surf. A Physicochem, *Eng. Asp. vol*., 593, 124618, 2020.

Chapter 3

Numerical prediction of microbubbles in water with mass transfer

3.1 Introduction

The diameter, d_B, and the number density, n_B, of microbubbles are important factors in the development and improvement of the applications, and the control of these factors is required for microbubble generators [1]. Many studies have therefore reported d_B and n_B of microbubbles in bubble-generation systems such as a swirl-type [2], a Venturi-type [3], a shear-type [4], a pressurized-dissolution-type [5–7] and microporous pores-type [8]. However, both d_B and n_B would change in time after generation due to the mass transfer between bubbles and the surrounding liquid. The microbubbles adhering to the oil interface grow by mass transfer and the detachment of grown bubbles from the oil interface largely contributes to removal of oil from a flow channel as discussed in Section 2.3.3. On the other hand, Ward et al. [9–11] reported that a bubble shrinks in a dilute solution of oxygen in water. The cause of these opposite trends (growth/shrinkage) can be understood from the direction of mass transfer depending on the gaseous species concentration in the liquid as described in Section 1.2.

A bubble of d_B smaller (larger) than the equilibrium diameter, d_{Beq}, will shrink (grow). Microbubbles in liquid flows are usually poly-dispersed and may grow or shrink depending

on their size and d_{Beq}, resulting in a change in the bubble size distribution. A method for predicting the temporal change in the size distribution would therefore be useful for design and development of the applications utilizing microbubbles. Although the time evolution of a single bubble has been studied so far [12, 13], that of the size distribution of microbubbles has been rarely investigated.

In this chapter, numerical predictions of the mass transfer for single microbubbles and microbubble groups were carried out, and the validity of the predictions was discussed through comparisons with experimental data.

3.2 Numerical method

3.2.1 Single bubbles

The gas volume fraction, α, in a water flow containing microbubbles is usually low. The mass transfer between each bubble and the surrounding water can therefore be approximated as that of an isolated bubble in water. In addition, the slip velocity is very small, so that the diffusion governs the mass transport near a bubble. Hence, the numerical model of Takahira et al. [14], in which the Rayleigh–Plesset equation [15] is coupled with the one-dimensional advection-diffusion equation in the polar-coordinate system, for a single spherical bubble in an infinite stagnant liquid is employed as the basis of the present numerical method.

The Rayleigh–Plesset equation is given by

$$R\frac{d^2R}{dt^2}+\frac{3}{2}\left(\frac{dR}{dt}\right)^2=\frac{1}{\rho_L}\left[p_B-\frac{1}{R}\left(2\sigma+4\mu\frac{dR}{dt}\right)-p_L\right] \tag{3.1}$$

where R is the bubble radius, t the time, ρ_L the liquid density, and μ the liquid viscosity. The p_B is given by

$$p_B=\frac{3NR_GT}{4\pi R^3} \tag{3.2}$$

where N is the number of moles in a bubble, R_G the gas constant, and T the absolute temperature. The system is assumed to be isothermal. The concentration, C_i, of the ith gas species in water is calculated by solving the following one-dimensional advection-diffusion equation:

$$\frac{\partial C_i}{\partial t}+u_r\frac{R^2}{r^2}\frac{\partial C_i}{\partial r}=\frac{1}{r^2}\frac{\partial}{\partial r}\left(r^2D_i\frac{\partial C_i}{\partial r}\right) \tag{3.3}$$

where D is the diffusion coefficient, and u_r (= dR/dt) the velocity normal to the interface. The Cs is given by

$$C_{Si} = C_{H_2O} \frac{p_B y_i}{H_i} \tag{3.4}$$

where C_{H2O} is the concentration of water, and y the molar fraction. The concentration, C_∞, far from a bubble is given as the bulk concentration. The mass transfer rate, $\dot{m}_i$, through the gas-liquid interface is given by

$$\dot{m}_i = 4\pi R^2 D_i \left. \frac{\partial C_i}{\partial r} \right|_{r=R} \tag{3.5}$$

When the concentration of a substance is non-equilibrium between gas and liquid, mass transfer through the interface occurs, and the amount of mass transfer is determined by the concentration gradient at the interface. The following is a description of the solution algorithm for the above set of equations:

(1) The time variation of the bubble diameter is obtained by solving the Rayleigh–Plesset equation Eq. (3.1). p_B in Eq. (3.1) is calculated by the equation of state, Eq. (3.2).

(2) u_r (= dR/dt) is determined from the solution of (3.1). The one-dimensional advection-diffusion equation, Eq. (3.3), is then solved using the finite difference method to obtain the concentration distribution in the liquid phase. As for the boundary condition at the interface, the molar concentration of dissolved bubbles at the gas-liquid interface is calculated by Henry's law using Eq. (3.4).

(3) The mass transfer rate, $\dot{m}_i$, of the gas component i in the bubble is calculated using Eq. (3.5), the pressure inside the bubble changes as the size and composition of the bubble change.

The loop from (1) to (3) is repeated.

The fourth-order Runge–Kutta [16] and the second-order centered difference schemes are used for the temporal and spatial differentiations, respectively.

3.2.2 Bubble groups in liquid flows

In simulations of microbubbles in water flows, the following assumptions are made in addition to the single bubble simulations:

(1) The interaction between microbubbles is negligible.
(2) The distributions of the concentrations of gas species around a bubble are not affected by the liquid flow.
(3) The concentration of gas species, the bubble number density and the bubble size distribution are uniform in the cross-section of a flow.
(4) Bubbles are moving with the liquid flow.
(5) Bubble coalescence and nucleation are negligible.

When microbubbles are observed in a coordinate system moving with water flow in the duct (Fig. 3.1 (a)), the mass transfer between each bubble and surrounding water can be approximated by that of an isolated bubble in stagnant water. Fig. 3.1 (b) shows a schematic of the method to predict the bubble size distribution. The microbubbles are classified into 150 bubble size classes (1–150 μm with 1 μm step), and d_B^j of bubbles in the *j*th bubble-size class is calculated by using the method described in Sec. 3.2.1. The mass transfer rate, $\dot{m}_i^j$, of the *j*th class in a unit volume is evaluated by multiplying the mass transfer rate, $\dot{m}_{SBi}^j$, of the single bubble and the number density, n_B^j, of bubbles in the class:

$$\dot{m}_i^j = n_B^j \dot{m}_{SBi}^j \tag{3.6}$$

The total mass transfer rate, $\dot{m}_{Ti}$, of bubbles in all the classes is evaluated as

$$\dot{m}_{Ti} = \sum_j \dot{m}_i^j \tag{3.7}$$

The increase in $C_{\infty i}$ is then given by solving the following equation:

$$\frac{dC_{\infty i}}{dt} = -\dot{m}_{Ti} \tag{3.8}$$

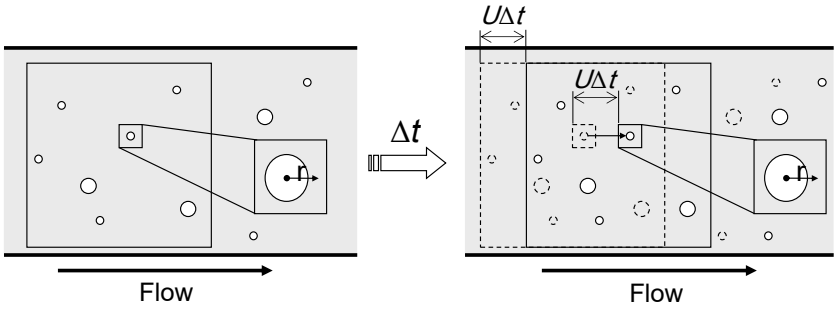

(a) Water flow in the duct.

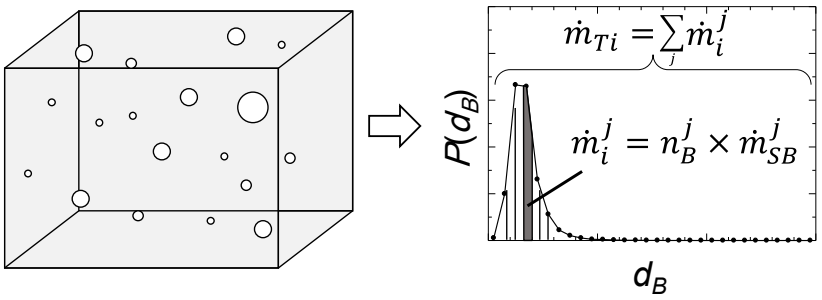

(b) Size distribution.

Fig. 3.1 Schematic of simulated system.

3.2.3 Influence of each numerical parameter on prediction of d_B

In this section, the effects of parameters used in the calculations, such as the time step, Δt, and the grid spacing, Δr, on the calculation results are discussed. Table 3.1 shows the calculation conditions and the physical constants used to investigate the effect of each parameter [17, 18], where d_{B0} is the initial bubble diameter, p_{vaper} the saturation water vapor pressure, and y_i the mole fraction of the i-component.

Table 3.1 Numerical conditions.

T	[K]	298
ρ_L	[kg/m^3]	997
μ	[Pa·s]	8.94×10^{-4}
p_0	[Pa]	1.013×10^5
σ	[N/m]	7.13×10^{-2}
R_G	[J/mol·K]	8.315
p_{vapor}	[Pa]	3169
m_{O2}	[kg/mol]	0.032
m_{N2}	[kg/mol]	0.028
m_{H2O}	[kg/mol]	0.018
D_{O2}	[m^2/s]	2.67×10^{-9}
y_{O2}	[–]	1.0
t	[s]	2.0
d_{B0}	[m]	1.0×10^{-5}
DO	[kg/m^3]	1.47×10^{-2}

(a) Influence of the time step

In order to set an appropriate value for the time step width Δt, the effect of Δt on the time variation of the bubble diameter was investigated. Fig. 3.2 shows the time variation of bubble

diameter. Fig. 3.2 shows that for time increments $\Delta t \leq 1.0 \times 10^{-7}$ s there is substantially no effect of Δt on the bubble diameter. Note that for $\Delta t > 1.0 \times 10^{-7}$ s, the computation became unstable. The time step was set to $\Delta t = 1.0 \times 10^{-7}$ s in the following simulations to reduce the computational time, since Δt have almost no effect on the computation results in this calculation range.

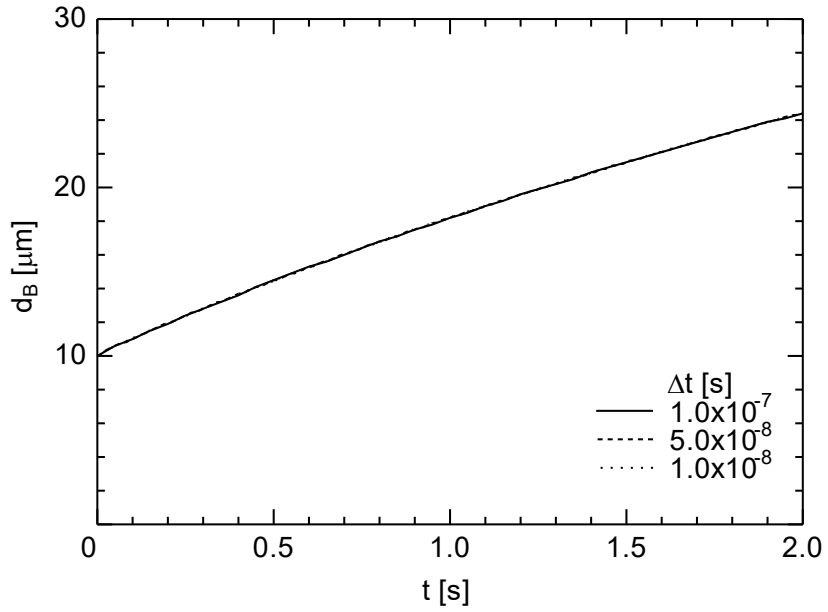

Fig. 3.2 Effects of Δt on bubble diameter change.

(b) Influence of the grid spacing

When calculating the concentration distribution of each gas component in the liquid phase around a bubble, it is necessary to discretize the space in the radial direction. The influence of Δr on the time variation of the bubble diameter was investigated as shown in Fig. 3.3. Slight differences in the time variation of the bubble diameters were caused by Δr. Therefore, the relationship between the errors $\varepsilon_{\Delta r}$ and Δr was investigated. The results are shown in Fig. 3.4 and Table 3.2. Here, $\varepsilon_{\Delta r}$ was defined for bubble diameter d at $t = 2$ s, based on the calculation result for the smallest grid spacing ($\Delta r = 6.0 \times 10^{-8}$):

$$\varepsilon_{\Delta r} = \frac{d^{t=2s} - d^{t=2s}_{\Delta r=6.0\times10^{-8}}}{d^{t=2s}_{\Delta r=6.0\times10^{-8}}} \tag{3.9}$$

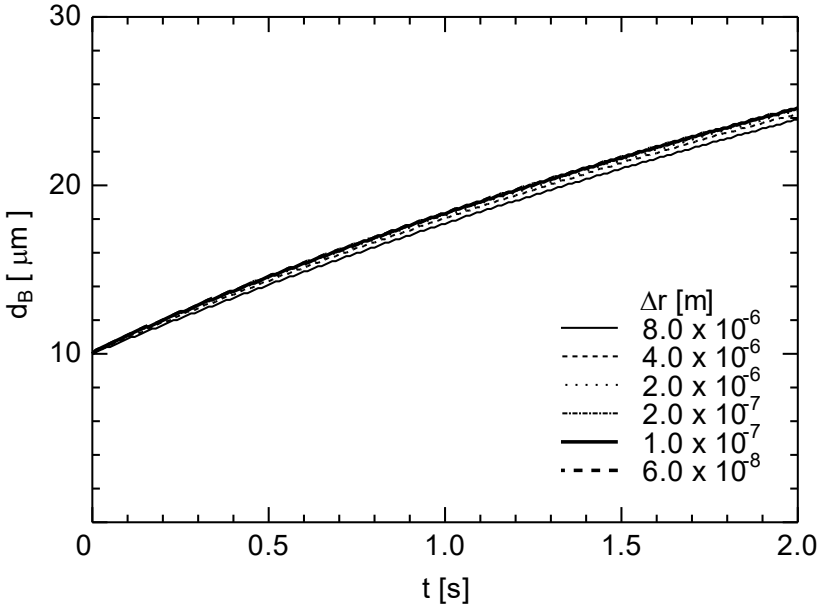

Fig. 3.3 Effects of Δr on bubble diameter change.

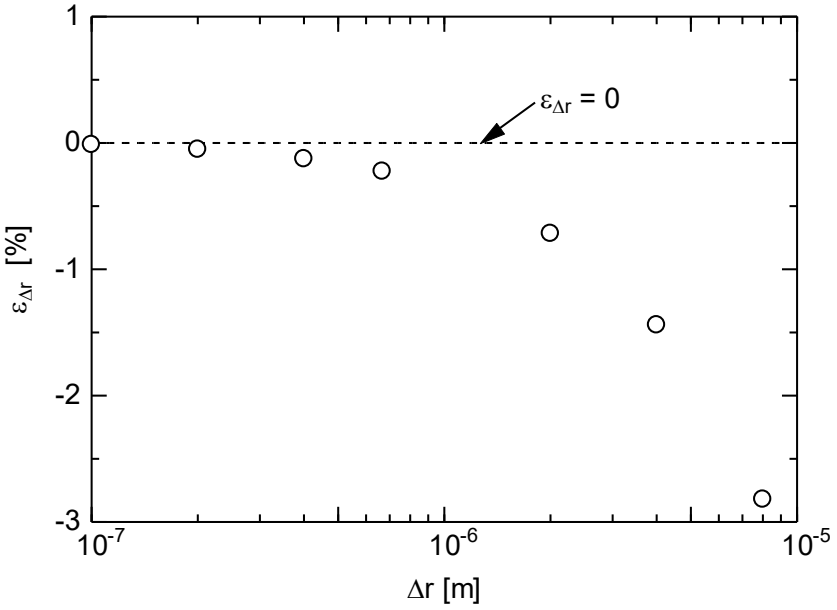

Fig. 3.4 Relation between Δr and $\varepsilon_{\Delta r}$.

Table 3.2 Effects of Δr and $\varepsilon_{\Delta r}$.

Δr [-]	$\varepsilon_{\Delta r}$ [%]
8.0×10^{-6}	−2.82
4.0×10^{-6}	−1.44
2.0×10^{-6}	−0.72
2.0×10^{-7}	−0.12
1.0×10^{-7}	−0.05
6.0×10^{-8}	—

As Δr increases, the mass transfer rate decreases due to the weakening of the concentration boundary layer, and the bubble diameter tends to be underestimated. The error decreases as Δr decreases, and converges to almost zero for $\Delta r > 2.0 \times 10^{-7}$. The larger the value of Δr, the more accurate the calculation is, but the calculation becomes more time-consuming. In this study, the value of $\Delta r = 2.0 \times 10^{-7}$ was chosen, which yields an error of less than 0.15% for $\Delta r = 6.0 \times 10^{-8}$.

(c) Influence of computational domain

The influence of the computational domain on the bubble diameter in the calculation of the concentration distribution in the liquid phase was investigated. The effect of the ratio of the computational domain size A to d_B, $\widetilde{A} = A / d_B$, on the time variation of d_B is shown in Fig. 3.5. The error, $\varepsilon_{\widetilde{A}}$, of d_B at each $\widetilde{A}$ is shown in Fig. 3.6. $\varepsilon_{\widetilde{A}}$ was defined for the bubble diameter d at $t = 2.0$ s, based on the bubble diameter d at $\widetilde{A} = 100$, i.e.,

$$\varepsilon_{\widetilde{A}} = \frac{d^{t=2s} - d^{t=2s}_{\widetilde{A}=100}}{d^{t=2s}_{\widetilde{A}=100}} \tag{3.10}$$

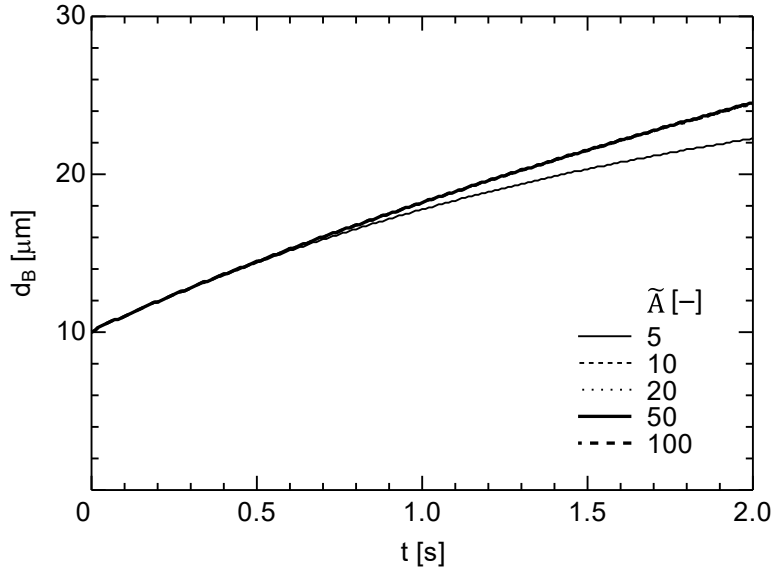

Fig. 3.5 Effects of $\widetilde{A}$ on bubble diameter change.

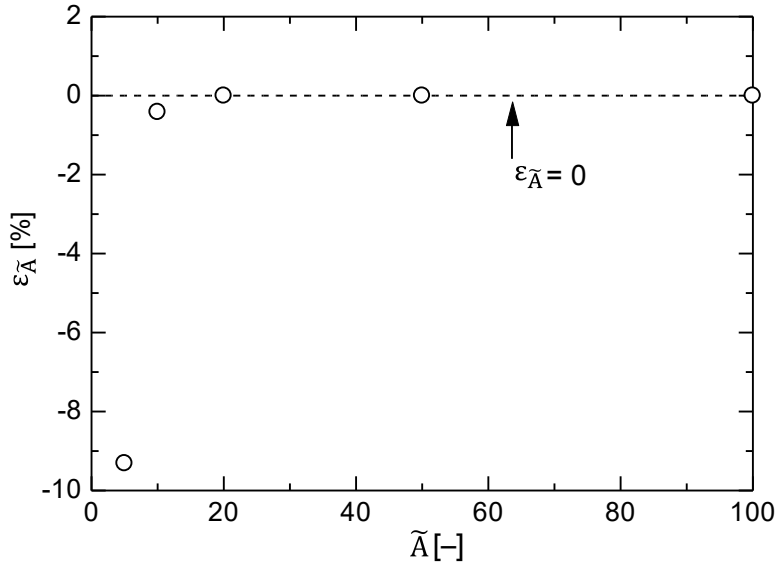

Fig. 3.6 Relation between $\widetilde{A}$ and $\varepsilon_{\tilde{A}}$.

The time variation of d_B was influenced by $\widetilde{A}$, but the dependence on $\varepsilon_{\tilde{A}}$ converged to almost zero for $\widetilde{A} \geq 10$. The error in bubble diameter at $t = 2$ s is 0.09% for $\widetilde{A} = 20$ compared to $\widetilde{A} = 100$. Therefore, $\widetilde{A} = 20$ was chosen in this study because it has an error of less than 0.1% with respect to $\widetilde{A} = 100$.

3.3 Results of single bubble simulations

3.3.1 Validation for growing bubble

The experiments on a water flow containing microbubbles to investigate a cleaning process of viscous oil adhering to the channel wall were described in Chapter 2. The results showed that microbubbles attached to the oil interface and became larger in time. An experiment on a single bubble attaching to the oil interface in a stagnant water was also conducted and the cause of the bubble growth is the mass transfer from oxygen-rich water to the bubble. Fig. 3.7 shows the temporal change in the bubble diameter measured in the literature (the circles). The initial bubble diameter is 25 μm and the bubble grows monotonically and enters the sub-milli range at $t \sim 40$ s, the diameter reaches 260 μm at $t = 240$ s, i.e., it is no longer a microbubble. It should be noted that the bubble shape was not perfectly spherical because of the formation of the three-phase contact line between the bubble, the liquid and the oil. See Chapter 2 for more details.

The single growing bubble was simulated using the present numerical method. The initial bubble diameter was 25 μm and the initial concentration of DO was 9.65×10^{-3} kg/m^3 as in the experiment. The oxygen, nitrogen and water vapor were considered. The other numerical conditions are shown in Table 3.3. The initial conditions of p_B and N were set by using the following Young–Laplace equation (Eq. (3.11)) and the equation of state (Eq. (3.2)), respectively:

$$p_{B0} = p_L + \frac{2\sigma}{R_0} \tag{3.11}$$

The prediction is shown in Fig. 3.7 by the solid line. The bubble growth is well reproduced by the present method. The slight deviation for $t > 90$ s can be attributed to the fact that the bubble shape was not perfect spheroid in reality.

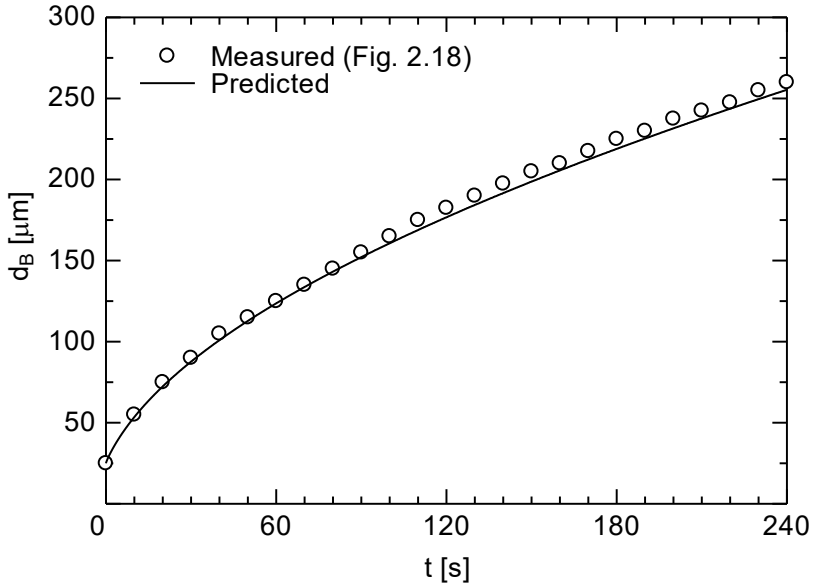

Fig. 3.7 Microbubble growth (single bubble).

Table 3.3 Numerical conditions for single bubble simulation.

T	[K]	298
ρ_L	[kg/m^3]	997
μ	[Pa·s]	8.94×10^{-4}
p_0	[Pa]	1.013×10^5
σ	[N/m]	7.13×10^{-2}
R_G	[J/mol·K]	8.315
p_{vapor}	[Pa]	3169
m_{O2}	[kg/mol]	0.032
m_{N2}	[kg/mol]	0.028
m_{H2O}	[kg/mol]	0.018
D_{O2}	[m^2/s]	2.67×10^{-9}
D_{N2}	[m^2/s]	2.0×10^{-9}
H_{O2}	[Pa]	4.42×10^9
H_{N2}	[Pa]	8.57×10^9
Δt	[s]	1.0×10^{-7}
Δr	[m]	2.12×10^{-7}

3.3.2 Validation for shrinking bubble

Ward et al. [11] carried out an experiment on dissolution of a single bubble in stagnant liquid. Fig. 3.8 shows the temporal change in measured d_B (the circles). The initial diameter is 212 μm, i.e., it is not a microbubble. However, the bubble shrinks monotonically and d_B is less than 100 μm for $t > 590$ s. Ward et al. [11] also predicted the time evolution of d_B using the statistical rate theory and obtained a good agreement between the data and the prediction (the dotted line) as shown in Fig. 3.8.

The time evolution of d_B of the shrinking bubble was predicted by using the present numerical method as shown by the solid line in Fig. 3.8. d_{B0}, T and p_0 were set to 212 μm, 298 K, and 2.5×10^4 Pa, respectively as reported in the experiment. The other conditions were set as given in Table 3.1. The bubble diameter predicted by the present method agrees well with the measurement and the prediction by Ward et al. [11] though some deviation between them is observed for $t > 600$ s. The fluid properties and transport coefficients such as the diffusion coefficients used in the literature were not provided there, and the values given in Table 3.1 were used in the present simulation. There could therefore be slight differences in those values. Since the rate of change in the bubble diameter is not fast at the early stage of the diameter change, the possible differences in the calculation conditions does not affect the result. The decreasing rate however becomes large for $t > 600$ s, and the present prediction shows some deviation from the result of Ward et al. for the steep change in the bubble diameter.

The good agreements in Secs. 3.3.1 and 3.3.2 show that the present method is capable of accurately predicting the mass transfer between a single bubble and liquid.

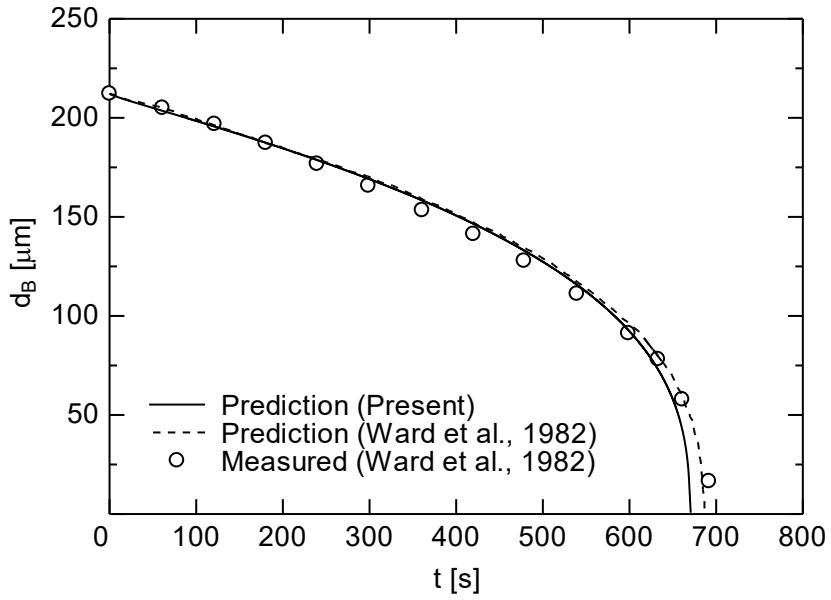

Fig. 3.8 Comparison between experiment data of a single shrinking bubble (Ward et al., 1982) and numerical prediction.

3.3.3 Effects of dissolved oxygen concentration on d_{Beq}

Numerical simulations of single bubbles were carried out at various initial bubble diameter and *DO* to investigate the effects of these parameters on d_{Beq}. The temperature was set at T = 298 K. Figs. 3.9 and 3.10 show the changes in d_B in time at a low and a high *DO*, respectively. Fig. 3.9 shows that under the low dissolved oxygen condition ($DO = 8.8 \times 10^{-3}$ kg/m^3), bubbles of $d_{B0} \geq 35$ μm grow, while those of $d_{B0} \leq 30$ μm shrink. The d_{Beq} is therefore in between 30 and 35 μm, and a slight difference in the initial size can drastically change d_B after experiencing mass transfer. Under the high dissolved oxygen concentration condition ($DO = 1.47 \times 10^{-2}$ kg/m^3), bubbles of $d_{B0} \geq 4$ μm grow, while those of $d_{B0} \leq 3$ μm shrink, i.e., d_{Beq} is much smaller than in the low *DO* case.

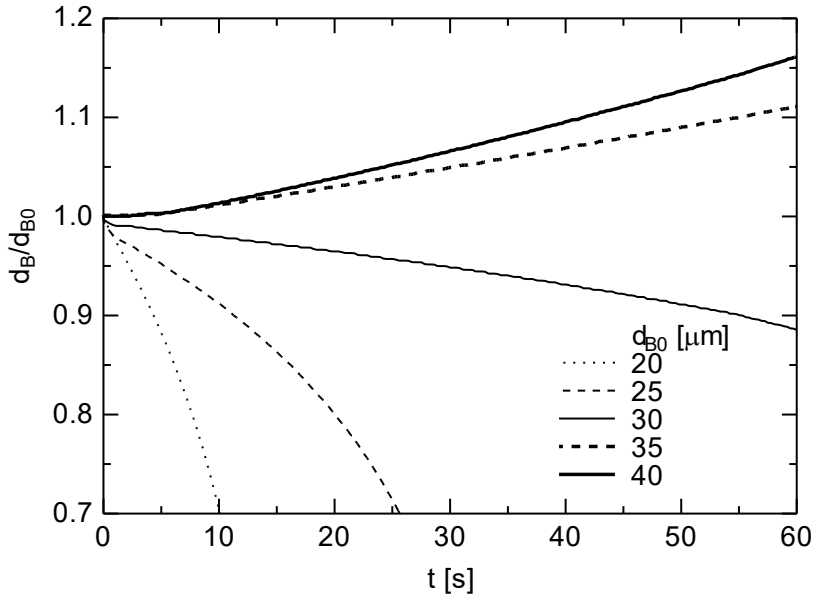

Fig. 3.9 Change in d_B at low DO (8.8×10^{-3} kg/m^3).

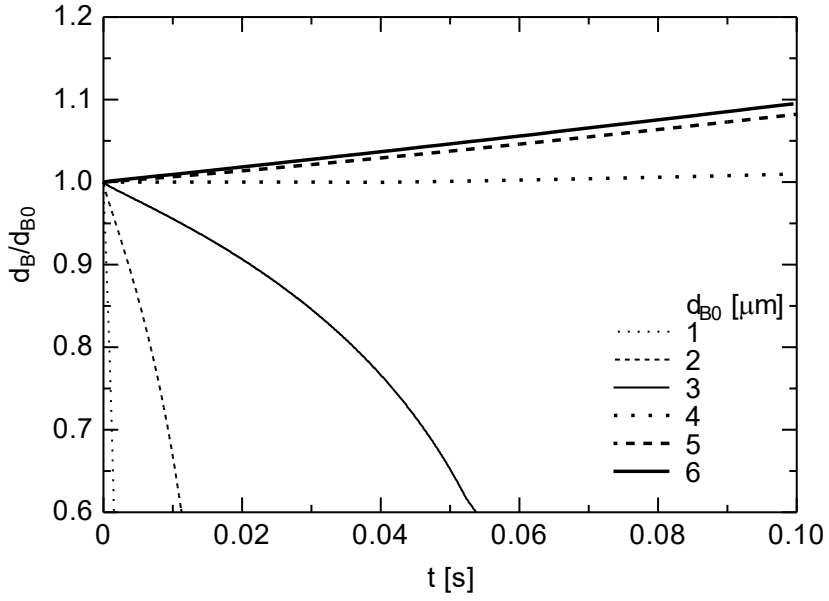

Fig. 3.10 Change in d_B at high DO (1.47×10^{-2} kg/m^3).

The d_{Beq} was calculated as a function of DO by Eq. (1.8) as shown in Fig. 3.11, where only oxygen was considered. The d_{Beq} steeply decreases as DO increases at the small DO range. For $DO < 8.6 \times 10^{-3}$ kg/m^3, all microbubbles (1–100 μm) shrink, while they grow for $DO > 3.2 \times 10^{-2}$ kg/m^3.

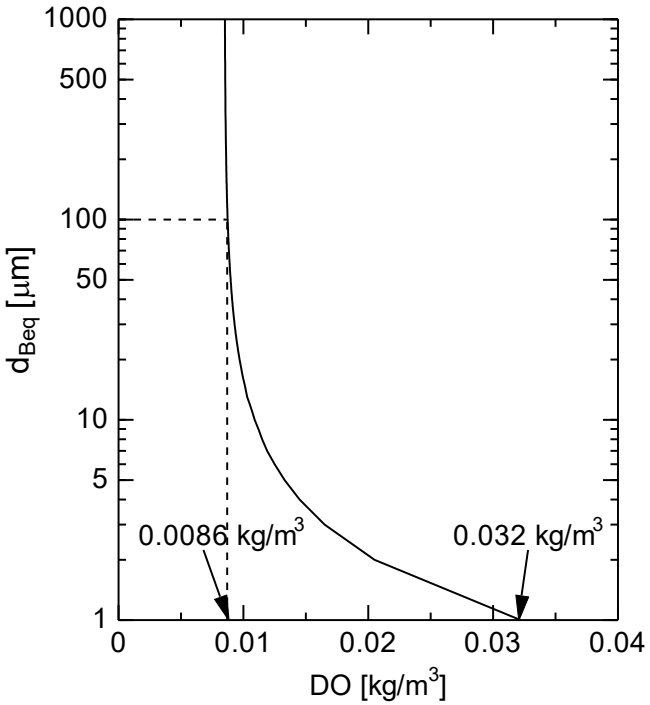

Fig. 3.11 Relation between d_{Beq} and DO.

3.4 Results of Validation for microbubble flow

3.4.1 Experimental

3.4.1.1 Experimental apparatus and methods

Experiments on microbubbles in a water stream generated by a pressurized dissolution method were conducted to investigate changes in the bubble size distribution of bubble groups and to obtain data for validation of the numerical method. Fig. 3.12 shows a schematic of the experimental apparatus which consisted of the compressor, the pump, the dissolution tank, the decompression nozzle for inducing cavitation, and the test section. Water purified by a Millipore system (Elix UV3) was used for the liquid phase. Water and air were supplied to the dissolution tank by the pump (Iwaya Electric, 25AJT0751B) and the compressor (Hitachi, SRL-2.2DA6), respectively. The air was dissolved in water in the dissolution tank at the gauge pressure of 0.1 MPa. The dissolution tank consisted of the outer and inner cylinders. The air and water supplied to the dissolution tank formed an upward bubbly flow in the inner pipe, and then water fell from the top end of the inner cylinder to form a film flow on the outer surface of the cylinder. Air dissolved into water through the air-water interfaces of the falling film and bubbles. The excess gas in the dissolution tank was exhausted through the exhaust valve. The *DO* at the upstream region of the nozzle was controlled by changing the water level in the dissolution tank, in other words the gas-liquid contact time. The *DO* in the upstream region of the decompression nozzle was measured by a *DO* meter (HACH, LDO101-01 HQ30d). The water with microbubbles flowed into the upper tank through the test section. The acceleration of the flow at the decompression nozzle (Fig. 3.13 (b)), whose dimensions were 4, 32 and 54 mm in the width, depth and length, respectively, while in the middle part of 4 mm length had 1 mm width, reduced the pressure when water flowed through the nozzle, and cavitation occurred there. The cavitation bubbles consisted of not only vapor molecules but also non-condensable gas molecules, which had dissolved in water in the dissolution tank. Pressure recovery at the downstream of the nozzle induced condensation of the vapor molecules, and remained non-condensable gas molecules

formed microbubbles. See Maeda et al. [5] for more details of the experimental apparatus and the bubble generation mechanism.

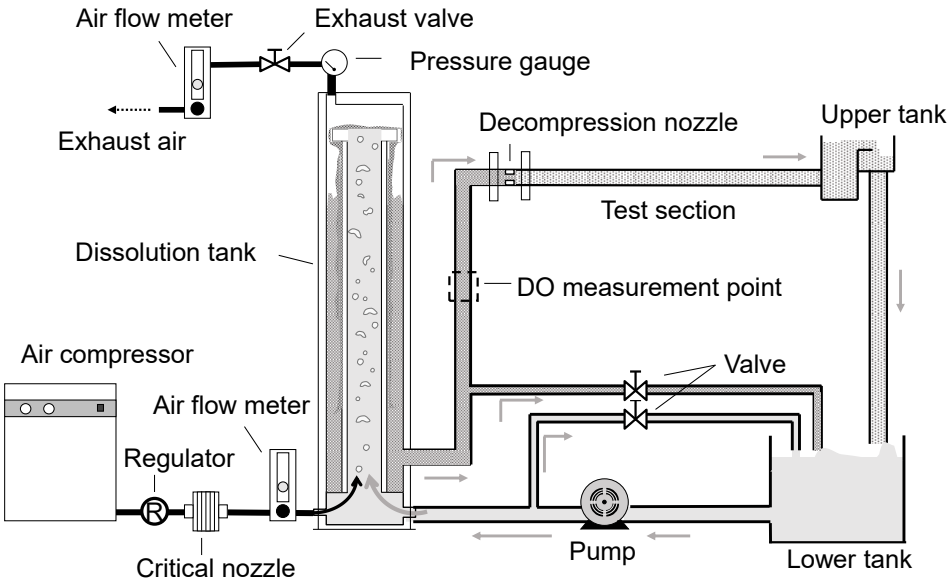

Fig. 3.12 Apparatus for microbubble flow experiment.

Fig. 3.13 (a) shows the test section, which was the square duct, the dimensions of which were 32, 32 and 1070 mm in the width, depth and length, respectively. The d_B and DO were, respectively, measured by using the phase Doppler anemometry (PDA, DANTEC, 60X) and the DO meter at L = 400, 550, 700 and 900 mm, where L is the distance from the exit of the decompression nozzle. The flow was confirmed to be developed for L < 400 mm. The scattering angle of the PDA optics, i.e., the angle between the transmitter and the receiver was 90 degrees. The sample number, N_s, of bubbles was 20,000. The n_B was evaluated from the data acquisition rate and the liquid velocity measured by PDA [5–7]. The water temperature and the concentration of dissolved oxygen (DO_{in}) in the upstream region of the decompression nozzle were fixed at 298.0 ± 1.0 K and (1.47 ± 0.01) × 10^{-2} kg/m^3, respectively.

The liquid volumetric flux, J_L, at the nozzle throat ranged from 9.0 to 13.5 m/s. Fig. 3.13 (c) shows the flow patterns in the decompression nozzle. No cavitation (NC) occurred at low J_L (= 9.0–10.0 m/s). At medium J_L (= 10.5–11.5 m/s), bubble cavitation (BC) occurred at the

entrance of the decompression nozzle. Cavitation developed as J_L increased, and it transited to sheet cavitation (SC) which covered whole decompression nozzle at J_L = 12.0 m/s.

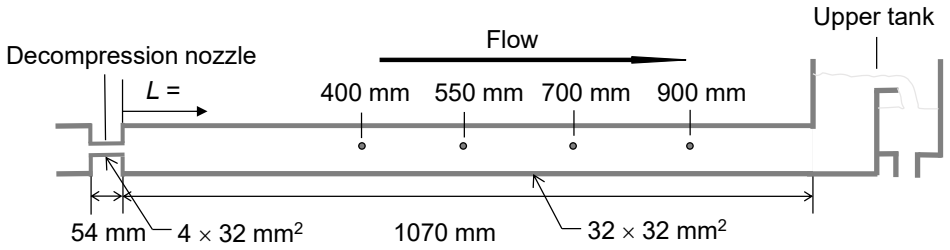

(a) Test section and measurement points.

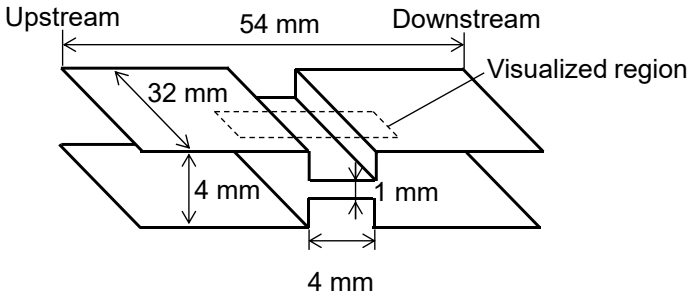

(b) Decompression nozzle.

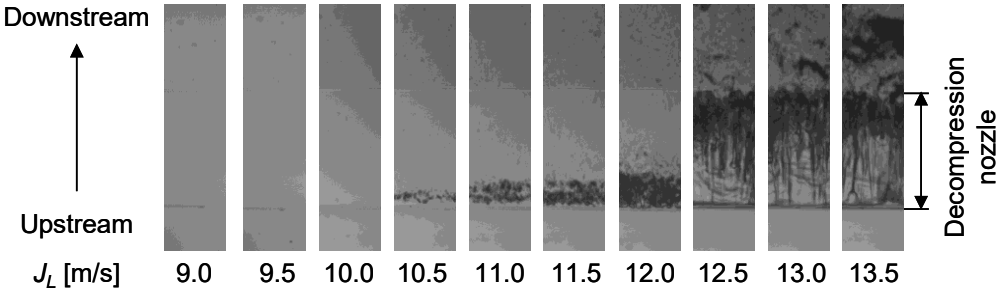

(c) Flow pattern in the decompression nozzle.

Fig. 3.13 Test section (a), decompression nozzle (b) and flow pattern in the decompression nozzle (c).

3.4.1.2 Results of microbubble flow

The probability density function, P^j, and the volume fraction, α^j, of the jth bubble size class are shown in Figs. 3.14 and 3.15, respectively, where α^j was calculated by

$$\alpha^j = \frac{\pi d_B^{\,3}}{6} n_B P^j \tag{3.12}$$

When the cavitation does not occur in the decompression nozzle (NC, J_L = 9.0–9.5 m/s), d_B is mainly in the range of 0–60 μm and α^j takes low values due to the low n_B. The bubble size distribution shifts to the larger diameter side with increasing L. When BC occurs in the nozzle (J_L = 10.5–11.5 m/s), the bubble size distribution at L = 400 mm is sharper than that in the NC case and α^j at L = 400 mm increases with J_L. The bubble size distribution shifts to the larger diameter side as L increases and α^j increases mainly for d_B = 20–50 μm. These increases in d_B and α^j are due to the mass transfer between bubbles and water. When SC occurs in the nozzle (J_L = 12.5–13. 5 m/s), the distributions of P^j and α^j at L = 400 mm are broader compared with those in the BC case. The bubble size distribution shifts to the larger diameter side with increasing L. The α^j increases especially for d_B = 20–50 μm and the increase at larger d_B (> 60 μm) is not significant. This is attributed to that the mass transfer rate of small bubbles is larger than that of large bubbles due to the large interfacial area concentration per unit gas volume. Experimental data of the total volume fraction and the time evolution of the difference are described in the following section.

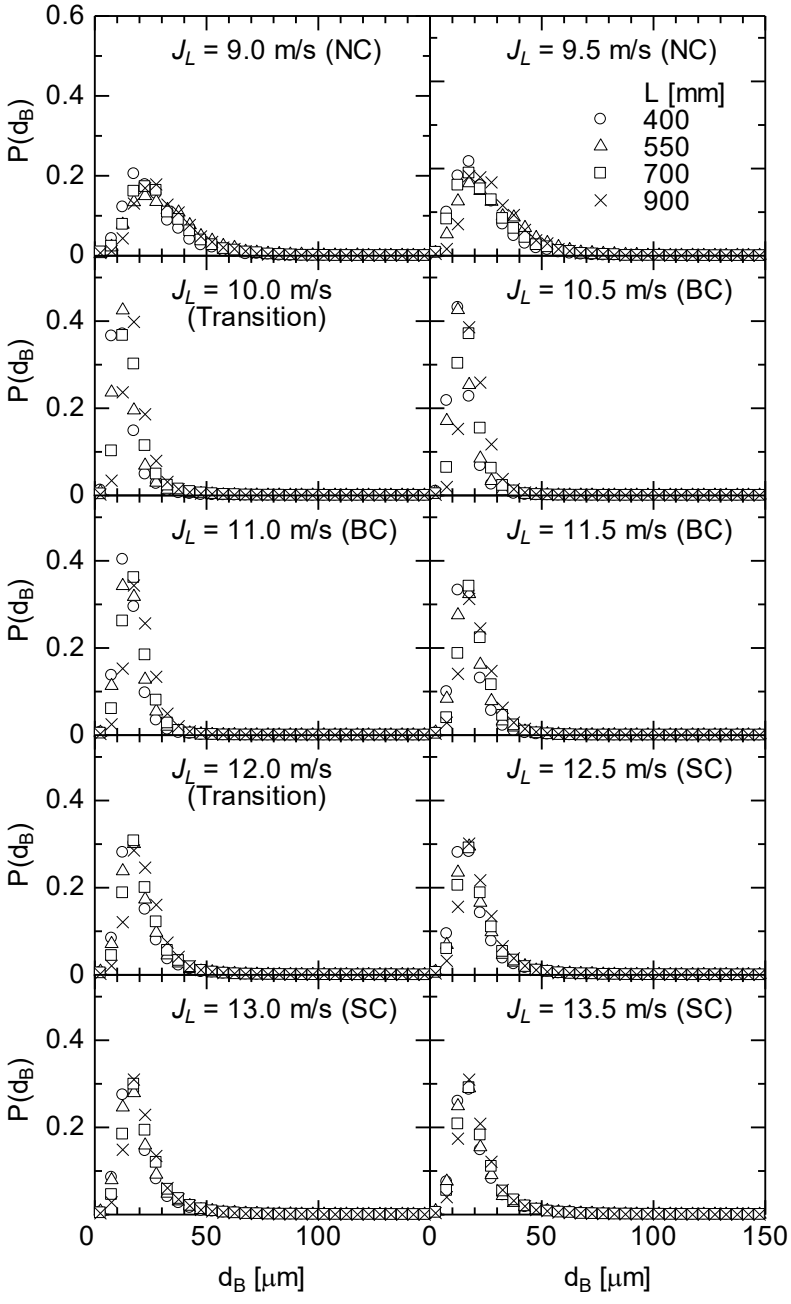

Fig. 3.14 Bubble size distribution.

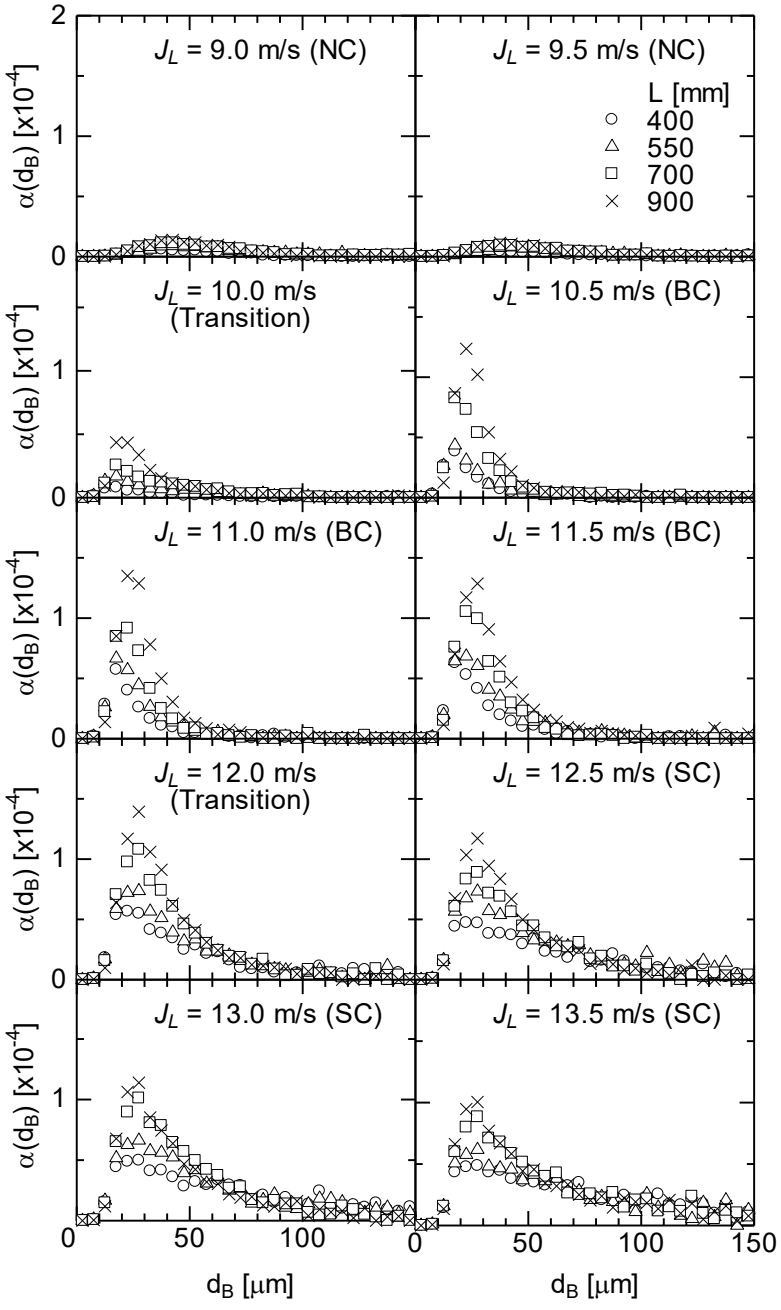

Fig. 3.15 Gas volume fraction.

3.4.2 Comparison between numerical predictions and measured data

Numerical predictions of $P(d_B)$ are compared with the data in Figs. 3.16–3.18. The predicted $P(d_B)$ are in agreement with the data for all the conditions and L. Numerical predictions of $\alpha(d_B)$ are compared with the data in Figs. 3.19–3.21. The predicted α show the same trends as the experimental results, that is, (1) the change in α is small for J_L = 9.0–9.5 m/s, (2) α increases with L mainly for d_B = 20–50 μm, and (3) the increase in α with L is small for d_B > 60 μm. Hence, the numerical simulation can predict well the diameter change due to the mass transfer between bubbles and water.

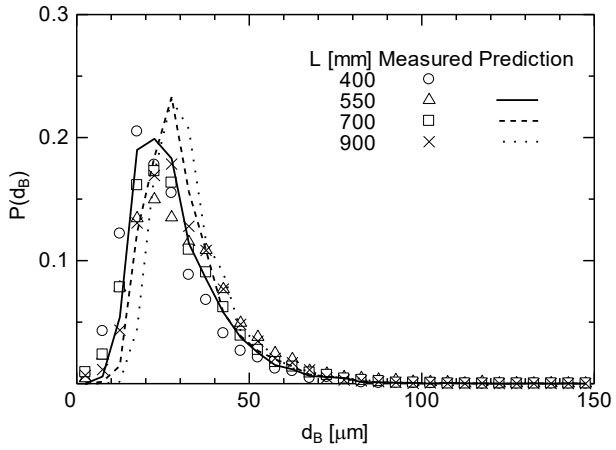

Fig. 3.16 Measured and predicted bubble size distribution of J_L = 9.0 m/s (NC).

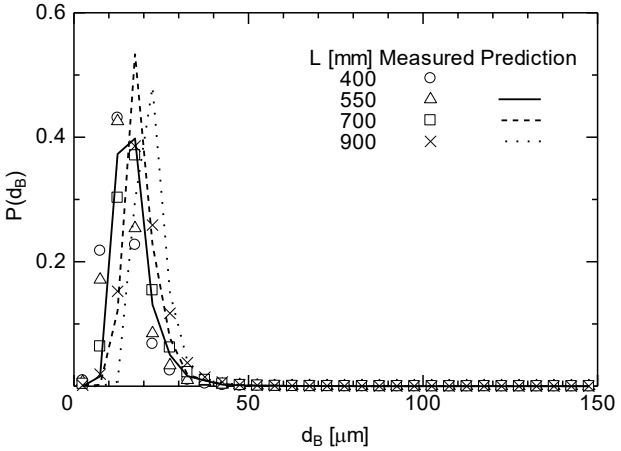

Fig. 3.17 Measured and predicted bubble size distribution of J_L = 10.5 m/s (BC).

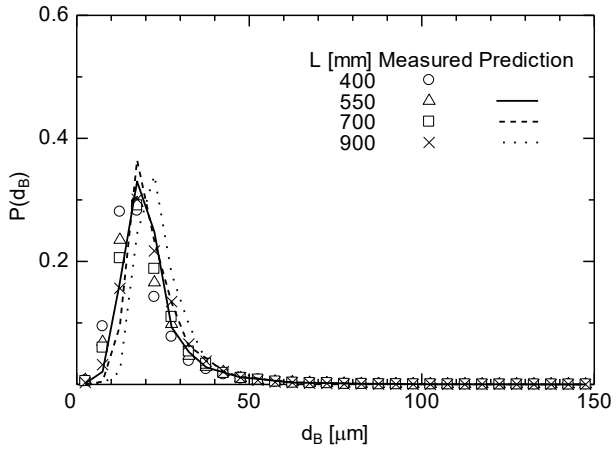

Fig. 3.18 Measured and predicted bubble size distribution of J_L = 12.5 m/s (SC).

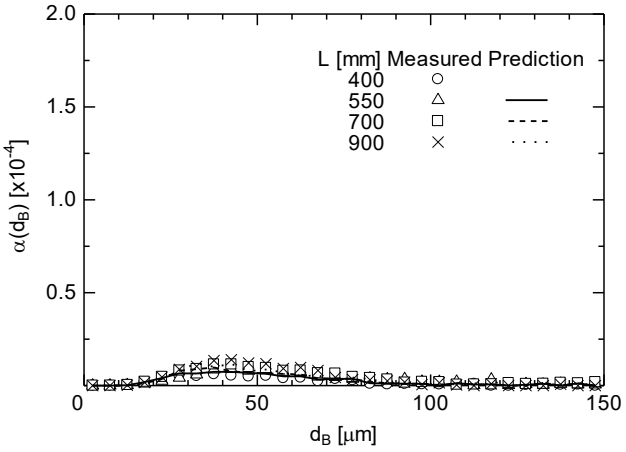

Fig. 3.19 Measured and predicted volume fractions of J_L = 9.0 m/s (NC).

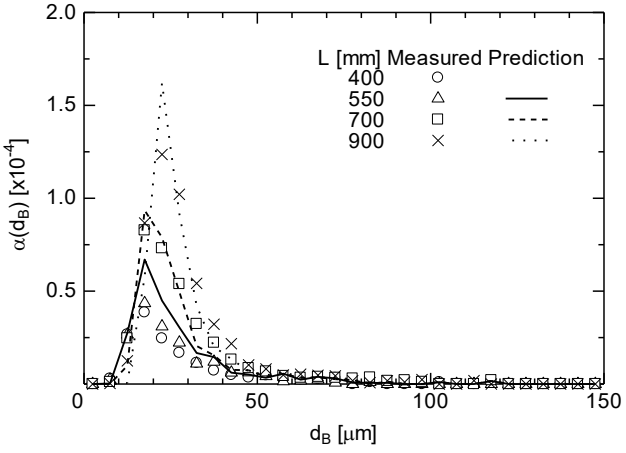

Fig. 3.20 Measured and predicted volume fractions of J_L = 10.5 m/s (BC).

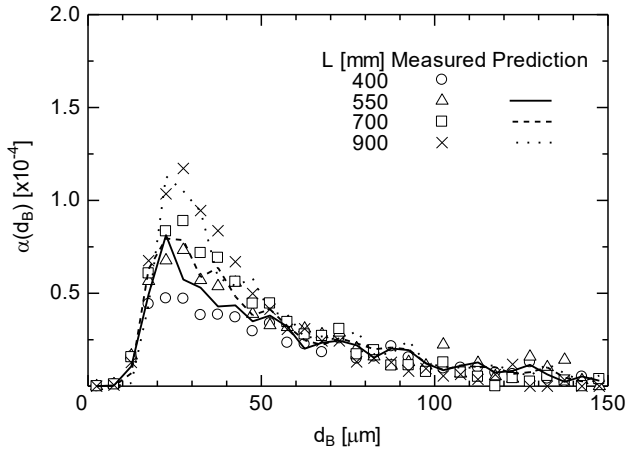

Fig. 3.21 Measured and predicted volume fractions of J_L = 12.5 m/s (SC).

Fig. 3.22 shows the total volume fraction, α, of bubbles, which is calculated by

$$\alpha = \frac{n_B}{N_s} \sum_{j=1}^{N_s} \frac{\pi d_B^{j\,3}}{6} \tag{3.13}$$

The horizontal axis is the time, T_E, elapsed after passing the exit of the decompression nozzle, which is calculated by $T_E = L / U$, where U is the mean liquid velocity in the measurement section. The curves in the figure represent the predicted α. The α increases with T_E when BC or SC occurs in the nozzle ($J_L \geq$ 10.5 m/s). On the other hand, the change in α is small for the NC cases (J_L = 9.0–9.5 m/s). Thus, the mass transfer rate between bubbles and water in the cavitation cases (BC and SC) is larger than that in the NC cases due to higher bubble number densities, i.e., larger interfacial area concentrations. The predictions agree well with the experimental data. Hence, the numerical method can reasonably predict the mass transfer rate between bubbles and water.

Fig. 3.23 shows the time evolution of the difference, ΔDO, between DO (DO_{in}) in the upstream region of the nozzle (DO before bubble generation) and DO at each measurement point ($\Delta DO = DO_{in} - DO$). The ΔDO increases in time for $J_L \geq$ 10.5 m/s, whereas it does not change so much for J_L = 9.0–9.5 m/s. The increases in ΔDO correspond to the increase in α shown in Fig. 3.22. The dissolved gas in water was transferred to bubbles through the

interface. Hence, the concentration of the dissolved gas decreases and the bubble diameter increased with time. The curves in Fig. 3.23 show the predictions, which agree well with the data. Since the numerical simulation assumes that no bubble nucleation occurs in the downstream region of the nozzle, this agreement supports the validity of the assumption. Thus, the decrease in *DO* in the downstream region of the nozzle was mainly caused by the mass transfer of the dissolved gas into the existing bubbles, and the decrease of the dissolved gas concentration due to bubble nucleation was negligibly small because of the small number of bubble nucleation. These results also show that the proposed numerical method can reasonably predict time evolution of bubble size distributions, volume fractions and concentrations of dissolved gas, provided that the reliable initial condition is available.

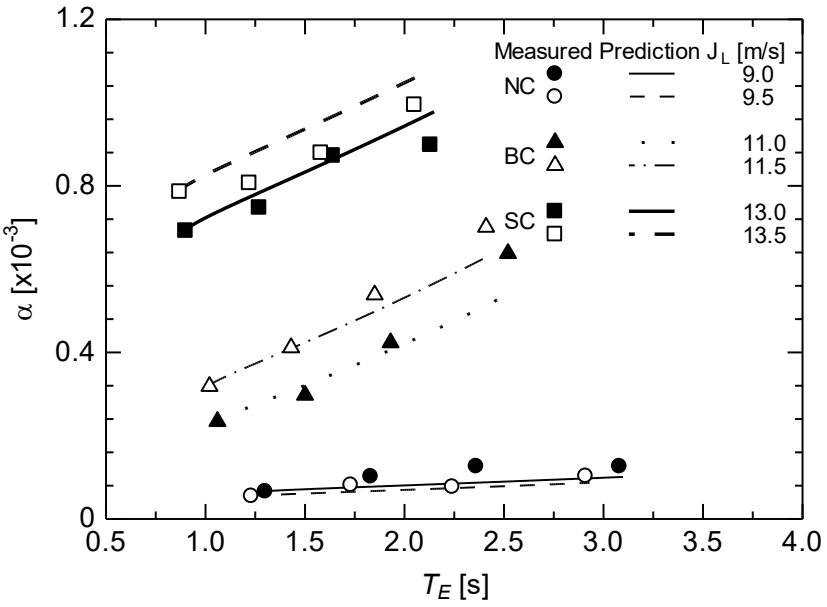

Fig. 3.22 Time evolution of volume fraction of bubbles.

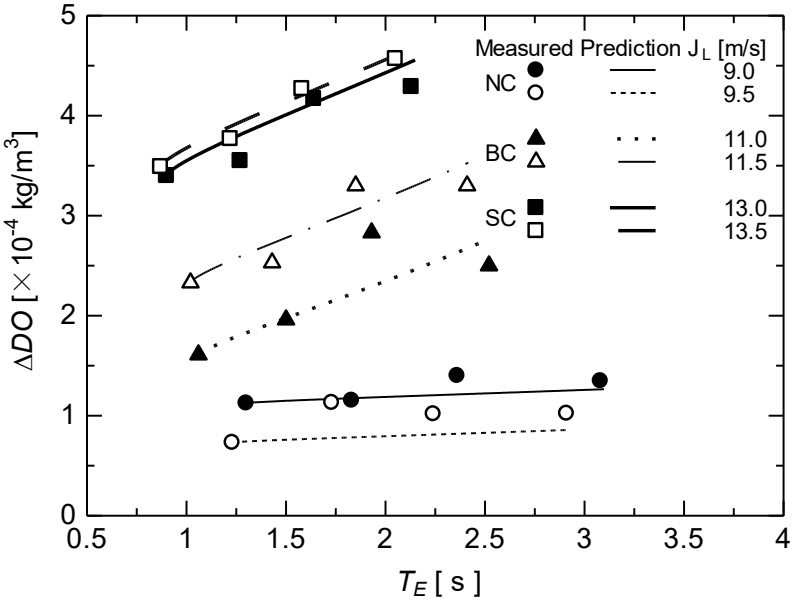

Fig. 3.23 Time evolution of ΔDO.

3.5 Conclusions

Numerical simulations based on the Rayleigh–Plesset equation and the one-dimensional advection-diffusion equation were carried out to investigate the time evolution of bubble diameter and the mass transfer of dissolved gas between bubbles and water after bubble generation for a single microbubble and microbubble groups. As a result, the following conclusions were obtained:

(1) The present numerical method can accurately predict the growth and shrinkage of a single microbubble.

(2) Microbubbles in water flows usually have size distribution and bubbles larger and smaller than the equilibrium bubble diameter become larger and smaller in time, respectively. The size distribution thus changes in time.

(3) The proposed numerical method can reasonably predict time evolutions of bubble size distributions, void fractions and concentrations of dissolved gas, provided that a reliable initial condition is available. Since the numerical simulation assumes that no bubble nucleation occurs in the downstream region of the nozzle, the agreement between the prediction and the experiments proves weak influence of the bubble nucleation on the mass transfer between the phases.

References for Chapter 3

[1] R. Parmar, S. K. Majumder, Microbubble generation and microbubble-aided transport process intensification—A state-of-the-art report, *Chem. Eng. Process*., vol. 64, 79–97, 2013.

[2] K. Tabei, S. Haruyama, S. Yamaguchi, H. Shirai, F. Takakusagi, Study of micro bubble generation by a swirl Jet, *J. Environ. Eng*., vol. 2, 172–182, 2007.

[3] S. Noor, A. Kaneko, The breakup characteristics of bubbles in Venturi tubes under different levels of dissolved gas, *Jpn. J. Multiph. Flow*, vol. 36, 344–352, 2022.

[4] M. Sadatomi, A. Kawahara, H. Matsuura, S. Shikatani, Micro-bubble generation rate and bubble dissolution rate into water by a simple multi-fluid mixer with orifice and porous tube, *Exp. Therm. Fluid Sci*., vol. 41, 23–30, 2012.

[5] Y. Maeda, S. Hosokawa, A. Tomiyama, Y. Baba, Y. Ito, Generation mechanism of micro-bubbles in a pressurized dissolution method, *Exp. Therm. Fluid Sci*., vol. 60, 201–207, 2015.

[6] S. Hosokawa, K. Tanaka, Y. Maeda, A. Tomiyama, S. Yamaguchi, Y. Ito, Effect of entrained air bubbles generated by a pressurized dissolution method, *Trans. Jpn. Soc. Mech. Eng. B*, vol. 76, 53–60, 2010.

[7] C. Taya, Y. Maeda, S. Hosokawa, A. Tomiyama, Y. Ito, N. Shibata, Size distribution of micro-bubbles generated by a pressurized dissolution method, *Jpn. J. Multiph. Flow*, vol. 25, 407–414, 2012.

[8] A. M. Trushin, E. A. Dmitriev, V. V. Akimov, Mechanics of the formation of microbubbles in gas dispersion through the pores of microfiltration membranes, *Theor. Found. Chem. Eng*., vol. 45, 26–32, 2011.

[9] A. S. Tucker, C. A. Ward, Critical state of bubbles in liquid-gas solutions, *J. Appl. Phys*., vol. 46, 4801–4808, 1975.

[10] C. A. Ward, A. S. Tucker, Thermodynamic theory of diffusion-controlled bubble growth or dissolution and experimental examination of the predictions, *J. Appl. Phys*., vol. 46, 233–238, 1975.

[11] C. A. Ward, M. Ritz, A. S. Tucker, Statistical rate theory of interfacial transport. II. Rate of isothermal bubble evolution in a liquid-gas solution, *J. Chem. Phys*., vol. 76, 5606–5614, 1982.

[12] F. Takemura, A. Yabe, Gas dissolution process of spherical rising gas bubbles, *Chem. Eng. Sci.*, vol. 53, 2691–2699, 1998.

[13] S. Kentish, J. Lee, M. Davidson, M. Ashokkumar, The dissolution of a stationary spherical bubble beneath a flat plate, *Chem. Eng. Sci*., vol. 61, 7697–7705, 2006.

[14] H. Takahira, D. Ito, T. Katsuyama, Effects of dynamic surface tension and gas permeation resistance on the stability of microbubbles, *Proceedings of Fluids Engineering Conference 2007*, vol. 37514, 455–463, 2007.

[15] A. Prosperetti, A. Lezzi, Bubbledynamics in a compressible liquid. Part 1. First-order theory, *Fluid Mech*., vol. 168, 457–478, 1986.

[16] H. Liang, M.Z. Liu, Z.W. Yang, Stability analysis of Runge-kutta methods for systems, *Appl. Math. Comput*., vol. 228, 463–476, 2014.

[17] R. H. Perry, D. W. Green, J. O. Maloney, Perry's chemical engineers' handbook 6th edition, *Mcgraw hill book publishing company*, 1984.

[18] D.L. Wise, G. Houghton, The diffusion coefficients of ten slightly soluble gases in water at 10–60°C, *Chem. Eng. Sci*., vol. 21, 999–1010, 1966.

Chapter 4

Generation of microbubbles by subcooled boiling

4.1 Introduction

Various microbubble generation methods have been proposed so far, e.g., the gas-liquid shearing/Venturi tube (bubble breakup) method [1, 2], the ultrasonic wave bubble generator [3, 4], the method based on steam condensation [5, 6] and the pressurized dissolution method [7, 8]. Most of the available methods however require a fluid flow typically with high velocity, a large equipment, resulting in a high operating cost [9–11]. In addition, the experiments in Chapter 2 showed that one of the removal mechanisms is that microbubbles attach to the oil and grow, causing the oil to peel-off, and therefore, it is desired to develop a low-cost and compact microbubble generator which does not require the fluid flow, and that can be applied where cleaning is necessary. Since the bubble generation mechanism of the pressurized dissolution method is not based on effervescent but on shrink of cavitation bubbles [7], subcooled boiling might be one of the candidates of the microbubble generation method.

A microbubble generation method based on subcooled boiling on a heated wire in a liquid with dissolved incondensable gases is proposed in the following. Vapor bubbles are generated due to boiling, and they shrink to form microbubbles of the incondensable gases after the subsequent condensation. Since the proposed method requires neither a pump nor a complex piping system, it is possible to generate bubbles in a stagnant liquid pool. The position, shape and number of heating wires can be changed depending on the application.

The advantage of the proposed method is that generation of microbubbles in arbitrary local positions without liquid supply, so that it can be used in various industrial applications such as water purification systems and chemical processes without water dilution and circulation as well as milli and micro channel applications. Although the proposed method requires a heat input, it can minimize the energy input because it can generate microbubbles at any position required. It, therefore, has a potential to contribute to miniaturization and cost reduction of a microbubble generation apparatus. The diameter and the number density of generated bubbles were measured to demonstrate the performance of the proposed method.

4.2 Experimental apparatus and methods

4.2.1 Experimental setup and experimental conditions

4.2.1.1 Experimental setup and measurement area

Fig. 4.1 shows the experimental apparatus, which mainly consisted of the heating thin metal wire, the power source and the water tank. The wire was platinum (Nilako, PT-351165) of 0.10 mm diameter and 30 mm length and was soldered with lead wires. Table 4.1 shows the properties of the platinum wire used in these experiments. The wire was polished by a sandpaper (#1000) to make small cavities on the surface. The aluminum frame was equipped in the acrylic water tank of 80 × 160 × 120 mm in width, depth and height for fixing the platinum wire. The tank was filled with water purified using a water purification device (Millipore, Elix3). The electrical conductivity of the purified water was 6.7×10^{-6} S/m. The amount of water was 1.0×10^{-3} m^3, so that the level of the free surface was 80 mm. The platinum wire was heated by applying a voltage to it for vapor bubble generation. The power supply system was used as the source of AC power (NF ELECTRONIC INSTRUMENTS, 4210 P-STATION MINI) and DC power (ALINCO, DM130MV). The applied voltage was recorded by the data logger (GRAPHTEC, midi LOGGER GL900). A traverse (SIGMAKOKI, TSD-802S, TSD-803, KSPA-806M) was installed under the acrylic tank for focusing the high-speed camera. A halogen light (OLYMPUS, ILP-1) with a light guide cable (OLYMPUS, KFLG-2) was used as the light source. A telephoto lens (NIKON, Nikkor Ai AF 80–200 mm f/2.8D) and a wide-angle lens (NIKON, Nikkor Ai AF 24 mm f/2.8D) were combined in opposite directions for photography. The images were taken at a magnification of 2.5×, with a resolution of 2.37 μm/pixel.

The bubble generation process was observed using a high-speed camera (Photron, SA-X2). The imaging area (2.00 × 2.00 mm^2) was about the central part of the platinum wire as shown in Fig. 4.2. Since vapor bubbles were detached from the wire and shrunk to the microbubbles before they reached 0.15 mm above the wire, the measurement area of 2.00 × 1.50 mm^2 was set 0.15 mm above the wire. Note that the size of microbubbles was little

change in the vertical direction in the measurement region, and therefore, the microbubbles were in the thermally equilibrium condition.

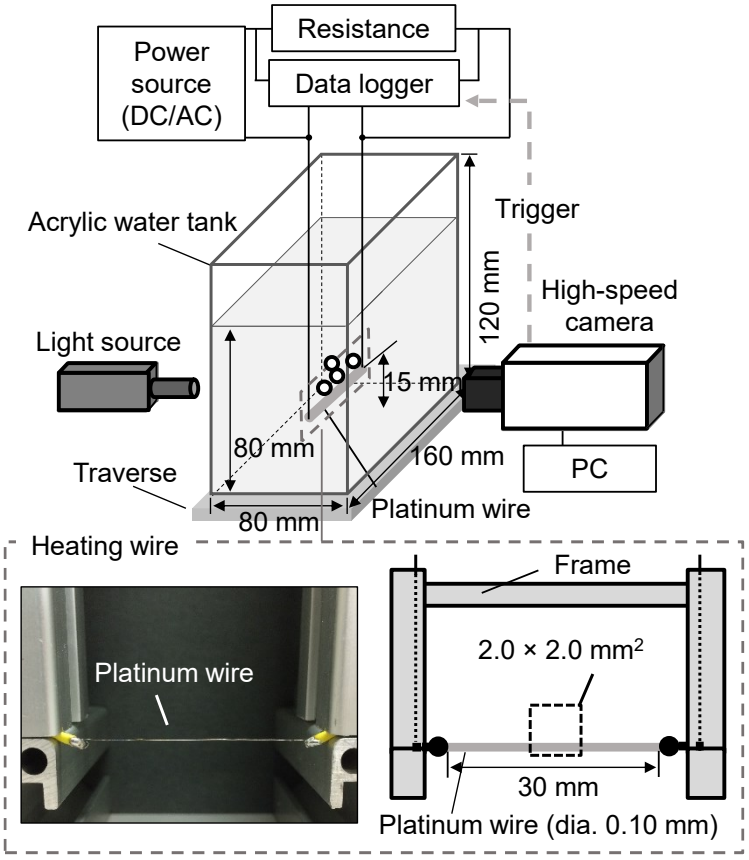

Fig. 4.1 Experimental apparatus.

Table 4.1 Platinum property [12].

Density	ρ_p	[kg/m^3]	2.15×10^4
Melting point	T_m	[K]	2045
Heat conductivity	k_p	[W/m·K]	71.6 [at 300 K]
Electrical resistivity	ρ_e	[Ω·m]	10.6×10^{-8} [at 293 K]

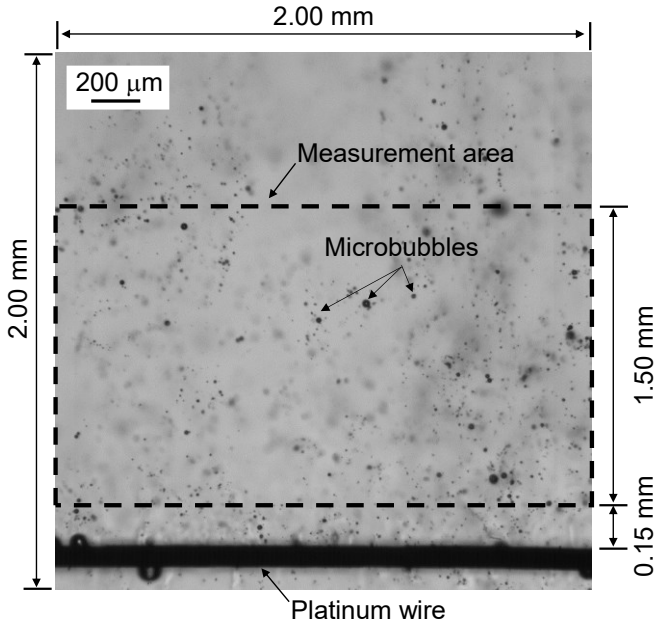

Fig. 4.2 Imaging area and measurement area.

Fig. 4.3 shows a schematic of the experimental setup used to observe the generation process of individual microbubbles in detail. The experimental apparatus consists mainly of an inverted microscope (Nikon, ECLIPSE Ti-U) and a bubble generator (Fig. 4.1). The distance between the bottom of the tank and the position, where the platinum wire was fixed, was kept close so that the platinum wire would be within the DOF. A microscope was used to take photographs, and the magnification of the objective lens (Nikon, S Plan Fluor 20×) was 20. The area of the image was the center of the platinum wire, and the bubble generation state was photographed from the vertical direction down with a high-speed camera (Photron, SA-X2). The area of 0.13×0.30 mm^2 (Fig. 4.4) was set at the center of the platinum wire in the longitudinal direction and included the surface of the platinum wire. The shutter speed was 1/6666 s and the frame rate was 200,000 fps to observe the behavior of individual bubbles. The spatial resolution was 1.00 μm/pixel.

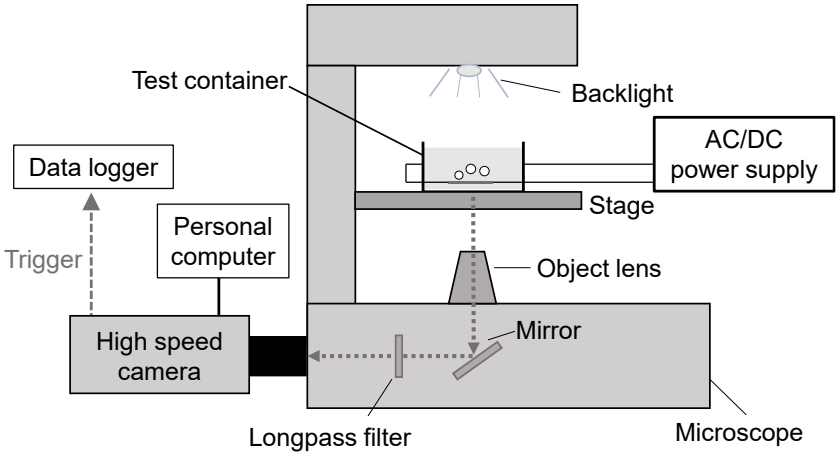

Fig. 4.3 Bubble Observation System.

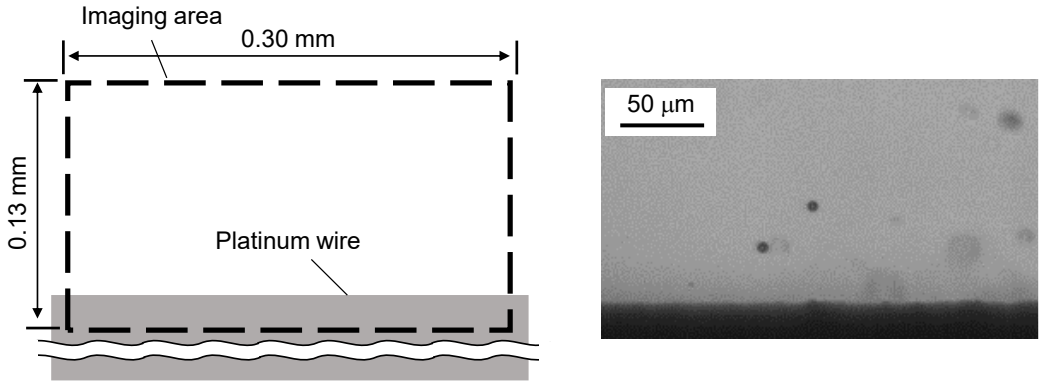

Fig. 4.4 Imaging area.

4.2.1.2 Experimental conditions

All experimental conditions are shown in Table 4.2. The effects of direct current (DC), alternating current (AC), the dissolved oxygen concentration, *DO*, and AC frequency on microbubbles were investigated. The water temperature, *T*, and *DO* in the water tank were measured using a thermometer and a luminescent dissolved oxygen meter (HACH, HQ30d LDO101-01), respectively. The temperature was initially set at $T = 298 \pm 0.5$ K and *DO* of purified water was $(8.5 \pm 0.3) \times 10^{-3}$ kg/m^3. Experiments in reduced *DO* conditions (4.5×10^{-3} and 0.05×10^{-3} kg/m^3) were also conducted to investigate the effects of *DO* on the microbubble generation process. In the condition of $DO = 4.5 \times 10^{-3}$ kg/m^3, the purified

water was degassed by heating, and then the water temperature was reduced to room temperature in an airtight container. In the condition of $DO = 0.05 \times 10^{-3}$ kg/m^3, 0.32 kg/m^3 of sodium sulfite was added to water degassed by boiling to further reduce DO by the reaction:

$$2Na_2SO_3 + O_2 \rightarrow 2Na_2SO_4 \tag{4.1}$$

Note that the incondensable gases other than the oxygen was still dissolved in this condition because only the oxygen was reduced by the chemical reaction. The concentration of Na_2SO_3 is much lower than the concentration in which the effect of Na_2SO_3 on pool boiling heat transfer was reported [13], and therefore, the effect could be negligible in this experiment.

Table 4.2 Experimental conditions.

Type of current	f [Hz]	$\overline{q}$ [MW/m^2]	DO [$\times 10^{-3}$ kg/m^3]
DC	—	1.5 ± 0.1 3.0 ± 0.1 4.5 ± 0.1 6.0 ± 0.1	8.5 ± 0.3
AC	15	4.5 ± 0.1	8.5 ± 0.3
	60	1.5 ± 0.1 3.0 ± 0.1	
		4.5 ± 0.1	0.5 ± 0.2 4.5 ± 0.3 8.5 ± 0.3
		6.0 ± 0.1	8.5 ± 0.3
	240 960	4.5 ± 0.1	

4.2.2 Measurement methods

4.2.2.1 Evaluation method by image analyses

The sphere-volume-equivalent diameter, d_{Bi}, of each bubble and the number density, n_B, in the measurement area were obtained by the image processing as described in Section 2.2.3. The uncertainty of d_B was ±2 μm. The mean bubble diameter, $\overline{d}_B$, was calculated from d_B of over 7,000 bubbles, the uncertainty of $\overline{d}_B$ was 2.4×10^{-2} μm, which is about 0.2% of the typical $\overline{d}_B$. The uncertainty in the average number density, $\overline{n}_B$, was 4.6×10^{6} m^{-3}, which is about 0.05% of the typical value of $\overline{n}_B$.

4.2.2.2 Measurement time

In measuring d_B and n_B, the measurement time was examined. The voltage was applied for 60 s at the power level significantly producing microbubbles. Since the heat flux fluctuates over time in the case of AC, the average heat flux, $\overline{q}$, was defined as the time-averaged heat flux as in the following equation:

$$\overline{q} = \frac{Q}{S_p} = \frac{IV}{\pi d_p l_p} \tag{4.2}$$

where Q is the heating value per unit time, S_p the surface area of platinum wire. The subscript p indicates a platinum wire. Experimental conditions are shown in Table 4.3.

Table 4.3 Experimental condition for measurement time evaluation.

Type of current	$\overline{q}$ [MW/m^2]	T_0 [°C]	DO_0 [× 10^{-3} kg/m^3]	t [s]
AC (f = 60 Hz)	4.5	298	8.50	60

The time variation of $\overline{d}_B$ and $\overline{n}_B$ are shown in Fig. 4.5. $\overline{d}_B$ showed little variation which was found to be within ±5% of the mean of all data. The $\overline{n}_B$ showed large time variability, but were within ±10% of the mean of all data after t = 7.5 s. The changes in T and DO during the bubble generation experiment is shown in Fig. 4.6. Although T slightly increases and DO slightly decreases with time due to heating and bubble generation, the changes in T and DO during the measurement time (30 s) were less than 1 % of the initial values. Note that the time around t = 0.0 s was immediately after the generation of bubbles, so that there were not enough bubbles in the measurement area and the state of bubble generation was not steady. Therefore, the period around t = 0.0 s was excluded from the measurement, and t = 0.50 ~ 30.5 s was set as the measurement time.

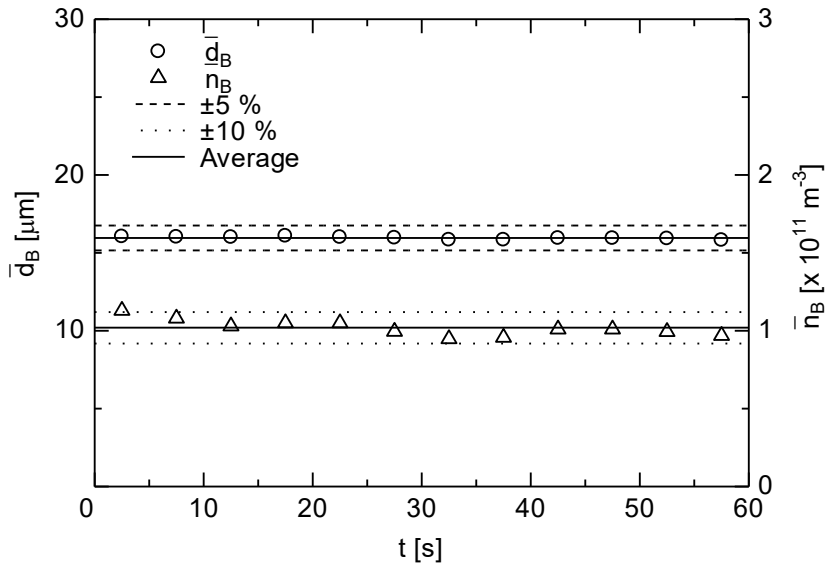

Fig. 4.5 Relation between $\overline{d}_B$, $\overline{n}_B$ and t.

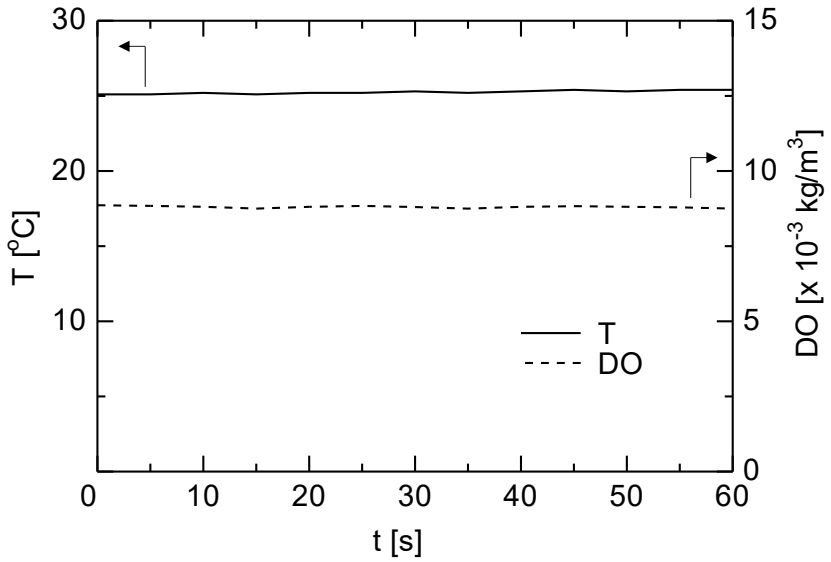

Fig. 4.6 Changes in T and DO.

4.2.2.3 Evaluation method of heat transfer from wire surface

Fig. 4.7 shows a schematic diagram of the circuit used to measure the temperature T_W of the platinum wire. It is known that the mean temperature of the platinum wire is to be proportional to the electric resistance, R_p, and the temperature of the platinum wire was therefore evaluated from the time variation of R_p.

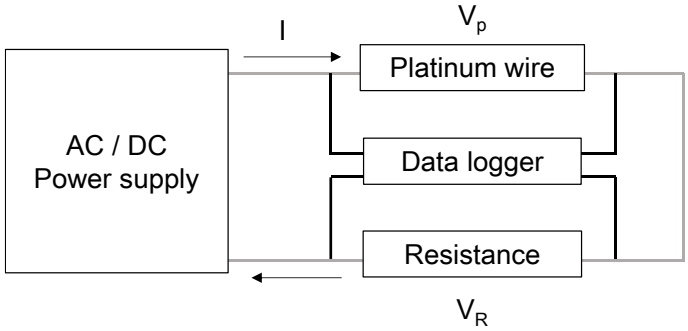

Fig. 4.7 Circuit diagram.

At first, the relation between the temperature of the platinum wire and the heat transfer surface temperature, T_W, of the platinum wire is examined as follows. The magnitude of the difference between the internal temperature and the surface temperature of a cylinder is related to the Biot number, Bi, which is expressed by

$$Bi = \frac{hl_H}{k_p} \tag{4.3}$$

where l_H (= d_P/4) is the hydraulic equivalent length, which divides the volume V_p of the platinum wire by its surface area S_p, and h the heat transfer coefficient. The heat conductivity k_p = 71.6 W/m·K from Table 4.1, and h = 10^3–10^5 W/m^2·K for phase change heat transfer, substituting the maximum h = 10^5 W/m^2·K into equation (4.3), Bi = 0.030. Since Bi << 1.0 for the present condition, the temperature distribution could be almost uniform on the metal surface [14], and the temporal change of the temperature was determined only by the relationship between the heat capacity of the wire and the amount of heat transferred through the surface. Therefore, in this study, T_W of the platinum wire can be represented by the mean temperature.

The process of calculating T_W is as follows. First, the voltage V_R applied to a fixed resistor (electrical resistance R_R = 0.05 Ω, 100 ppm/K) is measured with a data logger. The following equation was obtained from Ohm's law at both ends of the resistor.

$$V_R = I_E R_R \tag{4.4}$$

The I_E was calculated from the above equation by substituting the measured V_R and R_R. Since the input resistance of the data logger was 1.0 MΩ, the current flowing through the data logger could be negligible, and the current flowing through the fixed resistor and the current flowing through the platinum could be considered equivalent. The resistance of the lead wire was measured with an LCR meter (HIOKI, IM3536) and was less than 1.0 mΩ, i.e., less than 0.25% of the resistance of the platinum wire (437.0 mΩ at T_W = 298.3 K), thus the lead wire resistance was ignored.

Similarly, the following equation holds at both ends of the platinum wire.

$$V_p = I_E R_p \tag{4.5}$$

Using I given by Eq. (4.4) and V_p measured by the data logger, R_p was calculated. Then, R_p (R_{p1}, R_{p2}) was measured at two water temperatures (T_{01}, T_{02}) using the LCR meter, and the relationship between R_p and T_W was obtained by linear approximation; the relationship with T_W obtained from R_p at T_{01} = 298.3 K and T_{02} = 322 K is shown in Fig. 4.8. From the obtained data, it can be seen that R_p and T_W have the following relationship.

$$R_p - R_{p1} = \frac{R_{p2} - R_{p1}}{T_{02} - T_{01}}(T_W - T_{01}) \tag{4.6}$$

The resistance ratio of platinum wire obtained in this experiment at T_W = 273 K and T_W = 373 K was 1.388. The difference from that of a platinum resistance thermometer (1.385) [15] was less than 1.0 %. Therefore, the relationship between R_P and T_W obtained in this experiment is reasonable.

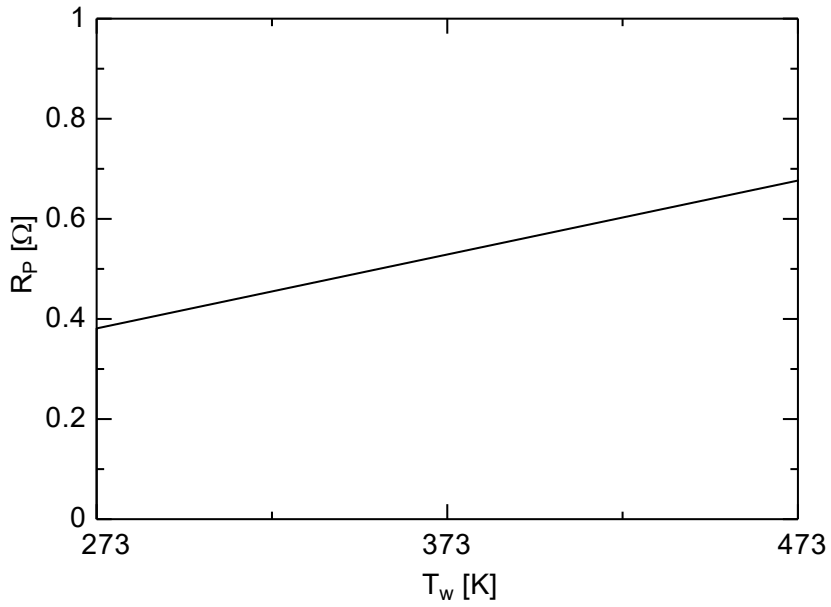

Fig. 4.8 Relation between T_W and R_p.

4.3 Results and discussion

4.3.1 Influence of *DO* and microbubble generation mechanism

4.3.1.1 Influence of dissolved oxygen concentration

The microbubble generation experiments with $DO = 8.5 \times 10^{-3}$, 4.5×10^{-3} and 0.05×10^{-3} kg/m^3, alternating current of the frequency $f = 60$ Hz and the time-averaged heat flux $\bar{q} = 4.5$ MW/m^2 were carried out. Fig. 4.9 shows the generation state of microbubbles at $t = 5.0$ s. The number of microbubbles generated at $DO = 0.05 \times 10^{-3}$ kg/m^3 was small as shown in Fig. 4.9 (a) though vapor bubbles were confirmed to be generated on the platinum wire under this condition as shown in the magnified image, Fig. 4.9 (d). On the other hand, in Fig. 4.9 (b), microbubbles are more visible at $DO = 4.5 \times 10^{-3}$ kg/m^3, and the further increase in *DO* up to 8.5×10^{-3} kg/m^3 (Fig. 4.9 (c)) results in a large increase in the number of microbubbles.

Then, the generation process of individual microbubbles was observed using a microscope to confirm the following three generation patterns, A, B and C. An example of the bubble generations in Pattern A from a certain time t_0 after the steady state was reached is shown in Fig. 4.10 (a). The vapor bubble grows on the wire surface with volume oscillation by repeating expansion and condensation. The bubble elongates vertically and then detaches from the wire. The second is the process in which only the tip of the vapor bubble is broken off and becomes a microbubble when the vapor bubble generated on the platinum wire expands and condenses. Fig. 4.10 (b) shows a bubble generated in Pattern B. The behavior of the bubble attaching to the wire is similar to that in Pattern A, whereas the microbubble is generated by breakup from the parent bubble when the bubble shape becomes unstable due to rapid condensation. Pattern C shown in Fig. 4.10 (c) is very different from the other two; i.e., the vapor bubbles larger than hundred microns collide on the wire, and subsequently they collapse to form multiple microbubbles.

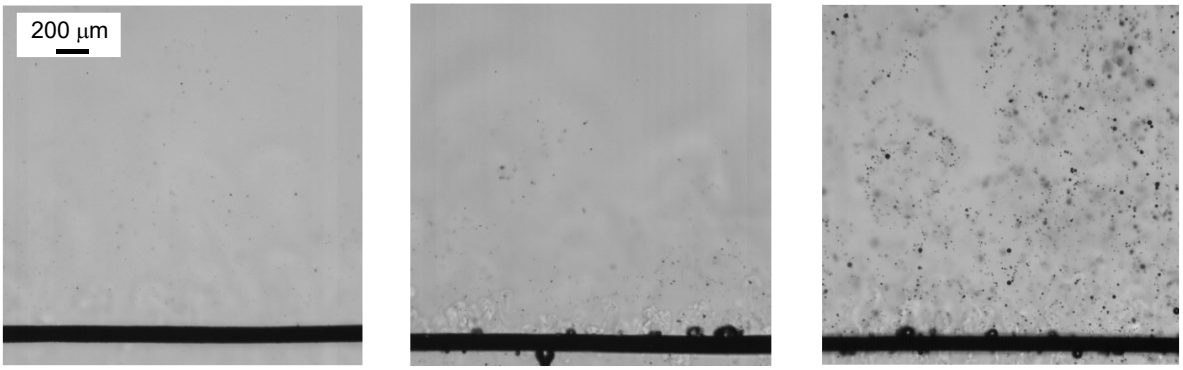

(a) DO [kg/m^3] = 0.05 × 10^{-3} (b) 4.5 × 10^{-3} (c) 8.5 × 10^{-3}

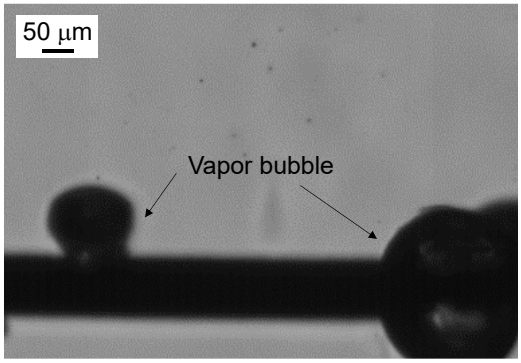

(d) Vapor bubble (DO = 0.05 × 10^{-3} kg/m^3)

Fig. 4.9 Images of generated microbubbles (t = 5.0 s).

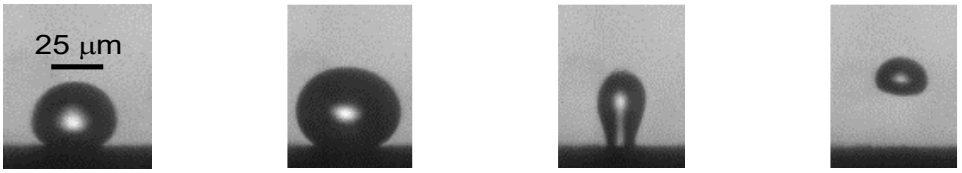

$t = t_0 + 0.0 \times 10^{-5}$ s 1.0×10^{-5} s 3.0×10^{-5} s 10×10^{-5} s

(a) Detachment of microbubble; pattern A.

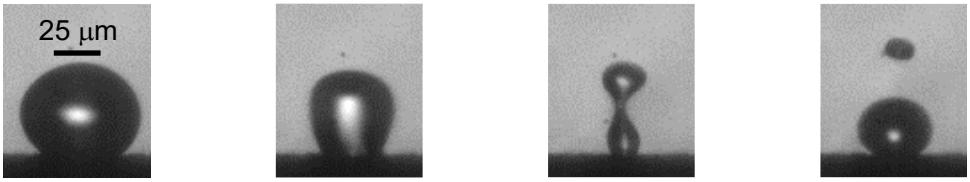

$t = t_0 + 0.0 \times 10^{-5}$ s 0.5×10^{-5} s 3.0×10^{-5} s 10×10^{-5} s

(b) Breakup of vapor bubble; pattern B.

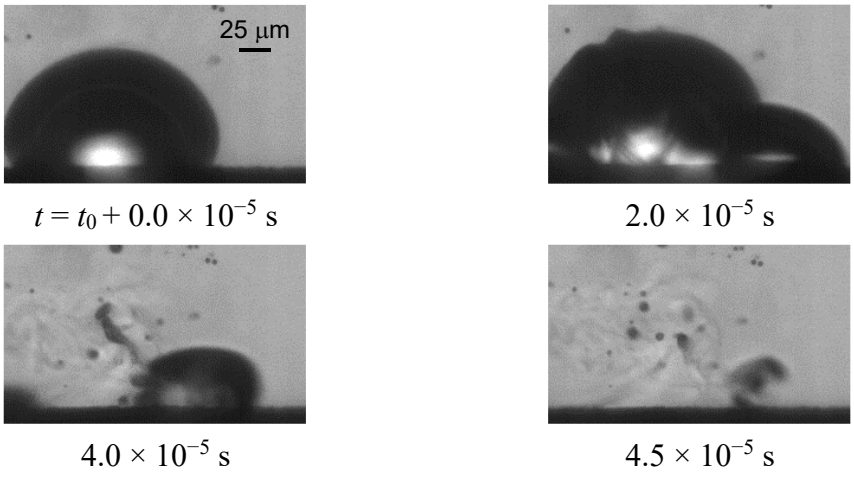

$t = t_0 + 0.0 \times 10^{-5}$ s 2.0×10^{-5} s

4.0×10^{-5} s 4.5×10^{-5} s

(c) Collapses of vapor bubble; pattern C.

Fig. 4.10 Process of microbubble generation.

The probability density function, $P(d_B)$, of the bubble diameter is shown in Fig. 4.11. The total numbers of samples used in the calculation of $P(d_B)$ were 3.5×10^5, 8.9×10^4 and 7.4×10^4 at $DO = 8.5 \times 10^{-3}$, 4.5×10^{-3} and 0.05×10^{-3} kg/m^3, respectively. The peak diameter around 10 μm slightly increases and the distribution becomes broader as DO increases, which results in the increase in the mean bubble diameter $\overline{d}_B$ with increasing DO as shown in Fig. 4.12. The effects of DO on $\overline{n}_B$ is also shown in Fig. 4.12. The $\overline{n}_B$ increases with increasing DO. This is due to the increases in nucleation rate [16, 17] and in

active nucleation sites on the wire surface as the concentration of dissolved incondensable gas increases. The number density of 10^{11} m^{-3} is several times larger than that obtained with the pressurized dissolution method [7]. Nitrogen was also dissolved in water as well as oxygen, and the concentration of nitrogen in the saturated condition can be estimated as 14.0 × 10^{-3} kg/m^3 at 298 K and 9.6 × 10^{-3} kg/m^3 at 373 K from Henry's law. The total concentration of the dissolved incondensable gases is estimated as 22.5 × 10^{-3}, 11.9 × 10^{-3}, and 9.65 × 10^{-3} kg/m^3 for DO = 8.5 × 10^{-3}, 4.5 × 10^{-3} and 0.05 × 10^{-3} kg/m^3, respectively. Hence, the small difference in $\overline{n}_B$ between DO = 4.5 × 10^{-3} and 0.05 × 10^{-3} kg/m^3 conditions is due to the small difference in the total concentration of dissolved gases.

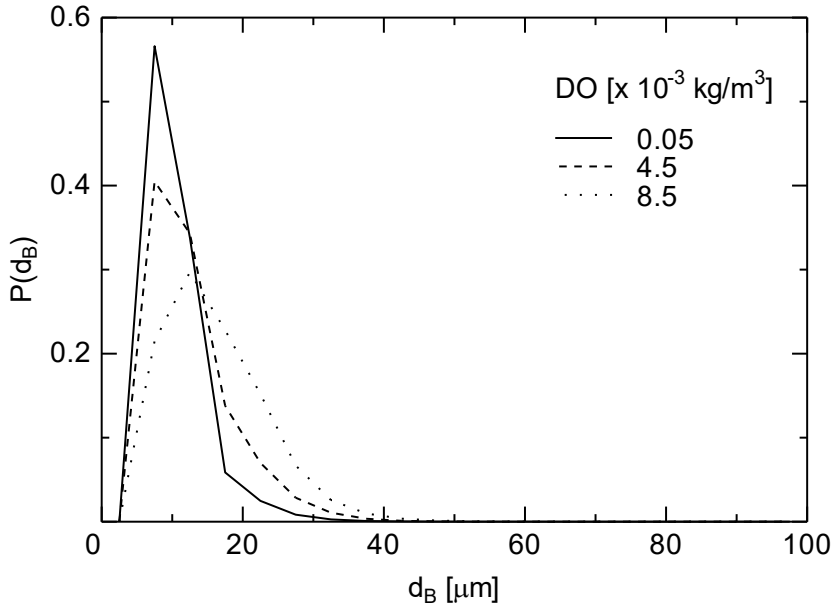

Fig. 4.11 Bubble size distribution ($\overline{q}$ = 4.5 MW/m^2, f = 60 Hz).

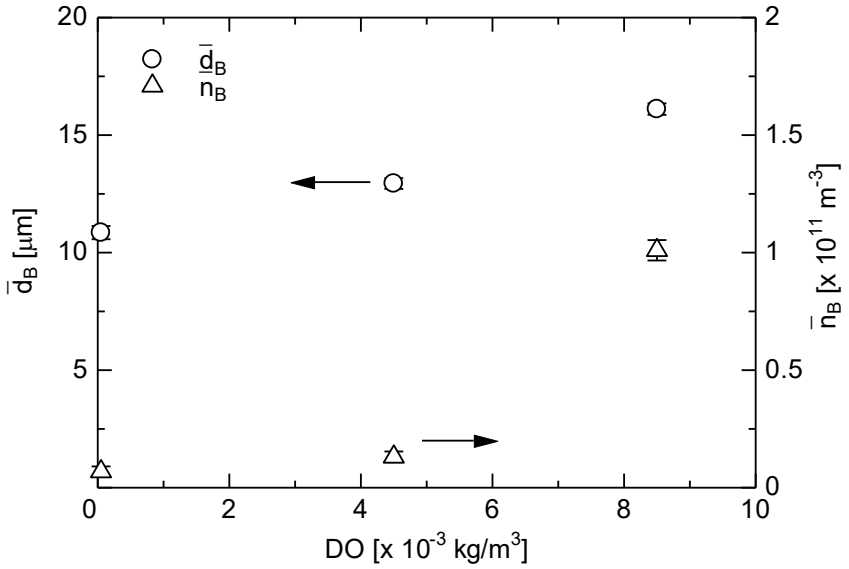

Fig. 4.12 Effect of *DO* on $\bar{d}_B$ and $\bar{n}_B$ ($\bar{q}$ = 4.5 MW/m^2, f = 60 Hz).

4.3.1.2 Microbubble generation mechanism

Based on the dependence of the bubble diameter and the number density on *DO*, the generation mechanism of microbubbles in the subcooled boiling method can be summarized as follows. Vapor bubbles are generated on the heated surface as schematically shown in Fig. 4.13 (a) when the platinum wire is heated by electric current. In fact, the bubbles consist not only of vapor but also of incondensable gases, e.g., oxygen and nitrogen, coming from the liquid phase during the bubble growth. The bubble size can be as large as several hundred microns at the bubble growth stage (Fig. 4.9 (d)). Then the bubbles are released from the wire or collapse, and rapidly shrink in the subcooled water due to the condensation of vapor, while the incondensable gases remain inside the bubbles. Thus, microbubbles consisting of the incondensable gases appear in the bulk liquid (Fig. 4.13 (b)). Note that the microbubbles contain a very small amount of vapor which is determined by Dalton's law. When the concentration of the dissolved incondensable gases increases, the number of incondensable gas molecules in the vapor bubbles generated by the heating increases, which results in increase of the number of molecules in the generated microbubbles, i.e., the size of the generated microbubbles. The number of generated microbubbles also increases with the

concentration of the dissolved gases due to the increase of bubble nuclei.

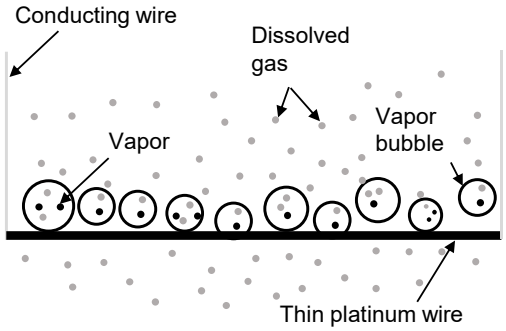

(a) Vapor bubble generation.

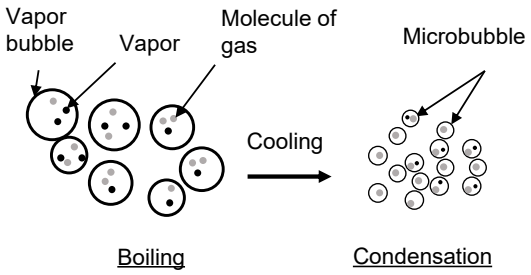

(b) Microbubbles consisting of incondensable gases.

Fig. 4.13 Microbubble generation process.

4.3.2 Influence of heat flux with DC and AC

4.3.2.1 Boiling curve of DC and AC

(a) Boiling curve of DC

Fig. 4.14 shows the boiling curve obtained by heating with DC. The abscissa is the difference between T_W and the saturation temperature, ΔT_{sat}, and the ordinate is $\overline{q}$. The boiling curve obtained by Shoji et al. [18] is also shown in the figure. Shoji et al. measured the boiling curve in degassed water by heating a platinum wire with a diameter of 200 μm by DC current. The ΔT_{sat} increases as $\overline{q}$ increases, and $\overline{q}$ increases as the degree of subcooling, ΔT_{sub},

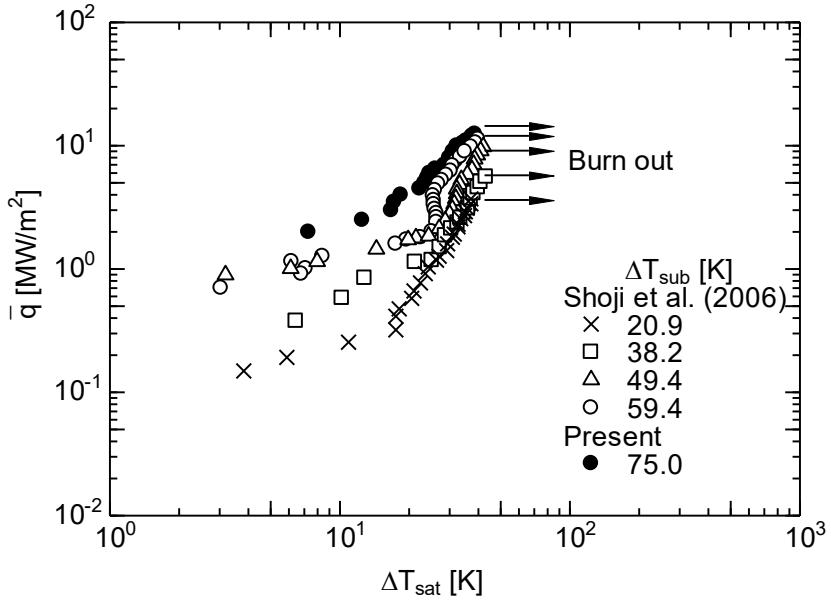

Fig. 4.14 Boiling curve for DC [16].

increases when compared at the same ΔT_{sat}. It was also found that $\bar{q}$, or CHF (Critical Heat Flux) at ΔT_{sat} of burn out, increases with an increase in ΔT_{sub}. The boiling curve obtained in this experiment shows the same trend as that of Shoji et al. Therefore, the relationship between $\bar{q}$ and T_{sat} in this experiment corresponds to the boiling curve in pool boiling.

(b) Boiling curve of AC

The boiling curve obtained with AC heating is shown in Fig. 4.15, which shows the relationship between q and ΔT_{sat} for one heating cycle, and the DC boiling curve obtained in this experiment is also shown. Compared to the DC boiling curve, the overall ΔT_{sat} is higher for DC at the same q, but ΔT_{sat} is higher for AC in the latter half of the period when q is decreasing. In the case of DC, ΔT_{sat} has reached the steady-state temperature at q because of the long heating time at constant q. In the case of AC, ΔT_{sat} is higher than that of DC because of the long heating time at constant q. On the other hand, in the case of AC, since q varies, the steady-state temperature is not reached at any q. The temperature tends to be lower than that of DC in the region where q increases and higher than that of DC in the region where q

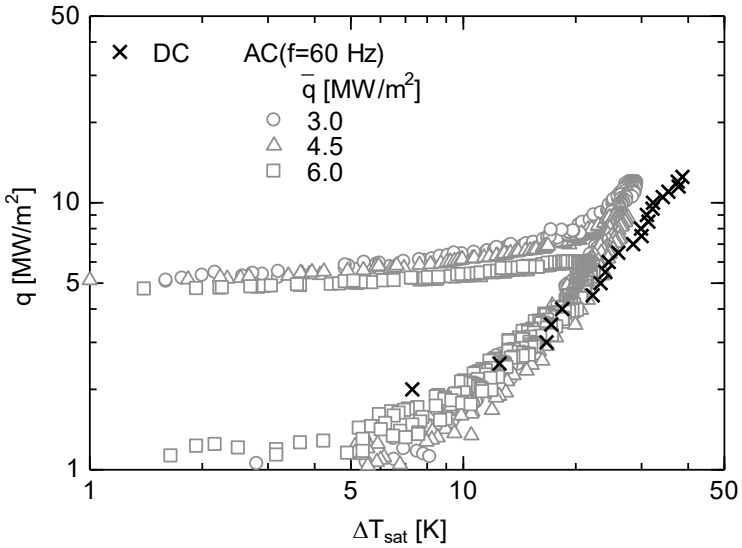

Fig. 4.15 Boiling curve for AC.

decreases. In particular, when q tends to increase, ΔT_{sat} increases from the cooled state by the ambient liquid, and the difference between ΔT_{sat} and DC is large. On the other hand, when q is decreasing, ΔT_{sat} is lower than that of DC at the beginning of the decrease in q because T_W is cooled from the already heated state.

4.3.2.2 Effects of DC and AC on microbubble generation

In order to discuss the effects of the heating condition on the microbubble generation, $\overline{d}_B$ and $\overline{n}_B$ of microbubbles generated with the electric heating of DC (constant heating) and AC (cyclic heating) (f = 60 Hz) were compared for $1.5 \leq \overline{q} \leq 6.0$ MW/m^2. Note that the boiling regime observed was the nucleate boiling in all the conditions. Fig. 4.16 (a) shows that at $\overline{q}$ = 1.5 MW/m^2, bubbles attaching to the platinum wire grow up to about 0.6 mm diameter and reach the quasi-equilibrium state, while few microbubbles are generated for both DC and AC. On the other hand, as shown in Fig. 4.16 (b)–(d), microbubbles are generated for $\overline{q} \geq 3.0$ MW/m^2, and the amount of bubbles increases as $\overline{q}$ increases. Microbubbles were confirmed for $\overline{q} \geq 3.0$ MW/m^2 in DC and $\overline{q} \geq 2.5$ MW/m^2 in AC. The reason why the minimum $\overline{q}$ required for microbubble generation in AC is slightly lower than in DC is as follows.

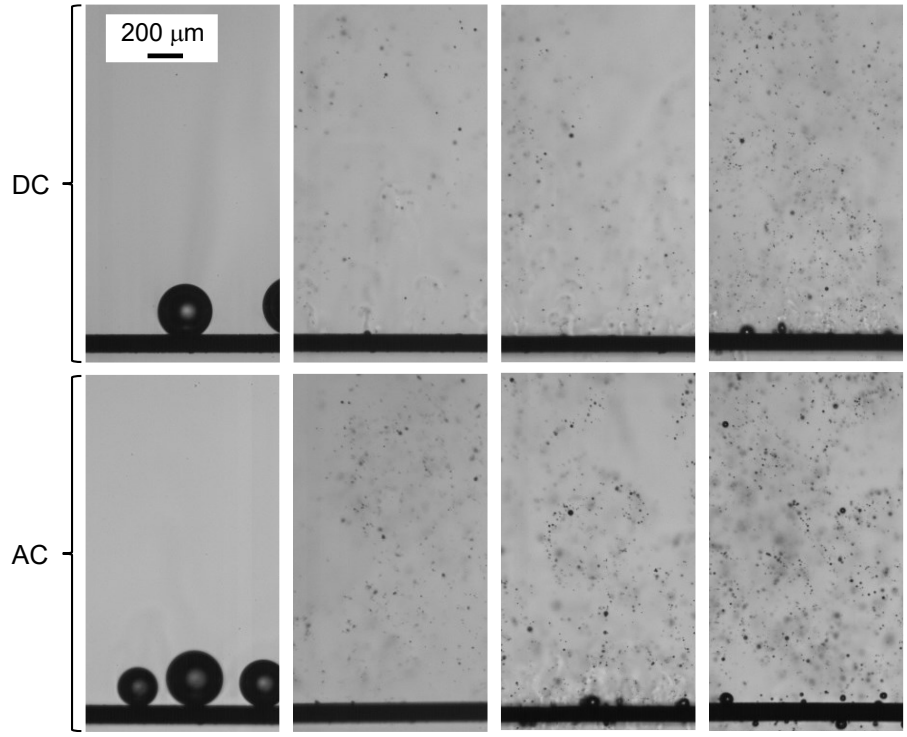

(a) $\bar{q}$ [MW/m^2] = 1.5 (b) 3.0 (c) 4.5 (d) 6.0

Fig. 4.16 Images of generated microbubbles (Top: DC, Bottom: AC).

The wire surface temperature T_W during one cycle and the bubble generation process at $\bar{q}$ = 4.5 MW/m^2 are shown in Fig. 4.17 and Fig. 4.18, respectively. Since T_W is constant in the DC case, microbubbles were generated from vapor bubbles at a constant generation rate (Fig. 4.18 (a)) and the bubble generation pattern was mainly Pattern A (detachment) and B (single breakup) in Fig. 4.10. On the other hand, the bubble generation rate with AC fluctuates as shown in Fig. 4.18 (b)–(d), where P_A, P_B and P_C represent the instants shown in Fig. 4.17. The bubble generation is not observed at the low temperature of P_A (Fig. 4.18 (b)), while microbubbles are generated at P_B, where T_W is higher than the surface temperature with DC and the microbubble generation due to bubble collapse (Pattern C in Fig. 4.10 (c)) is mainly observed. The bubble collapse efficiently produces multiple microbubbles, and consequently, the number of microbubbles generated with AC is larger than that with DC. As shown in Fig. 4.16 (c) and (d), the numbers of bubbles on the wire in the AC cases are larger than those in the DC cases. This implies that the number of active cavities in the AC cases are larger than those in the DC cases because of the higher maximum heat flux.

Thermophoresis of the microbubbles toward the wire surface due to high temperature gradient in the vicinity of the wire was also observed during the no bubble generation period in AC cases. The microbubbles move to the wire surface and play the role as nuclei in the subsequent boiling period. These are also the reason of high bubble generation rate in the AC cases.

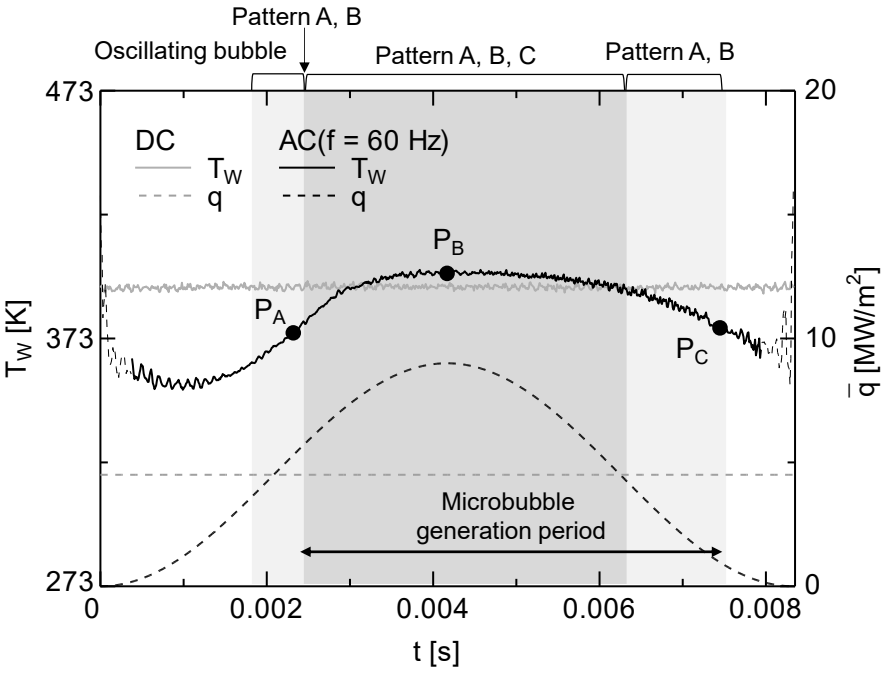

Fig. 4.17 Heat transfer surface temperature during one cycle ($\bar{q}$ = 4.5 MW/m^2).

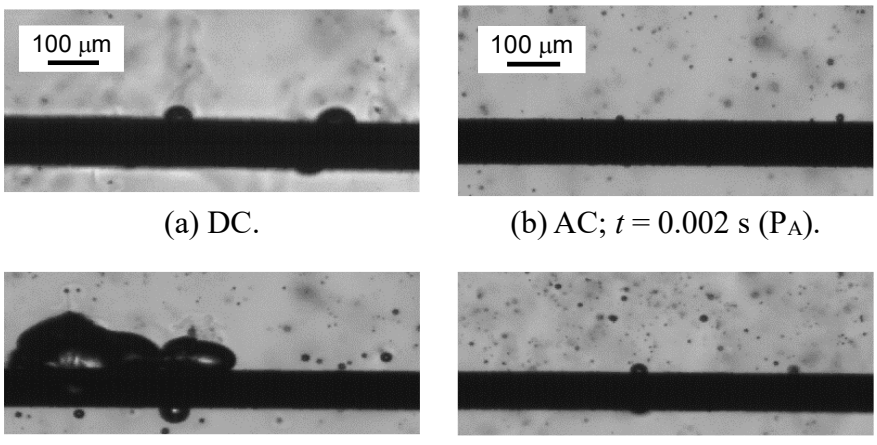

(a) DC. (b) AC; t = 0.002 s (P_A).

(c) AC; t = 0.004 s (P_B). (d) AC; t = 0.007 s (P_C).

Fig. 4.18 Generation state with different heat transfer surface temperature.

Fig. 4.19 shows the relationship between $\bar{q}$ and $\bar{n}_B$. The $\bar{n}_B$ increases with increasing $\bar{q}$ for both DC and AC. Hence, $\bar{n}_B$ can be easily controlled by changing electric current. The larger $\bar{n}_B$ with AC implies that AC can generate microbubbles more efficiently than DC. The $P(d_B)$s of the bubble diameter are shown in Fig. 4.20; the peaks appear around 15 μm for both DC and AC, and the probability around 20–40 μm increases as $\bar{q}$ increases. Fig. 4.21 shows the relationship between $\bar{q}$ and $\bar{d}_B$. The $\bar{d}_B$ slightly increases as $\bar{q}$ increases for both DC and AC, whereas AC gives somewhat larger $\bar{d}_B$.

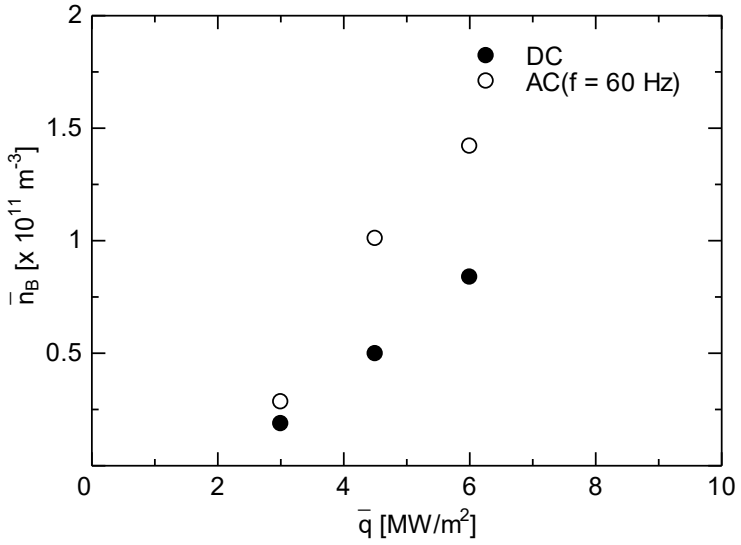

Fig. 4.19 Effects of $\bar{q}$ on $\bar{n}_B$.

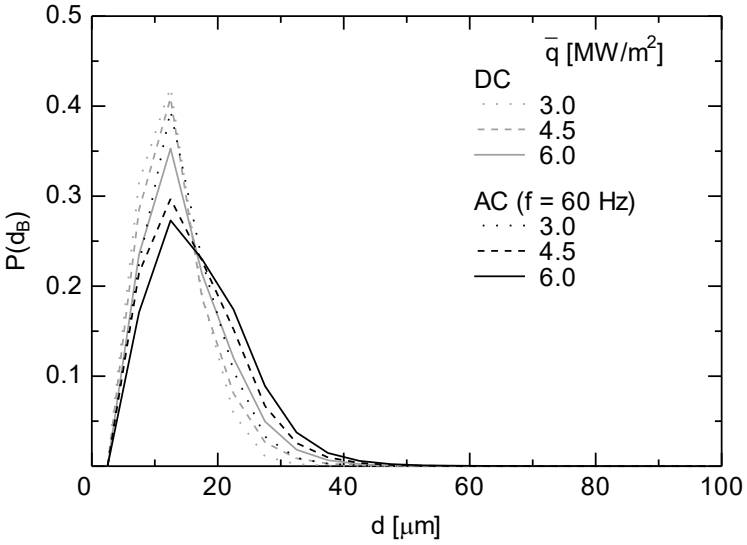

Fig. 4.20 Bubble size distribution.

The relationship between $\overline{q}$ and the average void fraction, $\overline{\alpha}$, is shown in Fig. 4.22. For both DC and AC, $\overline{\alpha}$ increases as $\overline{q}$ increases. In addition, $\overline{\alpha}$ is about 2 to 3 times higher for AC than for DC at the same $\overline{q}$.

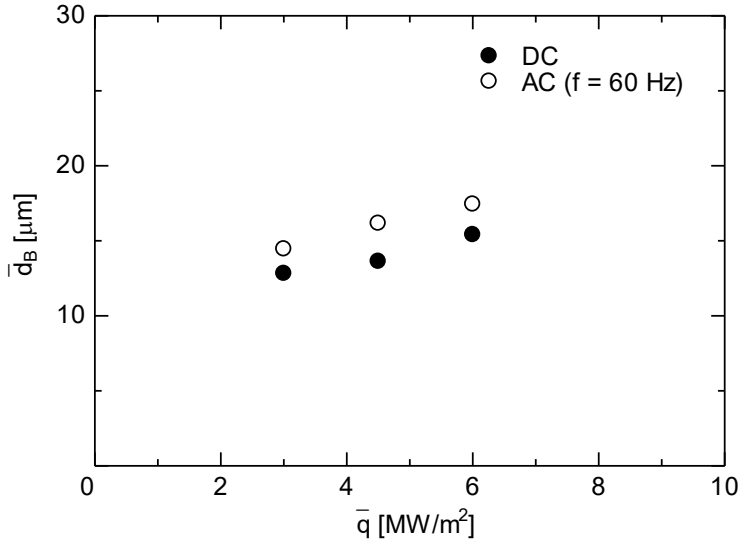

Fig. 4.21 Effects of $\overline{q}$ on $\overline{d}_B$.

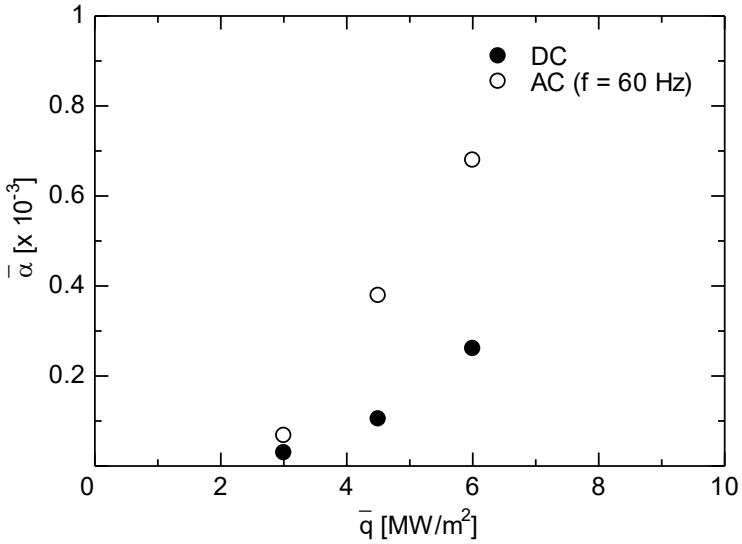

Fig. 4.22 Effects of $\overline{q}$ on $\overline{\alpha}$.

There are two possible reasons for the higher bubble generation rate in the AC cases than in the DC cases. The first is that AC cases cause more bubbles to reattach to the fine

wire. For the number of reattached bubbles measured over the same time period (1 heating cycle: 1/120 s), the number was 7 for DC and 25 for AC. Second, the number of bubble nucleus was higher for AC than for DC. For the number of bubble nucleus measured over the same time period (one heating cycle: 1/120 s), the number was 10 for DC and 51 for AC. The number of bubbles in AC was found to be five times higher than in DC. This is due to the fact that at the same average heat flux, the maximum heat flux in the AC case is larger than in the DC case. The number of bubble collapses is higher in the AC case than in the DC case (Pattern B and C). From the above, it is considered that higher number of microbubbles is generated in the AC cases due to the increase in the number of bubble nucleus.

4.3.3 Influence of AC frequency

The f was varied in the range of $15 \leq f \leq 960$ Hz to investigate the influence of f on the microbubble generation in the cyclic heating. The $\overline{q}$ was fixed at 4.5 MW/m^2. Fig. 4.23 shows the state of microbubble generation at time t = 30 s after heating started. The number of bubbles with large diameters decreases as f increases as can also be confirmed in Fig. 4.24 (a). Fig. 4.24 (b) shows the relationship between f and $\overline{n}_B$. Though the increase in f decreases $\overline{d}_B$, $\overline{n}_B$ is deteriorated as f increases; the reduction in $\overline{n}_B$ is about 40% by the increase in f from 60 to 240 Hz. Both $\overline{d}_B$ and $\overline{n}_B$ approach those values in the DC case as f increases.

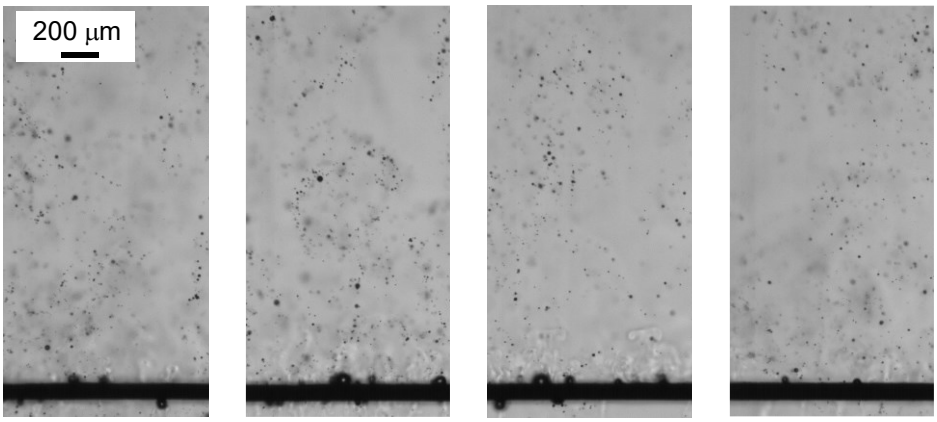

f = 15 Hz 60 Hz 240 Hz 960 Hz

Fig. 4.23 Microbubbles generated with different AC frequencies (AC, $\overline{q}$ = 4.5 MW/m^2).

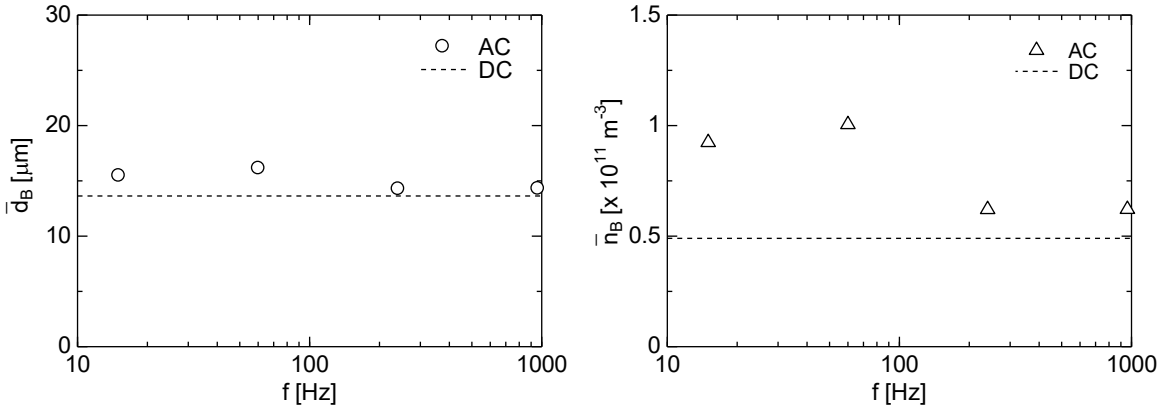

(a) (b)

Fig. 4.24 Relations between f, $\bar{d}_B$ and $\bar{n}_B$.

4.3.4 Microbubble generation using a nichrome wire

Since nichrome wires are often used as a heating element, the performance of the bubble generation method with a nichrome wire was also examined. The nichrome wire (Nilaco, 691167) of 0.10 mm diameter and 30 mm length was used, which was preliminary heated once for a sufficient time to form an oxide film to promote the detachment of microbubbles from the wire. The $\bar{q}$ was 4.5 MW/m^2 and 6.0 MW/m^2. The power supply was AC. Fig. 4.25 shows the state of microbubble generation captured at t = 30 s. The microbubbles can be generated by the nichrome wire and the generated bubbles are relatively larger than those generated by the platinum wire. The effects of $\bar{q}$ on $\bar{d}_B$ and $\bar{n}_B$ are shown in Table 4.4. Being similar to the cases with the platinum wire, $\bar{d}_B$ and $\bar{n}_B$ obtained with the nichrome wire increase with increasing $\bar{q}$. At the same $\bar{q}$, there is no significant difference in $\bar{d}_B$ between the platinum and nichrome wires, but $\bar{n}_B$ is lower for the nichrome wire. These differences can be attributed to the difference in the surface structure, i.e., the size and number of cavities made by polishing with the sandpaper and surface oxidization.

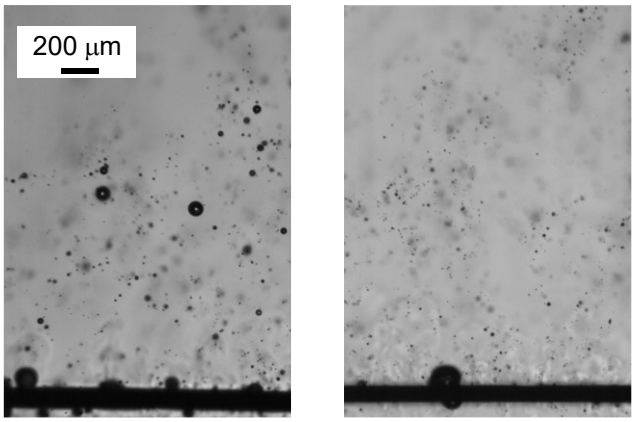

(1) Nichrome wire (2) Platinum wire

(a) $\bar{q}$ = 4.5 MW/m^2

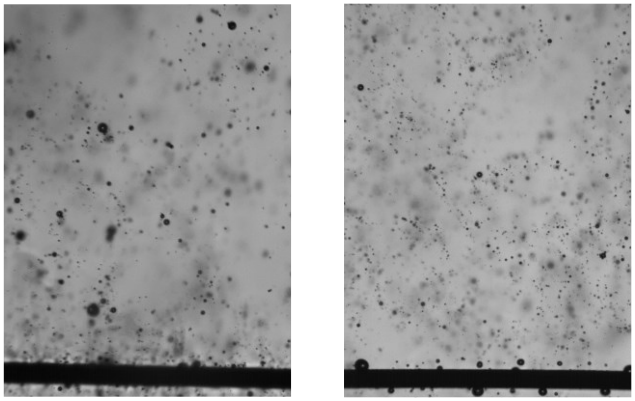

(1) Nichrome wire (2) Platinum wire

(b) $\bar{q}$ = 6.0 MW/m^2

Fig. 4.25 Comparison in bubble generation state between nichrome and platinum wires.

Table 4.4 $\bar{d}_B$ and $\bar{n}_B$ at each $\bar{q}$.

AC, f = 60 Hz	$\bar{q}$ [MW/m^2]	3.0	4.5	6.0
$\bar{d}_B$ [μm]	Platinum wire	14	16	17
	Nichrome wire	—	17	18
$\bar{n}_B$ [× 10^{11} m^{-3}]	Platinum wire	0.28	1.01	1.42
	Nichrome wire	—	0.52	0.71

4.4 Application of bubble generation method based on subcooled boiling to oil removal effects

The characteristics of microbubbles generated using the proposed method have been discussed up to the previous section. This method can generate bubbles in stagnant liquid pools without pumps or complex piping systems. The position, shape, and number of heating wires can be changed so as to be suitable for various applications. It is necessary to consider the importance of generating microbubbles in a position where they can act on dirt for efficient cleaning. Therefore, in this section, the performance of the proposed method is briefly examined for a cleaning process of highly viscous oil.

Fig. 4.26 shows an experimental setup for a cleaning application submerged in a water pool, which mainly consisted of the heating thin metal wire, the power source (Matsusada, SRJ500), the water tank and the dirt plate (40 × 40 mm in width and length). A nichrome wire (Nilaco, 691167) of 0.10 mm diameter and 30 mm length was soldered with lead wires. The acrylic water tank of 80 × 160 × 120 mm in width, depth and height was filled with water of 1.0×10^{-3} m^3. Lard oil (MIYOSHI OIL & FAT CO., LTD.) was adhered to the dirt plate with a thickness of 4 mm. The viscosity and density of the lard oil are 40.6 mPa·s (at $T = 311$ K) and 914 kg/m^3, respectively [19]. The water temperature was set at $T = 300 \pm 0.5$ K. The cleaning time was 10 min, and the dirt locations were $L = 20 \pm 0.5$ mm and 60 ± 0.5 mm above the wire. $DO = (8.5 \pm 0.3) \times 10^{-3}$ kg/m^3 and $\overline{q} = 4.5$, 6.0 MW/m^2 (AC, $f = 60$Hz).

Fig. 4.27 shows the results of the different installation distance L and $\overline{q}$. The left side is the bottom view and the right side is the reversed front view. The right side of the graphs in Figs. 27 (a), (b) and (c) shows the height of the highest point of the lard oil after cleaning. The relation among $\overline{q}$, L and the residual volume of lard oil at the plate, V_{res}, is shown in Table 4.5. Fig. 4.27 (a) is the initial state of lard oil adhering to the plate. Figs. 4.27 (b) and (d) show the different cleaning effects caused by different $\overline{q}$. Section 2.3.2 shows that the number density of microbubbles affects the cleaning effect and that the number density of bubbles generated by Section 4.3.2 increases with $\overline{q}$. The consistent results were obtained, i.e., the oil removal was enhanced by increasing $\overline{q}$. Figs. 4.27 (c) and (d) show the different

cleaning effects caused by different L. In a stagnant pool, the farther away microbubbles are from the generator, the less likely they are to reach the dirt by natural convection, thus weakening their cleaning effect (c). On the other hand, the closer the microbubbles are to the generator, the more efficiently they can act on the dirt (b). The experimental results have thus demonstrated that generating bubbles near a removal target using the proposed method is effective to enhance the cleaning effect.

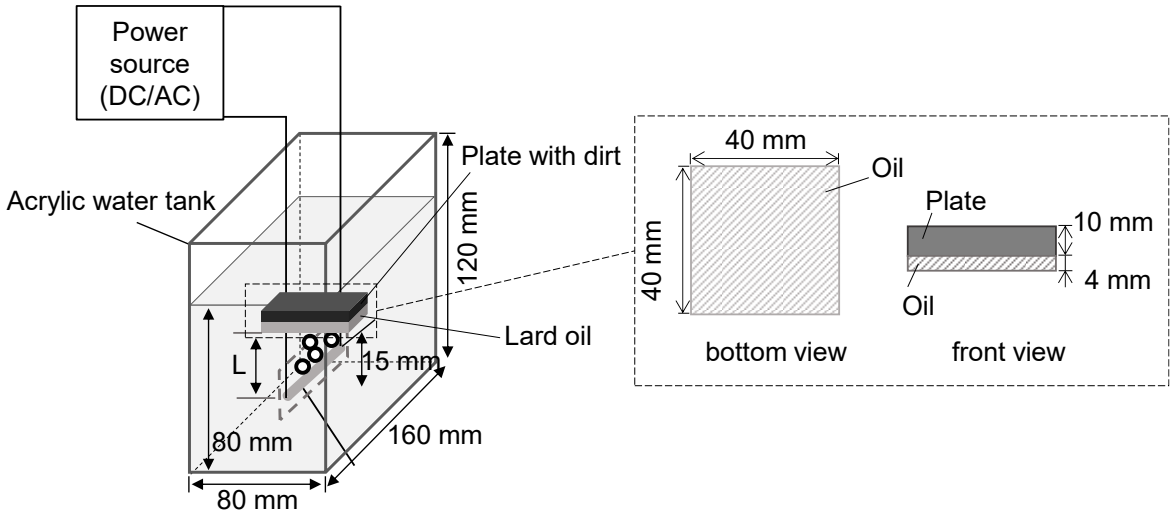

Fig. 4.26 Experimental setup for cleaning.

Table 4.5 Relation of $\bar{q}$, L and V_{res}.

$\bar{q}$ [MW/m^2]	L [mm]	V_{res} [mm^3]
4.5	20	3410
6.0	20	4147
6.0	60	5020

(a) t = 0 min.

(b) $\overline{q}$ = 4.5 MW/m^2, L = 20 mm.

(c) $\overline{q}$ = 6.0 MW/m^2, L = 20 mm.

(d) $\overline{q}$ = 6.0 MW/m^2, L = 60 mm.

Fig. 4.27 Effects of L and $\overline{q}$ on oil removal. (t = 10 min in cases (b), (c) and (d)).

4.5 Conclusions

The feasibility of microbubble generation using subcooled boiling with an electrically heated thin wire was confirmed and the diameter and number density of generated microbubbles were measured from high-speed video images. As a result, the following results were obtained:

(1) The proposed method can generate microbubbles at a high number density. The dependence of the bubble number density on the concentration of the dissolved oxygen implies that microbubbles consist of incondensable gases transferred from the liquid phase into vapor bubbles during the bubble growth in boiling and the subsequent condensation.

(2) The cyclic heating with AC is more effective for generating microbubbles than the constant heating with DC.

(3) The number density increases with increasing the time-averaged heat flux, which also increases the mean bubble diameter though the increasing rate of the diameter is not significant.

(4) Both platinum and nichrome wires can be used for the proposed method. The effects of the heat flux on the bubble size and number density are qualitatively the same for both materials.

References for Chapter 4

[1] M. Sadatomi, A. Kawahara, K. Kano, A. Ohtomo, Performance of a new micro-bubble generator with a spherical body in a flowing water tube, *Exp. Thermal Fluid Sci*., vol. 29, 615–623, 2005.

[2] A. Fujiwara, S. Takagi, K. Watanabe, Y. Matsumoto, Experimental study on the new micro-bubble generator and its application to water purification system, *ASME/JSME 2003 4th Joint Fluids Summer Engineering Conference*, FEDSM2003-45162, 469–473, 2003.

[3] T. Makuta, F. Takemura, E. Hihara, Y. Matsumoto, M. Shoji, Generation of micro gas bubbles of uniform diameter in an ultrasonic field, *J. Fluid Mech*., vol. 548, 113–131, 2006.

[4] T. Makuta, R. Suzuki, T. Nakao, Generation of microbubbles from hollow cylindrical ultrasonic horn, *Ultrasonics*, vol. 53, 196–202, 2013.

[5] A. Thiemann, T. Nowak, R. Mettin, F. Holsteyns, A. Lippert, Characterization of an acoustic cavitation bubble structure at 230 kHz, *Ultrason. Sonochem*., vol. 18, 595–600, 2011.

[6] P. S. Russell, D. R. Giosio, J. A. Venning, B. W. Pearce, P. A. Brandner, S. L. Ceccio, Microbubble generation from condensation and turbulent breakup of sheet cavitation, *31st Symposium on Naval Hydrodynamics Monterey*, *California*, 2016.

[7] Y. Maeda , S. Hosokawa , Y. Baba, A. Tomiyama, Y. Ito, Generation mechanism of micro-bubbles in a pressurized dissolution method, *Exp. Thermal Fluid Sci*., vol. 60, 201–207, 2015.

[8] S. Hosokawa, K. Tanaka, Y. Maeda, A. Tomiyama, A. Yamaguchi, Y. Ito, Effect of entrained air bubbles generated by a pressurized dissolution method, *Trans. JSME B*, 76, 53–60, 2010.

[9] K. Tabei, S. Haruyama, S. Yamaguchi, H. Shirai, F. Takakusagi, Study of micro bubble generation by a swirl Jet, *J. Environ. Eng*., vol. 2, 172–182, 2007.

[10] K. Koide, S. Kato, Y. Tanaka, H. Kubota, Bubbles generated from porous plate, *J. Chem. Eng. Jpn*., vol. 1, 51–56, 1968.

[11] A. M. Aliyu, H. Seo, M. Kim, K. C. Kim, An experimental study on the characteristics of ejector-generated bubble swarms, *J. Vis*., vol. 21, 711–728, 2018.

[12] Catalag of Pure Metals, *The Nilaco Corporation*, No. 34.

[13] M. Jamialahmadi, A. Helalizadeh, H. M€uller-Steinhagen, Pool boiling heat transfer to electrolyte solutions, *Int. J. Heat Mass Trans*., vol. 47, 729–742, 2004.

[14] J. R. Simonson, Engineering heat transfer, *Palgrave Macmillan London*, 1988.

[15] JIS C 1604–1997, *IEC Pub.*751–1995.

[16] S.D. Lubetkin, Why is it much easier to nucleate gas bubbles than theory predicts, *Langmuir*, vol. 19, 2575–2587, 2003.

[17] Y. Mori, K. Hijikata, T. Nagatani, Effect of dissolved gas on bubble nucleation, *Int. J. Heat Mass Trans*., vol. 19, 1153–1159, 1976.

[18] M. Shoji, Microbubble emission boiling and its possible application, *Science Reports of Research Institute for Engineering Kanagawa University*, vol. 29, 2–9, 2006.

[19] R. Jeantet, T. Croguennec, P. Schuck, G. Brulé, Handbook of food science and technology 1: Food alteration and food quality, *Wiley-ISTE*, 2016.

Chapter 5

Conclusions

Microbubbles have a long residence time in the liquid phase, high internal pressure and high interfacial area concentration due to their small diameter, which often promote physical and chemical phenomena related to the interface. Microbubbles with these properties have been widely used in the agricultural, marine, and environmental fields. In recent years, environmental problems have spread, especially water pollution. Therefore, microbubbles consisting only of air and water are expected to be applied to the cleaning process. Factors that make water containing microbubbles effective for cleaning include the abrasive effect of bubbles, the effect of surface charge, the adsorption of dirt at the gas-liquid interface, and the lifting effect of the bubbles on dirt. However, none of these factors has been clearly proven, and the detailed mechanism regarding the removal effect has not been fully elucidated. In addition, in order for microbubbles to perform well in their application, it is necessary to understand the change in diameter and number density of microbubbles. Furthermore, the generation of microbubbles is very important in the microbubble cleaning process. However, most current generation methods are costly and large in size, thus, low-cost and compact generation methods are expected. By overcoming these issues, the application of microbubbles can be expanded.

Hence, in this dissertation, the objective was to clarify the relationship between the behavior of microbubbles near oil and the removal process, and to examine the diameter change of microbubbles and the mechanism of microbubble generation in order to obtain design guidelines for removal mechanisms and new microbubble generators.

In chapter 2, dirt removal experiments were conducted using viscous silicone oil adhering to the bottom wall of a horizontal rectangular channel, and the effects of microbubbles on oil removal from the wall was investigated by continuously measuring the thickness change of the contamination using a fluorescence-induced method. The bubble diameter and number density in the vicinity of the wall surface were also measured to investigate the removal rate enhanced by microbubbles. The behavior of microbubbles attached to dirt was also examined to investigate the cleaning mechanism of microbubbles. As a result, the following conclusions were obtained:

(1) The amount of oil removed by the water flow increases with increasing the Reynolds number, showing that the water flow has cleaning effects even without microbubbles. This is attributed to the shear stress acting on the oil interface.
(2) Adding microbubbles to the water flow increases the amount of oil removal. In other words, microbubbles have a removal enhancement effect. The higher the bubble number density, the larger the removal effect is. The removal effect of microbubbles can be evaluated by a model which assumes that the amount of oil removal is proportional to the number of microbubbles in the vicinity of oil interface.
(3) The removal rate can be modeled as a superposition of the effects of shear stress and the presence of microbubbles.
(4) Microbubbles adhering to oil under turbulent conditions can be grown by mass transfer. The cleaning effect is largely promoted by peeling of the oil by the detachment of large bubbles grown on the oil interface.

Based on the discussion of conclusions (4), the bubble diameter variation of microbubbles is an important parameter for microbubble applications. Numerical calculations of bubble diameter variation for single bubbles and groups of bubbles based on Henry's law and the Rayleigh-Plesset equation were therefore proposed as follows.

In chapter 3, at first, numerical simulations based on the Rayleigh–Plesset equation and the one-dimensional advection-diffusion equation were carried out to validate the change in bubble diameter for the single growing bubble discussed in Chapter 2. Then, the validation

for single shrinking bubble and the time evolution of bubble diameter and the mass transfer of dissolved gas between bubbles and water after bubble generation for microbubble groups were investigated. As a result, the following conclusions were obtained:

(5) The present numerical method can accurately predict the growth and shrinkage of a single microbubble.
(6) Microbubbles in water flows usually have size distribution and bubbles larger and smaller than the equilibrium bubble diameter become larger and smaller in time, respectively. The size distribution thus changes in time.
(7) The proposed numerical method can reasonably predict time evolutions of bubble size distributions, void fractions and concentrations of dissolved gas, provided that a reliable initial condition is available. Since the numerical simulation assumes that no bubble nucleation occurs in the downstream region of the nozzle, the agreement between the prediction and the experiments proves weak influence of the bubble nucleation on the mass transfer between the phases.

Conclusions (4) and (5) demonstrated that microbubbles attached to dirt and grown under turbulent flow conditions, thereby promoting the cleaning effect. However, when the water flow is slow, it is difficult for microbubbles to adhere to dirt. Therefore, a compact and low-cost generation method that can generate microbubbles in the vicinity of stains dirt is considered necessary.

In chapter 4, a microbubble generation method based on subcooled boiling on a heated wire in a liquid with dissolved incondensable gases was proposed. The proposed method does not require pumps or complex piping systems to generate bubbles in stagnant liquid pools. The location, shape, and number of heating wires can be changed according to the application. Since the bubble diameter and number density are important parameters of the microbubble generation method, the performance of the proposed method was evaluated by measuring them with a high-speed video camera. As a result, the following conclusions were obtained:

(8) The proposed method can generate microbubbles at a high number density. The

dependence of the bubble number density on the concentration of the dissolved oxygen implies that microbubbles consist of incondensable gases transferred from the liquid phase into vapor bubbles during the bubble growth in boiling and the subsequent condensation.

(9) The cyclic heating with AC is more effective for generating microbubbles than the constant heating with DC.

(10) The number density increases with increasing the time-averaged heat flux, which also increases the mean bubble diameter though the increasing rate of the diameter is not significant.

(11) Both platinum and nichrome wires can be used for the proposed method. The effects of the heat flux on the bubble size and number density are qualitatively the same for both materials.

As mentioned above, it is expected that the cleaning mechanisms clarified in this study can be considered in manufacturing for practical applications. In addition, the developed microbubble generation method can directly supply microbubbles to the target area for cleaning in the cleaning field or necessary place in the other fields. Therefore, by using this technology in future design and development, it can be expected that new developments will be possible by increasing the number density locally.

Appendix A

Evaluation of the amount of bubble generation

In Chapter 4, a method to generate microbubbles by subcooled boiling in still water was proposed. This method does not require water flow and is proposed for practical use in the field of compact cleaning system. It may also have a potential for application in water flow. Therefore, the amount of microbubbles produced by the method in a flowing water is discussed in this appendix.

A.1 Experimental setup and evaluation method

A.1.1 Experimental setup

The amount of generated microbubbles is important for understanding the efficiency of bubble generation methods, the generation process, and design. However, in a pool water, it is difficult to evaluate the amount of generated bubbles because all bubbles generated do not flow in the same direction and their velocity fluctuates greatly. Therefore, the evaluation of the amount of bubbles was attempted by generating microbubbles in a flowing water and enforcing them to flow in the specified direction. A schematic of the experimental apparatus used is shown in Fig. A.1 which mainly consists of a tank, a test section, a pump (IWAKI, MD-6ZK), and a power supply. A high-speed camera (Photron, SA-X2) was used to capture the microbubbles generated by heating the platinum wire by applying voltage to it. Pure water

(T_0 = 298 ± 0.5 K, DO_0 = (8.5 ± 0.3) × 10^{-3} kg/m^3) purified by a water purification system (Millipore, Elix3) was used for the liquid phase. Water in the tank was suctioned by a pump and passed through the test section. The dimensions of the test section were 5 × 50 × 600 mm in width, depth and height, respectively. A compression fitting was used to fix the platinum wire, which was fixed straight by applying tension. The power source was either a AC power supply (NF ELECTRONIC INSTRUMENTS, 4210 P-STATION MINI) or a DC power supply (ALINCO, DM130MV).

In order to ensure that the generated bubbles flow without backflow, the Reynolds number $Re' < 6$ around the cylinder, where no Karman vortex is generated, [1]:

$$Re' = \frac{\rho \bar{u} d_p}{\mu} \tag{A.1}$$

where d_p is the diameter of platinum wire, $\bar{u}$ the cross-sectional mean velocity, ρ the density of water, and μ the viscosity of water. Here, μ = 0.89 mPa·s at T = 298 K, thus, $\bar{u}$ < 0.06 m/s. The entrance length, L_e, was calculated by Eq. (A.2).

$$L_e = 0.06 Re' d_H \tag{A.2}$$

L_e = 297 mm when $\bar{u}$ = 0.06 m/s in laminar flow, and the position of the wire was set at 350 mm downstream from the channel inlet, where d_H is the hydraulic equivalent diameter of the channel.

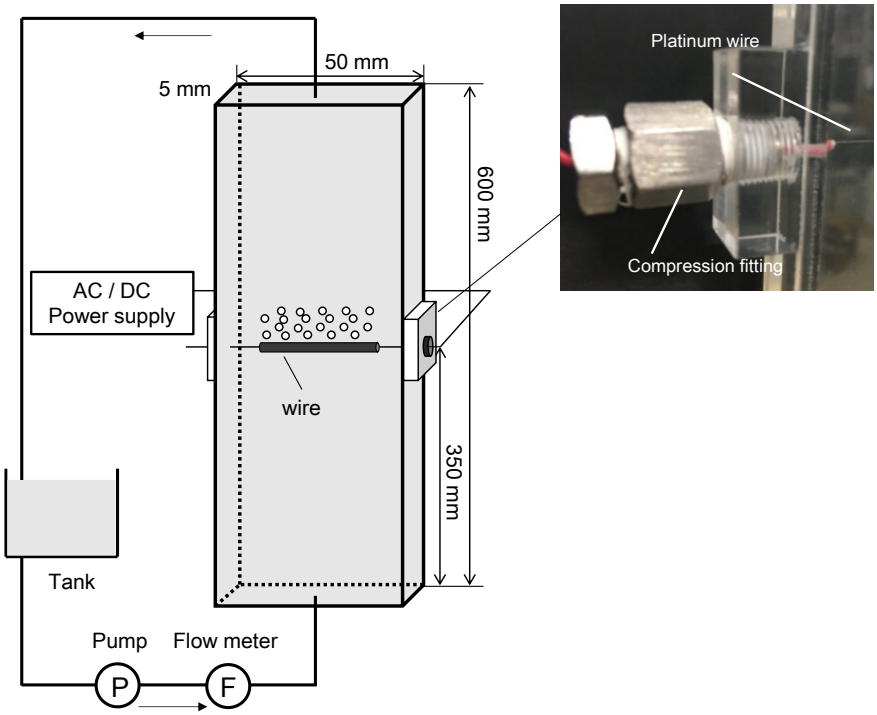

Fig. A.1 Experimental apparatus.

The flow did not significantly affect the formation of microbubbles and their subsequent contraction and growth, and $\bar{u}$ was considered to be the same as the advection velocity of bubbles. Experiments were conducted under three conditions ($\bar{u}$ = 0.01, 0.02 and 0.03 m/s). Microbubbles were generated at AC (f = 60 Hz), $\bar{q}$ = 4.5 MW/m^2, and the bubble generation state, d_B, and n_B were measured.

A.1.2 Evaluation method

The test section of the experimental apparatus is shown in Fig. A.2. The conservation of n_B in a small area in a fluid with bubbles is expressed as

$$\frac{\partial n_B}{\partial t} + \nabla \cdot (\boldsymbol{u}_B n_B) = G_B \tag{A.3}$$

where $\boldsymbol{u}_B$ is the velocity of the bubbles and G_B the amount of bubbles generated per unit time

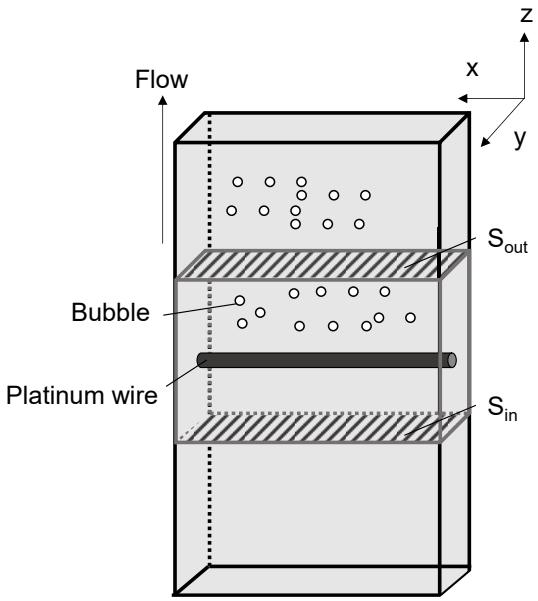

Fig. A.2 Test section of calculation.

and unit volume in the small area. Integrating Eq. (A.3) for the region bounded by the two cross sections of the test section in the direction of the flow axis (Fig. A.2) yields

$$\int_V \frac{\partial n_B}{\partial t} dV + \int_V \nabla \cdot (\boldsymbol{u}_B n_B) dV = \int_V G_B dV \tag{A.4}$$

Using the Gauss divergence theorem, Eq. (A.4) can be expressed as

$$\int_V \frac{\partial n_B}{\partial t} dV + \int_S \boldsymbol{u}_B n_B \cdot d\boldsymbol{S} = \int_V G_B dV \tag{A.5}$$

When the flow is in a steady state, Eq. (A.5) reduces to

$$\int_S \boldsymbol{u}_B n_B \cdot d\boldsymbol{S} = \int_V G_B dV \tag{A.6}$$

Since the inflow surface in this region has only two cross sections perpendicular to the z

direction, Eq. (A.6) can be expressed as

$$\int_{S_{out}} u_z n_B dS - \int_{S_{in}} u_z n_B dS = \int_V G_B dV \tag{A.7}$$

where S_{in} and S_{out} are the inflow and outflow surfaces, respectively. u_z is the z-directional velocity component of the bubble velocity. Since bubbles are generated only on the platinum wire, and the disappearance of bubbles is assumed to be negligible, Eq. (A.7) becomes

$$\int_{S_{out}} u_z n_B dS - \int_{S_{in}} u_z n_B dS = g_B l \tag{A.8}$$

where g_B is the amount of bubbles generated per unit length of platinum wire and l the length of the platinum wire. Since there are no bubbles in S_{in}, g_B is obtained as

$$g_B = \frac{1}{l} \int_{S_{out}} u_z n_B dS \tag{A.9}$$

In this experiment, at a certain height downstream from the platinum wire, the high-speed camera was moved in the x and y directions using a traverse system to capture the bubble generation state, and u_z and n_B in each region were obtained. The imaging system is shown in Fig. A.3. When taking images with a spatial resolution that could capture microbubbles, the volume of the image becomes small, and it is time-consuming to evaluate the total amount of bubbles generated from the platinum wire. Therefore, the distribution of bubbles was considered to be symmetric with respect to the platinum wire, and the amount of bubbles generated was obtained for the measurement area shown in Fig. 4.2. This region covers the area from the platinum wire to the wall in the y direction and the area from the center of the platinum wire in the longitudinal direction to the x direction, where no bubbles were observed. The bubble production rate G_B' obtained in this region is expressed by

$$G_B' \cong \frac{1}{4} g_B l \tag{A.10}$$

G_B' is assumed to be about 1/4 of the total amount of bubbles produced by the platinum wire. The length of the platinum wire was set to 10 ± 0.5 mm when evaluating the amount of bubbles generated. The spatial volume of the imaging space is 2.00 × 0.31 × 1.50 mm^3 based on the imaging area and DOF (see Sec. 2.2.3).

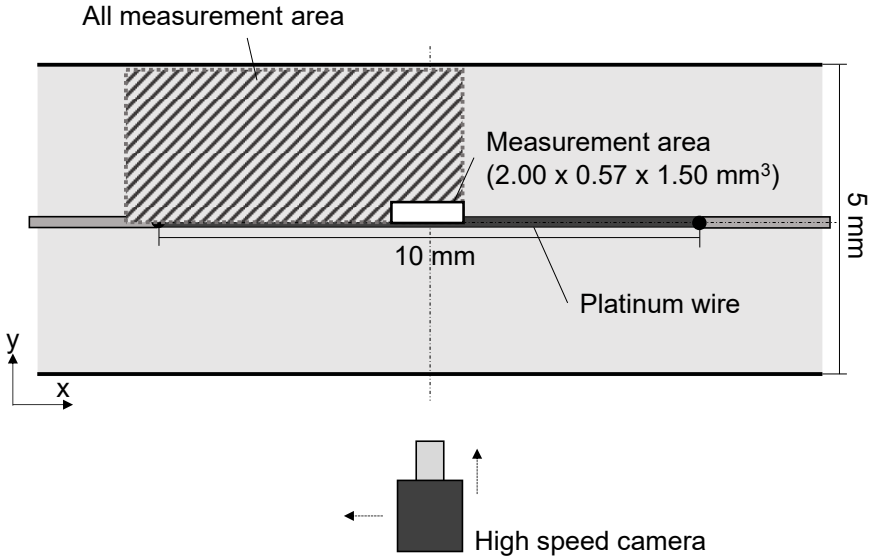

Fig. A.3 Measurement area.

A.2 Bubble characteristics and heat transfer surface temperature

The relationship between $\bar{u}$, $\bar{d}_B$ and $\bar{n}_B$ is shown in Table A.1. $\bar{d}_B$ is almost equal for $\bar{u}$ = 0.00 and 0.01 m/s, while $\bar{d}_B$ decreases with increasing $\bar{u}$ for $\bar{u} \geq 0.01$ m/s. The $\bar{n}_B$ decreases as $\bar{u}$ increases.

Table A.1 Relation between $\bar{u}$, d_B and n_B.

$\bar{u}$ [m/s]	$\bar{d}_B$ [μm]	$\bar{n}_B$ [$\times 10^{10}$ m^{-3}]
0.00	16.2	10.1
0.01	16.4	4.5
0.02	15.1	2.3
0.03	14.2	1.5

Fig. A.4 shows the time variation of the surface temperature T_W for each $\bar{u}$ during one heating cycle (1/120 s). The average heat transfer surface temperature T_{Wave} is shown in Table A.2. From Fig. A.4 and Table A.2, it can be seen that T_{Wave} for $\bar{u}$ = 0.03 m/s is lower than that for the other conditions. This is due to the cooling effect on the heat transfer surface as the subcooled water is more easily supplied near the heat transfer surface as $\bar{u}$ increases, which is similar to the formation at low heat flux. The decrease in $\bar{d}_B$ may be due to the decrease in $\bar{n}_B$, which reduces the probability of bubbles coalescing with each other and the fact that vapor bubbles attached to the platinum wire were cooled more easily by the subcooled water than in the pool water, making it difficult for relatively large diameter vapor bubbles to be formed.

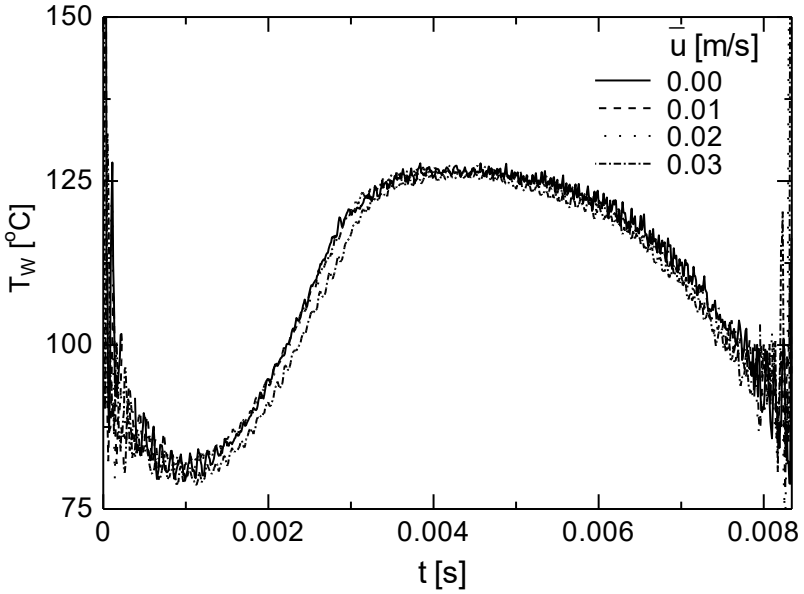

Fig. A.4 Relation between t and T_W.

Table A.2 Relation between $\bar{u}$ and T_{Wave}.

$\bar{u}$ [m/s]	0.00	0.01	0.02	0.03
T_{Wave} [m/s]	109.9	110.0	110.1	108.1

A.3 Evaluation of bubble generation

A.3.1 Flow state

Fig. A.5 shows a schematic diagram of the measurement area where the bubbles were observed, and Figs. A. and A.7 show the flow states at $\bar{u}$ = 0.02 m/s. Microbubbles were observed at (i, j) = (1, 1) for DC and (i, j) = (1, 1 ~ 4) for AC. The AC condition generated more bubbles than the DC condition.

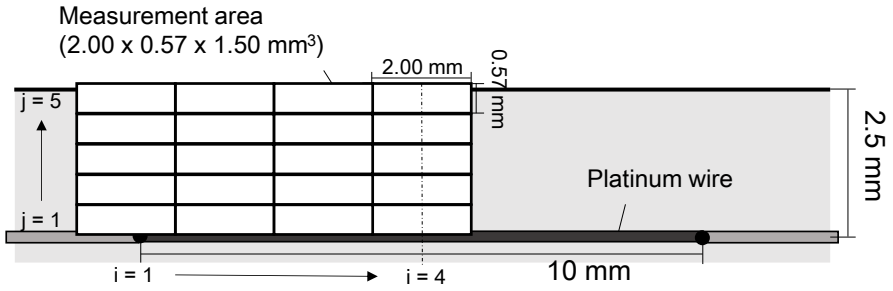

Fig. A.5 Schematic diagram of the measurement area.

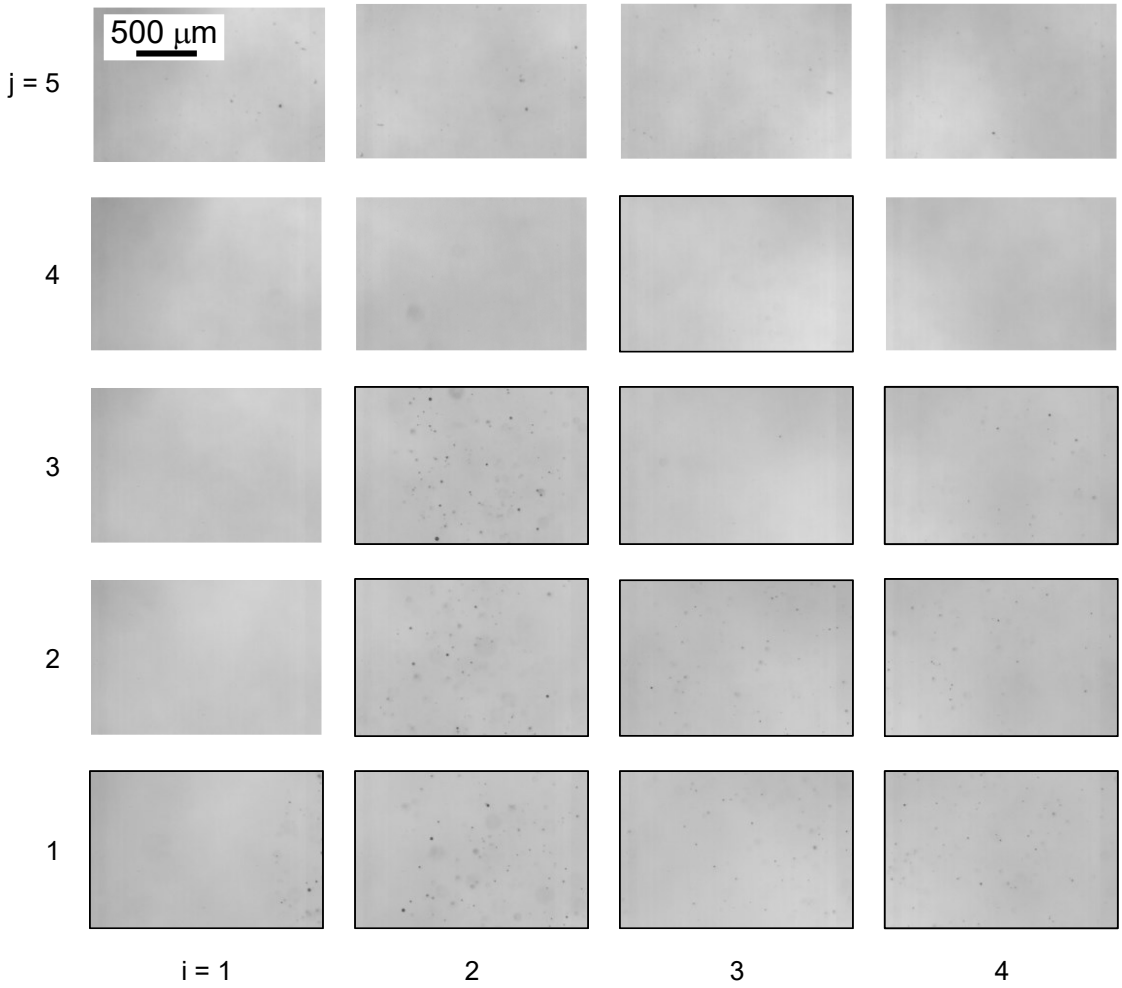

Fig. A.6 Images of generated microbubbles (DC, $\bar{q}$ = 4.5 MW/m^2).

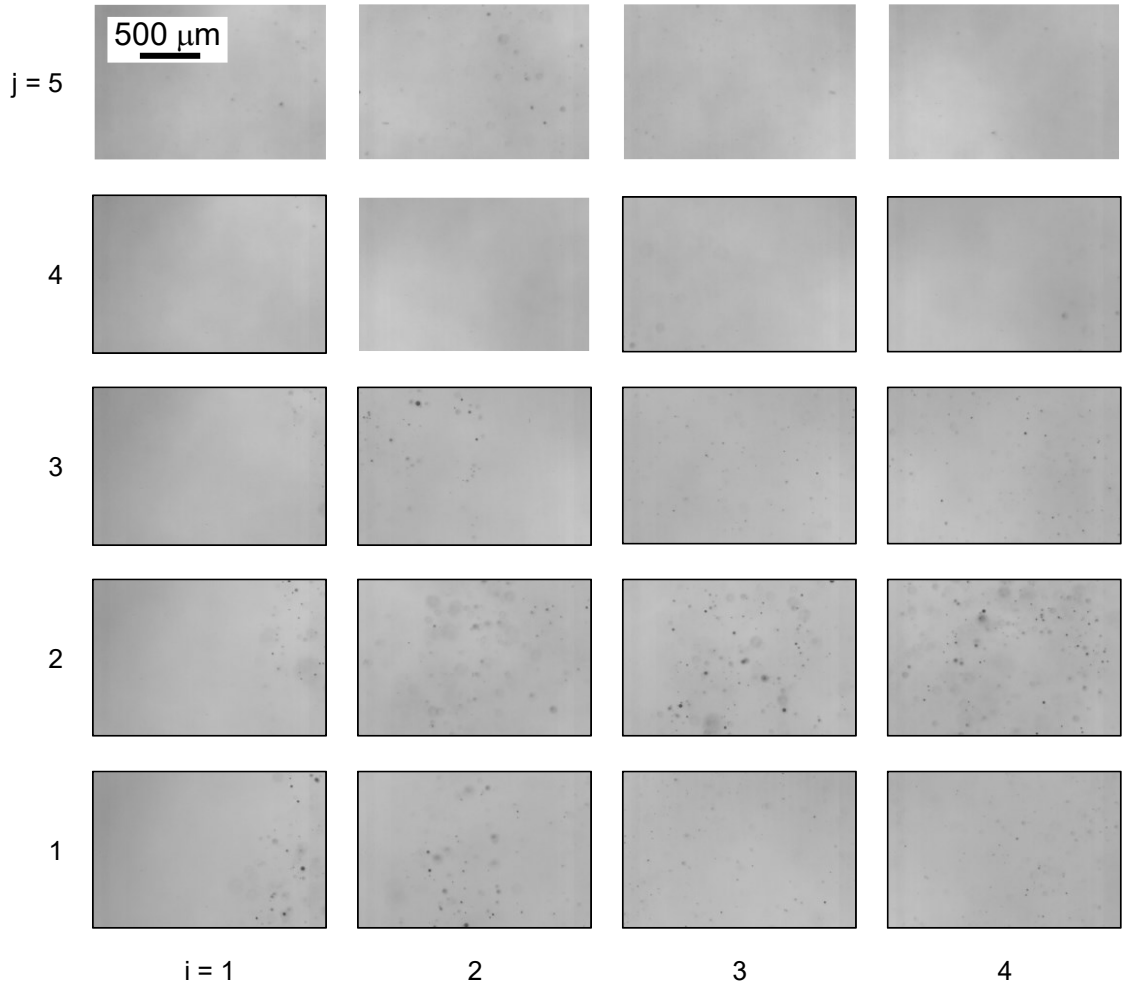

Fig. A.7 Images of generated microbubbles (AC (f = 60 Hz), $\bar{q}$ = 4.5 MW/m^2).

A.3.2 n_B

The $\bar{n}_B$ in each region was calculated for the images shown in the previous section. The distribution of $\bar{n}_B$ for DC and AC is shown in Fig. A.8 which shows that there are no bubbles near the wall surface and that $\bar{n}_B$ is higher for AC. The $\bar{n}_B$ with AC exhibits peaks at a distance from the platinum wire. The fact that $\bar{n}_B$ was higher for AC suggests that the flow was disturbed by the bubbles during the generation of microbubbles, resulting in a bias in the distribution.

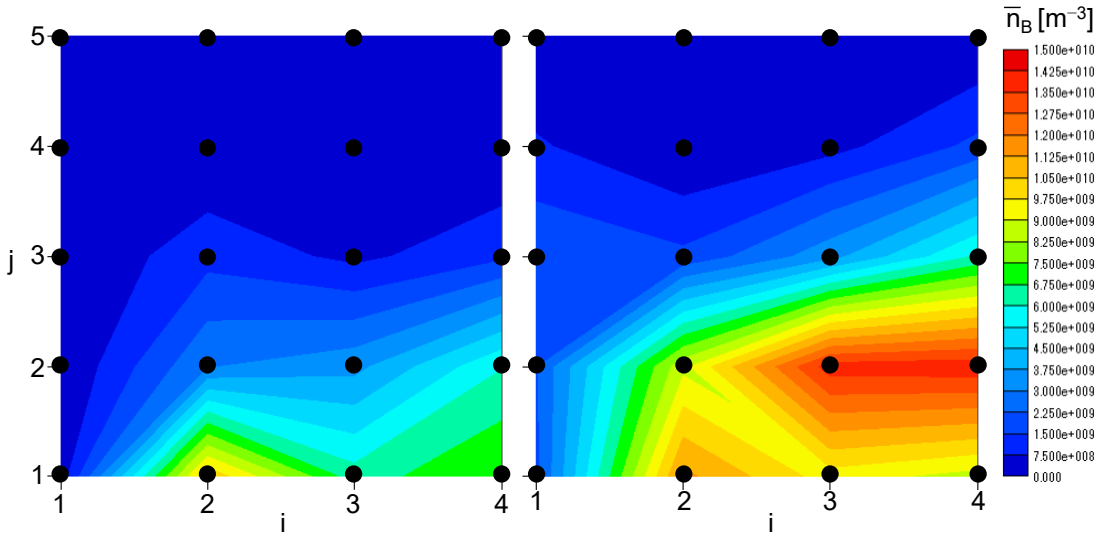

(a) DC. (b) AC.

Fig. A.8 Distribution of $\overline{n}_B$.

A.3.3 Rise velocity

The average velocity of bubbles in each region was calculated for the images shown in Section A.3.1 by counting the number of pixels of the traveling distance in the z-direction during 0.02 s. The number of bubbles sampled was 25. The distributions of $\overline{u}_{Bz}$ for DC and AC are shown in Fig. A.9. In the case of DC, $\overline{u}_{Bz}$ takes the largest values near the platinum wire and decreases as it moves toward the wall. On the other hand, in the case of AC, the distribution of $\overline{u}_{Bz}$ is more skewed than that of DC. As shown in the previous section, the distribution of bubbles is biased in the AC case, suggesting that $\overline{u}_{Bz}$ is also affected by the agitation.

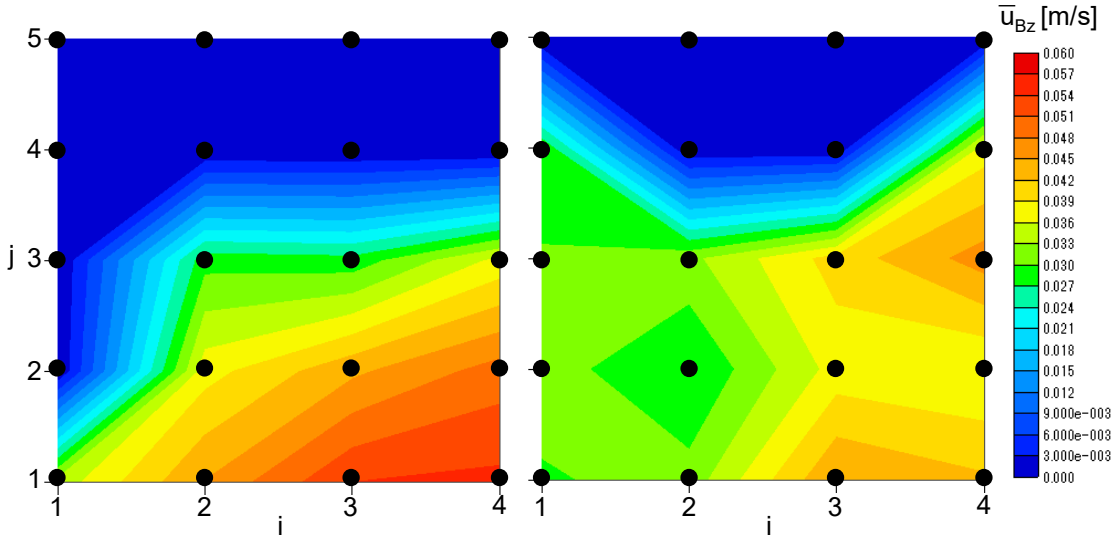

(a) DC. (b) AC.

Fig. A.9 $\bar{u}_{Bz}$ distribution.

A.3.4 Amount of generated bubbles

$G_B' = 2164$ in DC case and $G_B' = 3610$ in the AC case were calculated. The amount of microbubbles produced by AC is about 1.7 times greater than that by DC, which is about the same ratio as that in still water (Fig. 4.19).

From Eq. (A.10), $g_B = 1.45 \times 10^6$ $s^{-1}m^{-1}$, which corresponds to a platinum wire length of 0.87 mm and a bubble production rate of about 10 bubbles per cycle of q variation (1/120 s), clearly less than the image shown in Sec. 4.3.2. This may be due to the decrease in bubble diameter caused by contraction of bubbles due to mass transfer through the gas-liquid interface after bubble formation, and an increase in the number of microbubbles with diameters that cannot be captured in the image (diameters of about 5 μm or less).

References for Appendix A

[1] L. Chen, S.J. Xu, M.J. Ni, The Kármán vortex street inversion and heat transfer around a square cylinder at low Reynolds and magnetic interaction numbers, *Int. J. Heat Mass Transf.*, vol. 117, 768–779, 2018.

Appendix B

Attachment state of microbubbles to dirt surface in laminar flow

In Chapter 2, microbubbles did not attach to the oil under the laminar flow conditions in the horizontal channel due to buoyancy. It would be worth to investigate whether microbubbles attach to the oil in a vertical flow channel even under laminar flow conditions.

Fig. B.1 shows the experimental apparatus which mainly consists of a microbubble generator tank (Science, SMBO-PS480), a test section, a pump (IWAKI, MD-6ZK), a flow meter (Nippon Flow Cell, NSP-5-B006), and a high-speed camera (Photron, SA-X2) was used to capture the microbubbles attached to oil. Pure water (T_0 = 298 ± 0.5 K, DO_0 = (8.5 ± 0.3) × 10^{-3} kg/m^3) purified by a water purification system (Merck, Elix UV5) was used for the liquid phase. Water in the tank was suctioned by a pump and passed through the test section. The dimensions of test section were 300 × 300 × 500 mm in width, depth and height, respectively. The cross-sectional area of test section were 5 and 10 mm in height and width, respectively. The area of the oil part was 5 mm × 5 mm and the depth was 1 mm.

The experiments were carried out at Re = 1000 ± 2, 2000 ± 2 and 3000 ± 3, where Re was defined as in Eq. (2.1). Fig. B.2 shows the state of microbubbles attaching to the oil. Fig. B.2 (a) is a state at t = 0 s and Fig. B.2 (b) was a state at t = 240 s. As in the results of Chapter 2, microbubbles attaching to the oil and grew to milli-bubble sizes and where swept away by water. The attachment rate increases with increasing Re. The number of bubbles are decreasing with increasing Re due to the fact that the growing microbubbles have already been swept away by the water flow. Fig. B.2 clearly showed that microbubble attachment can

also occur in laminar flows when microbubbles are generated near dirt.

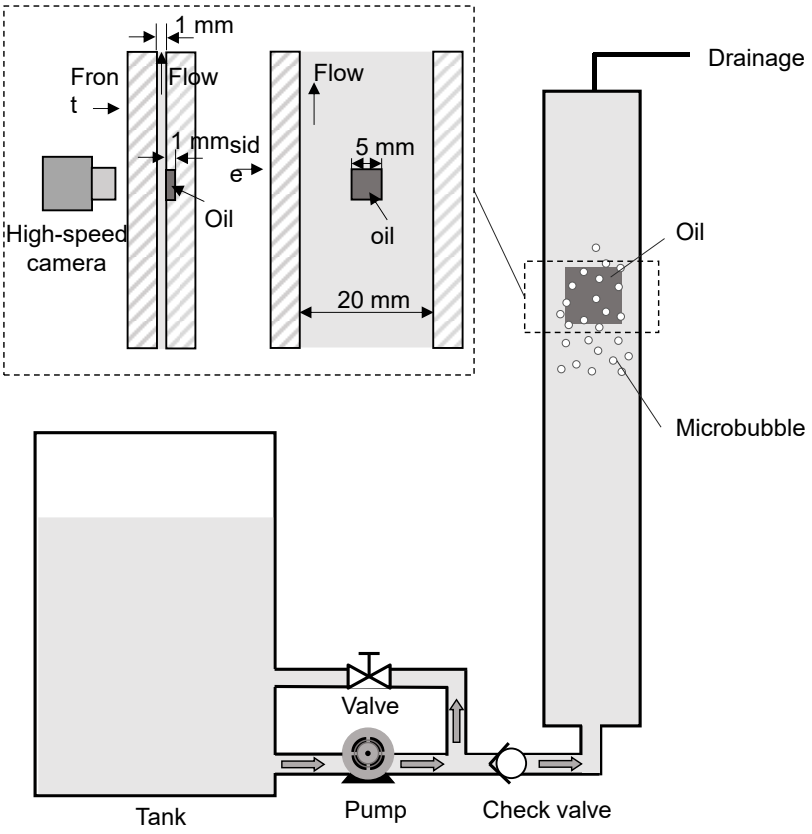

Fig. B.1 Experimental apparatus.

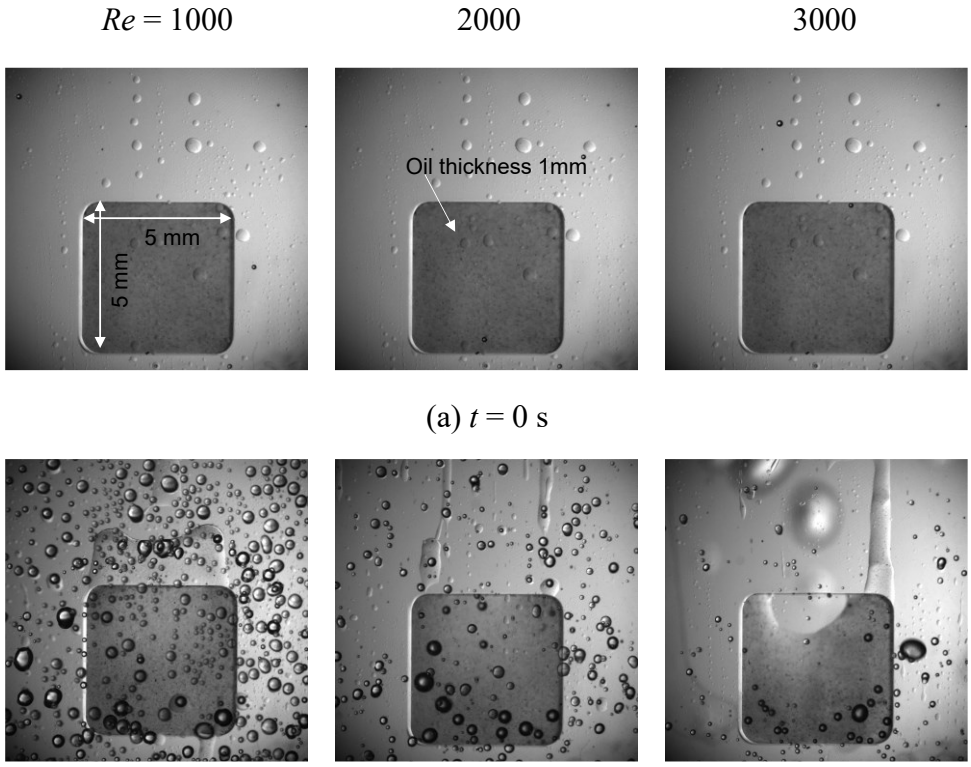

(a) $t = 0$ s

(b) $t = 240$ s

Fig. B.2 State of microbubbles attached on oil.

Academic and lecture papers related to this research

[1] Y. Li, K. Hayashi, F. Okamoto, S. Hosokawa, A. Tomiyama, Effects of microbubbles on removal of viscous oil adhering to channel wall, *Chem. Eng. Res. Des*., vol. 193, 75–84, 2023.

[2] Y. Li, S. Hosokawa, K. Hayashi, A. Tomiyama, N. Shibata, Y. Maeda, Generation of microbubbles by subcooled boiling of water with dissolved incondensable gases, *Multiph. Sci. Technol*., vol. 33, 17–31, 2021.

[3] Y. Li, S. Hosokawa, K. Hayashi, A. Tomiyama, Y. Maeda, Numerical Prediction of Size Distribution of Microbubbles in Water with Mass Transfer, *Multiph. Sci. Technol*., vol. 36, 41–54, 2024.

[4] Y. Li, S. Hosokawa, A. Tomiyama, Y. Maeda, Generation of Micro-Bubbles from a Heated Thin Wire, *Proc of the 11th International Symposium on Measurement Techniques for Multiphase Flow* (ISMTMF 2019), 2019.

[5] 李　月桂，細川　茂雄，冨山　明男，前田　康成，蛍光を用いたマイクロバブルによる洗浄効果の評価，混相流シンポジウム 2020, 2020.

Acknowledgments

First of all, I would like to express my appreciation to the Ministry of Education, Culture, Sports, Science and Technology (MEXT) of Government of Japan for their financial support during my stay in Japan.

I would also like to express my deep gratitude to my supervisors Prof. Kosuke Hayashi, Prof. Shigeo Hosokawa and Prof. Akio Tomiyama whose continuous support, patient guidance and valuable suggestions have enabled me to complete my studies. Their feedback has been instrumental in my growth as a researcher. I am also grateful to dissertation examiners Prof. Hitoshi Asano and Prof. Yohsuke Imai for providing constructive feedback on my dissertation. I would also thank Asst. Prof. Ryo Kurimoto, Mr. Naoyuki Yoshida, Dr. Nobuya Kobayashi and Shiqi Yang for constantly providing constructive feedback for my studies during this period.

I would also like to offer my special thanks to members of the laboratory of Multiphase Fluid Dynamics, Kobe University– in particular Mr. Masataka Yoshida, Mr. Chiaki Taya, Mr. Kazuya Ishii, Naoya Iwamoto and Fuyuki Okamoto for all their cooperation. I am also grateful to my classmate of Master course Yuki Matsuo, Hitoshi Mori, Yoshihiro Yahara and Takashi Yoshioka for their help.

Finally, I would like to take this opportunity to thank my family and friends especially Yuzheng Wu, Lanjie Chen, Chenyang Wang, Mr. Kazuhiro Sainohira, Mr. Yunqi Lin and Dr. Ayşegül Öktem who studied in Kobe University for all their patience and love, both who are in China and Japan. Their support and encouragement have helped me to sail through the difficult times and been instrumental in lifting my spirits up whenever I felt demotivated.

Li Yuegui

January, 2024

In the colophon, indicate all the necessary information as follows;

Doctoral Dissertation, Kobe University
“Cleaning Effect of Microbubbles and Development of Microbubble Generator”, 136 pages
Submitted on January, 8, 2024

When published on the Kobe University institutional repository /*Kernel*/, the publication date shall appear on the cover of the repository version.